Autothermal Oxidative Pyrolysis of Biomass Feedstocks over Noble Metal Catalysts to Liquid Products

A dissertation submitted to the faculty of the
Graduate School of the University of Minnesota
by

Christine Marie Balonek

In partial fulfillment of the requirements for the
degree of Doctor of Philosophy.

Advisor: Lanny D. Schmidt

July, 2011

ACKNOWLEDGMENTS

Thank you to my advisor, Professor Lanny Schmidt, for his guidance and advice during my graduate career. Thank you to the entire Schmidt Group for help and discussions, both academic and non-academic. To my family and friends who have always been a source of support and inspiration, thank you.

ABSTRACT

Two thermal processing technologies have emerged for processing biomass into renewable liquid products: pyrolysis and gasification/Fischer-Tropsch processing. The work presented here will demonstrate oxidative pyrolysis of biomass as an alternative process to avoid the intrinsic disadvantages of traditional pyrolysis. Additionally, work has been conducted to examine the processing of biomass derived synthesis gas to condensable products, which involves mitigating new challenges when compared with the processing of conventional coal-based feedstocks during gasification/Fischer-Tropsch.

The research group of Professor Lanny D. Schmidt has pioneered autothermal partial oxidation of a variety of gas and liquid feedstocks on noble metal catalysts to synthesis gas with high selectivity, char-free operation, and on millisecond timescales at temperatures of 600 - 1000 °C. More recently, cellulose has been shown to decompose on the catalyst surface to also produce high selectivities to synthesis gas. Chapter 2 discusses the discovery of an intermediate liquid phase during the autothermal processing of cellulose particles over rhodium-based catalysts. Volatilization of 300 μm cellulose particles on a 700 °C catalytic surface were filmed using a high speed camera capable of 1000 frames per second. The cellulose particles decomposed through an intermediate liquid, which boiled to gaseous species that convected into the catalyst bed. The high heat transfer rates made possible by the intimate contact of the boiling liquid and the hot surface allowed rapid reactions without leaving char residues. This unique insight allows new processes to be designed that exploit this type of cellulose thermal decomposition.

Experiments were conducted to investigate the extension of catalytic partial oxidation over noble metal catalysts to convert biomass to liquid pyrolysis products, termed 'oxidative pyrolysis'. Model compounds were chosen to represent the lignin fraction of lignocellulosic biomass to more easily and accurately study the proposed system. Chapter 3 discusses the autothermal oxidative pyrolysis of monoaromatics over noble metal catalysts. Benzene, toluene, ethylbenzene, cumene, and styrene were indepen-

dently studied over five noble metal-based catalysts (Pt, Rh, Rh/γ-Al_2O_3, Rh-Ce, and Rh-Ce/γ-Al_2O_3) while varying the carbon-to-oxygen feed ratio. Aromatic rings were observed to be very stable in the reactor system, while homogeneous reactions of the alkyl groups of ethylbenzene and cumene were prevalent.

Chapter 4 addresses the oxidative pyrolysis of microcrystalline cellulose particles as a model for lignocellulosic biomass to yield liquid products. Cellulose was demonstrated to autothermally convert to combustion, partial oxidation, and pyrolysis products without char formation. The effects of support geometry, catalyst metal, and hydrogen addition on product selectivities were studied. Platinum-coated alumina spheres maximized the yield of pyrolysis products by favoring combustion chemistry and minimizing reforming activities, as compared with rhodium-based catalysts. Up to 60 % carbon selectivity to pyrolysis products could be achieved on a Pt catalyst with hydrogen addition.

As mentioned, previous research in the Schmidt group has shown high selectivities to synthesis gas by autothermal reforming of cellulose particles. However, utilizing this biomass-derived syngas, as opposed to traditional coal-based syngas, is not well studied. Biomass-derived synthesis gas presents a new set of inorganic impurities that may affect catalyst performance during Fischer-Tropsch processing. Small quantities (ppm) of typical biomass inorganics (Na, K, Li, and Ca) were loaded onto γ-Al_2O_3-supported Co-Re powder catalysts to study the effect on product selectivities (Chapter 5). The inorganic impurities were found to affect the reduction of Co and increase CO_2 and C_{5+} selectivities, which were largely attributed to electronic effects.

Chapter 6 proposes future research utilizing gas chromatography and mass spectrometry to identify and quantify specific components within liquid pyrolysis products, generally termed 'pyrolysis oil'. This work will build on the research presented in Chapter 4: the demonstration of oxidative pyrolysis of cellulose to produce up to 50 % carbon selectivity to pyrolysis products. Further characterization of the pyrolysis oil will involve pH and water fraction measurements. Preliminary work shows the presence of several acids, alcohols, phenols, pyrans, among other small oxygenated species in the pyrolysis oil. Levoglucosan was identified as being the largest carbon-based fraction of the oil, up to 11 wt% under certain conditions. Additional experiments extending oxidative pyrolysis to process polymer feedstocks are also proposed.

CONTENTS

LIST OF TABLES

LIST OF FIGURES

CHAPTER

ONE

INTRODUCTION

In the last several years, environmental concerns and the rise of fossil fuel prices have prompted discussion and research in alternative and renewable energy sources. Currently, the global economy and infrastructure relies heavily on liquid hydrocarbon transportation fuels. To ease a transition to a more renewable-based fuel economy, a suitable liquid fuel that can utilize existing infrastructure would be ideal.

Biomass has emerged as one of the forerunners of renewable energy sources and is the only source of renewable carbon. According to a study by the US Department of Agriculture and Department of Energy, 30 % of transportation fuels can be replaced with biomass-based fuels by 2030. This can be accomplished by processing over 1 billion tons of dry biomass from many underutilized sources, such as forestry wastes and crop residues (Fig. 1.1).[1] This study assumes that by 2030 large-scale biorefineries will exist to process all varieties of biomass, including lignocellulosic. The US EPA has mandated that by 2020 annual production of renewable fuel should be 30 billion gallons (ethanol equivalent).[2–4] More specifically, nearly a third of the renewable fuel should be made from cellulosic biomass sources. In 2010, the EPA required that 100 million gallons of renewable fuel be made from cellulosic material, however production fell far short of this goal, at only 6.5 million gallons. Lignocellulosic biomass is an important and major source of renewable fuel, but is more difficult to process than corn starch and other non-lignin biomass feedstocks. More efficient and versatile technologies are necessary to reach renewable fuel production goals.

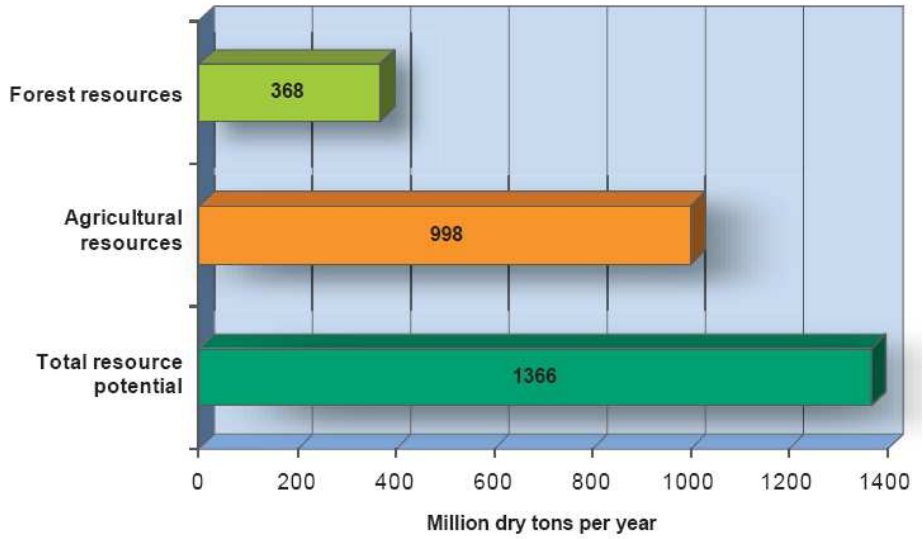

Figure 1.1: Annual biomass resource potential from forest and agricultural resources.[1]

1.1 Lignocellulosic Biomass Structure

The term 'lignocellulosic' indicates types of biomass made of cellulose, hemicellulose, and lignin fractions.[5–7] This includes woody biomass (hardwood and softwood trees), grasses, and agricultural residues (i.e. corn stover). The typical composition of lignocellulosic biomass is 35 - 50 % cellulose, 20 - 35 % hemicellulose, and 10 - 25 % lignin on a dry basis. Ash and extractives make up the remaining fraction and are generally low for woody biomass, $\sim$ 1 and $\sim$ 2 %, respectively.[8] However, these fractions can vary based on the type of lignocellulosic biomass; for example, rice husks can have $\sim$ 17 % ash and corn stover can have $\sim$ 5 % extractives.

1.1.1 Cellulose

Cellulose is a linear homopolymer of D-glucose monomer units (Fig. 1.2(a)). The monomers are 1,4-β-D-glucosidic bonded to form long chains (n $>$ 3000).[8] These chains are hydrogen bonded (Fig. 1.2(b)) to form crystalline microfibrils, shown in Figure 1.3. The crystallinity of cellulose makes it difficult to process using biological methods. The lignocellulosic biomass must first be pretreated (a current area of research) to remove hemicellulose and lignin and increase the availability of the celluose for cellulase enzymes.[6,7] During enzymatic hydrolysis, cellulase converts cellulose to glucose, which can then be fermented to ethanol.

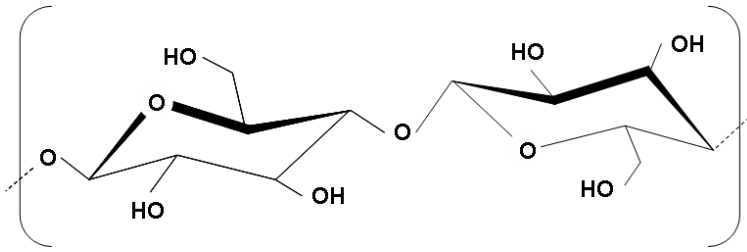

(a) D-glucose

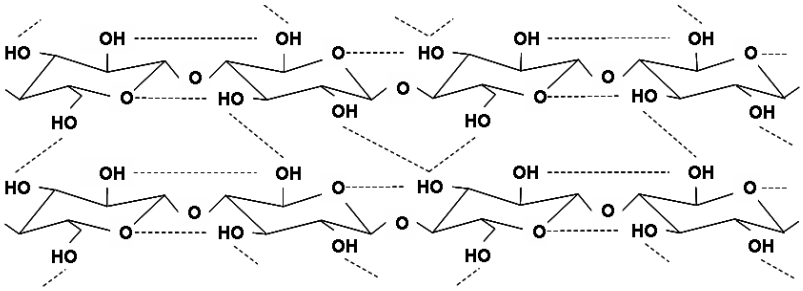

(b) Crystalline Cellulose

Figure 1.2: Structure of cellulose. (a) Two D-glucose units. (b) Structure of crystalline cellulose with hydrogen bonding indicated.

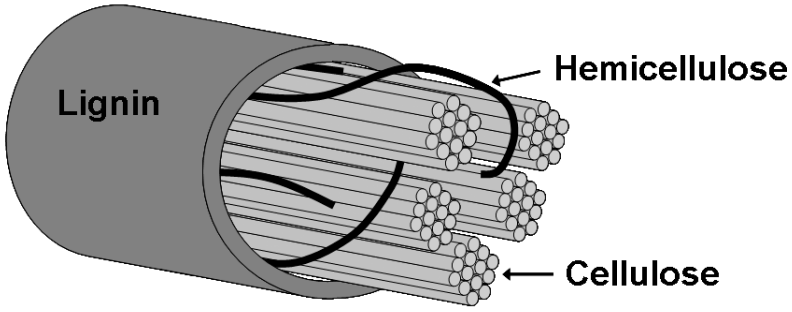

Figure 1.3: Representation of lignocellulosic biomass structure. Cellulose microfibrils enclosed in hemicellulose and lignin.

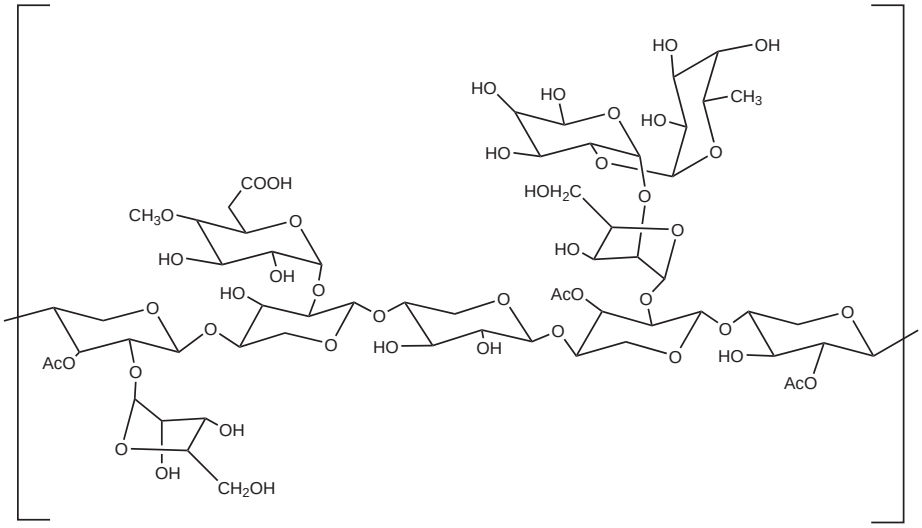

Figure 1.4: Example of hemicellulose structure by Kersten et al.[8]

1.1.2 Hemicellulose

Hemicellulose is a branched heteropolymer of several different pentose and hexose sugars. An example of hemicellulose structure is represented in Figure 1.4, though the exact structure can vary based on the type of biomass. The C_5 sugars in hemicellulose are generally xylose and arabinose. The C_6 sugars are galactose and mannose.[5,7] The hemicellulose polymers form a matrix, or sheaths, that contain the cellulose microfibrils (Fig. 1.3). During biological processing, hemicellulose can be hydrolyzed into C_5 and C_6 sugars for fermentation.[6] Hemicellulose processing is an active area of study since there is currently no single organism that can efficiently convert both C_5 and C_6 sugars to alcohol.[5]

1.1.3 Lignin

Lignin is a complex heteropolymer that provides mechanical stability and aids in water movement throught lignocellulosic biomass.[8,9] The structure of lignin is highly variable, even within a single plant, and is composed of aromatics with many functional groups, including alcohols, aliphatics, phenols, methoxyls, and ethers (Fig. 1.5). Lignin impedes the biological conversion of lignocellulosic biomass to ethanol. Pretreatments are necessary to remove lignin before hydrolyzing the cellulose and hemicellulose. Current research is investigating the genetic modification of plants to reduce lignin content to improve ethanol yeilds.[10,11]

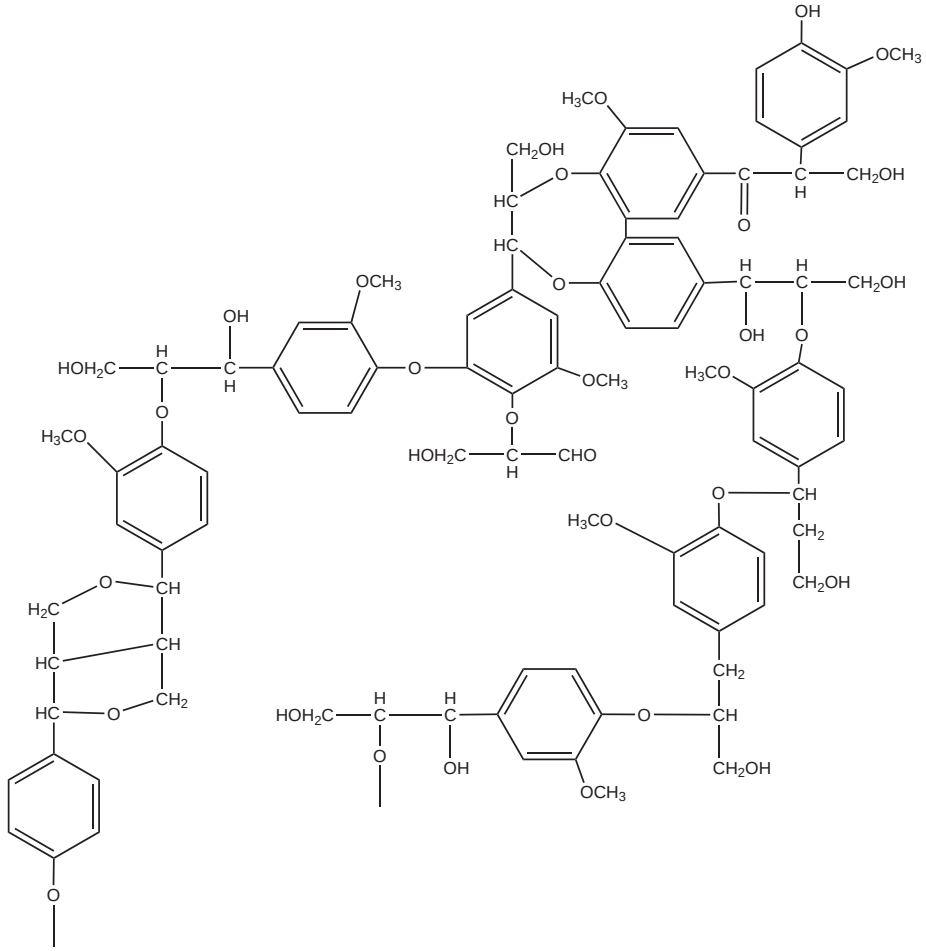

Figure 1.5: Example of lignin structure by Kersten et al.[8]

1.2 Thermochemical Processing Techniques

Biomass processing research has largely focused on biological and thermochemical routes to produce renewable liquid fuels and chemicals. One biological processing route is the production of ethanol, which can be readily mixed with gasoline as a transportation fuel additive to displace fossil fuel use. The US Environmental Protection Agency currently approves 10 % ethanol in gasoline mixtures (E10) for all transportation uses, and 15 % for light-duty vehicles manufactured after 2001 and flex-fuel vehicles.[12] E10 is widely available and nine states have laws specifically mandating the blending of ethanol into gasoline.[13]

Corn starch is the primary feedstock for ethanol prodcution. Processing of the starch involves hydrolysis to produce glucose, fermentation to ethanol, and recovery of the ethanol from the product stream. However, this process does not directly translate for the processing of lignocellulosic biomass, which can require pretreatments and additional processing (Section 1.1).

In addition to the difficulties associated with processing of lignocellulosic biomass, biological processing to ethanol has several intrinsic disadvantages. The process speed is limited by the enzymes and yeast, which are slow when compared to thermochemical process methods. Distillation of the water and ethanol product stream is energy intensive and requires additional steps to create a pure ethanol product. Additionally, ethanol has a lower heating value than gasoline, is hydroscopic, and corrosive.[14] Thermochemical processing of lignocellulosic biomass feedstocks may be a faster and more efficient route to produce renewable fuels and chemicals. Two main thermochemical routes discussed in the following sections are pyrolysis and gasification with Fischer-Tropsch processing.

1.2.1 Pyrolysis

Pyrolysis is an endothermic thermochemical processing method that can utilize biomass to make fuels and chemicals. During pyrolysis, feedstock is thermally decomposed at atmospheric pressure and in the absence of oxygen to select primarily for liquid products. Solid, liquid, and gaseous products can be produced depending on reaction conditions: lower temperatures and long residence times have high selectivity to solid carbon products, while high temperatures and short residence times select for gaseous products.[15] Fast pyrolysis has emerged as a particular area of interest to maximize the yield of liquid hydrocarbons from biomass feedstock. The process is characterized by high heat transfer rates, temperatures of 400 - 500 °C, short resi-

Acids	wt. %	Syringols	wt. %
Formic	0.3 to 9.1	2,6 DiOMe phenol (syringol)	0.7 to 4.8
acetic	0.5 to 12	propyl syringol	0.1 to 1.5
propanoic	0.1 to 1.8	syringaldehyde	0.1to 1.5
Esters		Sugars	
angelicalactone	0.1 to 1.2	Levoglucosan	0.4 to 1.4
2(5H)-Furanone, 5-methyl		Glucose	0.4 to 1.3
Alcohols		Fructose	0.7 to 2.9
methanol	0.4 to 2.4	D-xylose	0.1 to 3.2
ethanol	0.6 to 1.4	cellubiosan	0.6 to 3.2
ethylene glycol	0.7 to 2	1,6 anhydroglucofuranose	3.1
Ketones		Furans	
acetone	2.8	furanone	0.1 to 1.1
Aldehydes		Furfural	0.1 to 1.1
formaldehyde	0.1 to 3.3	Furfural alcohol	0.1 to 5.2
acetaldehyde	0.1 to 8.5	5-OH-methyl-2-furfural	0.3 to 2.2
ethanedial	0.9 to 4.6	Misc Oxygenates	
Phenols		Hydroxyacetaldehyde	0.9 to 13
phenol	0.1 to 3.8	acetol (hydroxyacetone)	0.7 to 7.4
2-ethyl phenone	0.1 to 1.3	methyl cyclopentenolone	0.1 to 1.9
1,4 diOH benzene	0.1 to 1.9	4-OH-3-methoxybenzaldehyde	0.1 to 1.1
Guaiacols			
2-methoxy phenol (guaiacol)	0.1 to 1.1		
4-methyl guaiacol	0.1 to 1.9		
Isoeugenol	0.1 to 7.2		
Eugenol	0.1 to 2.3		

A. Bridgwater, S. Czernik, J. Diebold, D. Meier, A. Oasmaaa, C. Peacocke, J. Piskorz, D. Radlein. *Fast Pyrolysis of Biomass: A Handbook*. CPL Press, Speen, UK, **2008**

Figure 1.6: Typical wt% of several pyrolysis oil components.

dence times (< 2 s), and rapid cooling to condense products. The resulting liquid product, referred to as pyrolysis oil or bio-oil, is highly variable depending on the type of feedstock and can be made up of hundreds of decomposition products of lignin, hemicellulose, and cellulose (Fig. 1.6). Pyrolysis oil is typically characterized by a high water content (< 35 %), numerous oxygenated species, and a low pH (~ 2). This oil can be upgraded (i.e. deoxygenated and stabilized) to a more desireable product for use as a transportation fuel.

Several reactor configurations can be used for fast pyrolysis: fluidized bed, rotating cone, and vacuum, among others.[16] Bubbling fluidized bed reactors are the most common design and use sand to provide a large thermal mass and even heat distribution. The reactor is heated externally, which can result in heat transfer limitations upon scale-up, inhibiting reactor performance.[17] Since the rate-limiting step in the process is heat transfer to the biomass particles, small particles (~ 2 - 3 mm) are necessary. Pyrolysis products (solid char particles, gases, and vaporized liquids) quickly exit the reactor, char is separated, and the gases are immediately cooled to condense the liquid product and minimize further thermal reactions (Fig. 1.7(a)). Circulating fluidized beds operate similarly, however the sand and char are circu-

lated, separated, and the clean sand is recycled to the reactor (Fig. 1.7(b)), which may be more appropriate for larger reactor throughputs.

Fluidized bed technology is widely understood and used by many start-up companies. Dynamotive Energy Systems Corporation currently operates a 200 ton per day biomass fast pyrolysis unit in Guelph, Ontario (completed in 2007).[18] The Dynamotive system (Fig. 1.8) reacts dry biomass (< 10 wt% water) at 450 - 500 °C in the absence of oxygen to pyrolysis vapors and solid char particles.[19] Pyrolysis vapors and char are separated by cyclone and vapors are quickly condensed. Residence time in the system is $\sim$ 2 seconds. The process yields 60 - 75 wt% pyrolysis oil, 15 - 20 wt% solid char, and 10 - 20 wt% gases, depending on the type of biomass feedstock used (i.e. sawdust or bagasse). Currently a mixture of 80 % pyrolysis oil and 20 % char is marketed as an industrial fuel to kilns and boilers.[20] Further upgrading to minimize water and oxygen content of the pyrolysis oil is necessary before it can be marketed as a transportation fuel.

Additional commercial ventures utilize similar fluidized bed technologies as Dynamotive. Ensyn operates several biomass pyrolysis plants, including a 150 tonne/day facility in Renfrew, Ontario that was commissioned in 2007.[21] Utilizing a circulating fluidized bed design, termed 'Rapid Thermal Processing', Ensyn converts woody biomass feedstocks to 60 - 80 wt% pyrolysis oil, 12 - 16 wt% solid char, and 12 - 16 wt% gases, similar to the process yields of Dynamotive. The resulting pyrolysis oil is also used an an industrial heating fuel, but is not yet suitable for use as a transportation fuel.

While pyrolysis has the potential to produce liquid fuels from biomass as a renewable transportation fuel source, typical pyrolysis methods have several disadvantages that impair further development. First, pyrolysis reactors can produce large amounts of solid char and non-condensible gases, limiting carbon selectivity to the desired pyrolysis oil. Traditional pyrolysis systems also require external heating to react the biomass. Heating the feed and bed material through the reactor walls can be expensive and inefficient, creating issues during scale-up. Few research groups address this external heat requirement and the resulting process efficiencies when discussing pyrolysis oil production. Pyrolysis oil is also corrosive and non-uniform in composition, making it a poor fuel for typical ignition engines.[15]

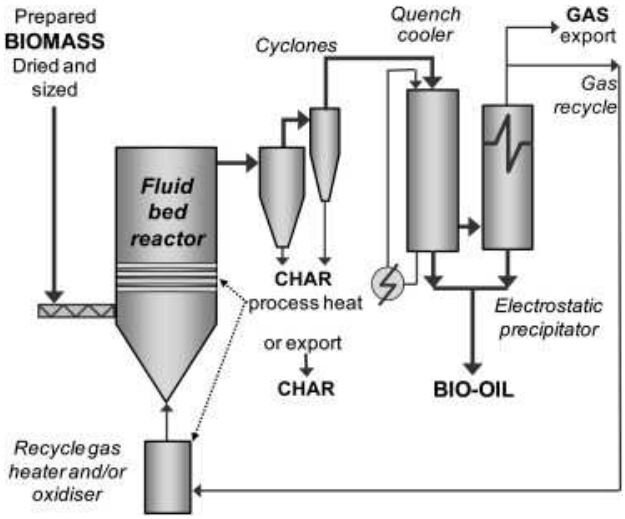

(a) Bubbling Fluidized Bed

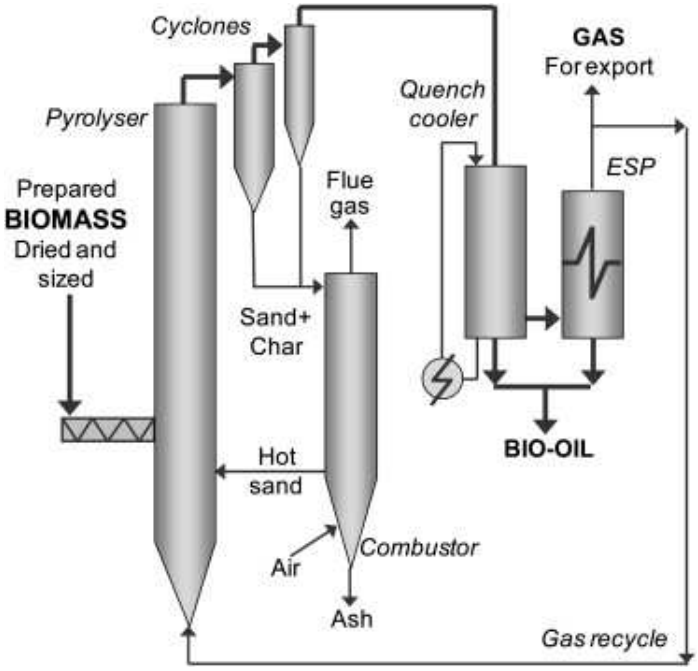

(b) Circulating Fluidized Bed

Figure 1.7: Schematics of fluidized beds.[17] (a) Bubbling fluidized bed. (b) Circulating fluidized bed.

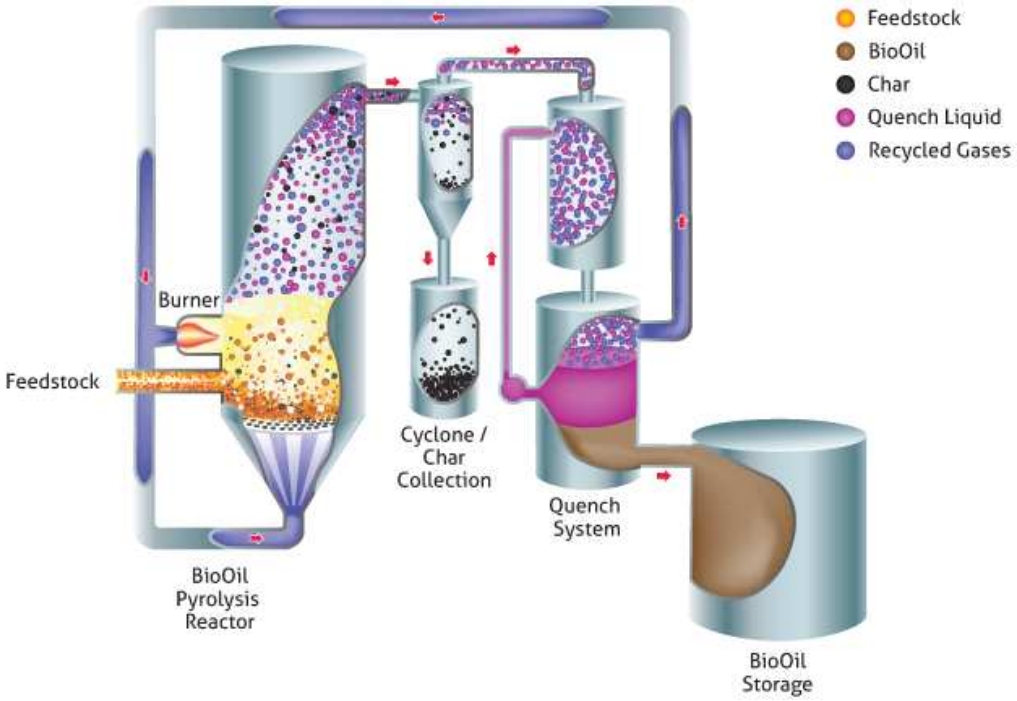

Figure 1.8: Process schematic of the Dynamotive Fast Pyrolysis reactor.

1.2.2 Gasification and Fischer-Tropsch

Gasification uses controlled amounts of oxygen and/or steam, and heat to partially oxidize carbonaceous materials, producing a mixture of hydrogen and carbon monoxide called synthesis gas (syngas). Gasification units generally operate between 600 and 1450 °C and at pressures up to 25 atm.[22,23] Gasification of solid biomass begins with the thermal degradation of the biomass particles to volatile chemicals, which further react with oxygen and water to produce syngas. Oxidation of carbonaceous feedstock is exothermic and produces the heat required by the endothermic reactions. The net process is exothermic and therefore no external heat needs to be applied to the system (termed 'direct gasification'). Since the heat is generated within the reactor, the feedstock can be directly heated, minimizing heat transfer limitations.

After processing in a gasification unit, biomass-derived syngas can be fed to a Fishcer-Tropsch (FT) unit for upgrading to hydrocarbons. The FT unit operates at low (< 250 °C) or (high > 300 °C) temperatures and pressures up to 30 atm, depending on the desired product.[24,25] Syngas, typically at a H_2/CO ratio of 2, reacts over an FT catalyst (iron or cobalt) according to the following reaction:

$$(2n+1)\ H_2 + n\ CO \rightarrow C_nH_{(2n+2)} + n\ H_2O \tag{1.1}$$

Iron, cobalt, nickel, and ruthenium are the four catalysts typically discussed for FT reactions. However, nickel and ruthenium are generally disregarded due to their high methanation activity and very high cost, respectively.[24,26,27] Iron is the most common FT catalyst in commercial applications since it is inexpensive, relatively insensitive to feed contaminants, and has high water-gas-shift activity (Equation 1.2) that eliminates the need for H_2/CO ratio adjustment prior to the FT reactor. Cobalt, while more expensive, has several advantages over iron catalysts: longer lifespan (years vs. months), higher activity, and very high selectivity to normal paraffins. The product hydrocarbons can be hydrocracked to produce a range of transportation fuels (gasoline, diesel, jet).

$$CO + H_2O \rightleftharpoons CO_2 + H_2 \qquad \Delta H = 41 \text{ kJ mol}^{-1} \tag{1.2}$$

Gasification and Fischer-Tropsch processing has several advantages in the conversion of biomass feedstocks. Gasification is robust to a wide variety of feedstocks, including various types of biomass such as trees and grasses.[28,29] The high temperatures at which gasification processes operate and the producer gas is held minimize the formation of aromatics, dioxins, and other similar tar compounds.[30] No significant changes to infrastructure is necessary to use the synthetic gasoline and diesel produced by FT reactions.[29] Additionally, since the syngas is required to be of high quality for FT processing, the product fuel is much cleaner than traditional fossil fuels.

Gasification of biomass and reaction of syngas through FT methods are independently well-understood processes. However, there are very few facilities that incorporate the two processes. Rentech has developed and piloted a 400 gallon per day biomass-to-liquids facility in Commerce City, Colorado.[31] The primary products are renewable jet and diesel fuels for transportation. A 1500 barrel per day facility is planned for construction in Rialto, California after securing a deal to provide renewable diesel to several airlines at the Los Angeles International Airport.[32] Additionally, Rentech has demonstrated a successful test flight with United Airlines using a mixture of renewable and fossil-based jet fuels (60/40) in April, 2010.[33]

Despite several advantages, gasification has disadvantages that severely limit its widespread use on a commercial scale with biomass feedstock. The syngas can contain tar and char byproducts that require expensive downstream cleanup of the syngas. Product gases are also strongly affected by process conditions, such as temperature and pressure.[34] Furthermore, it is not well understood how biomass-related inorganic compounds within the syngas will affect FT catalyst performace as few research

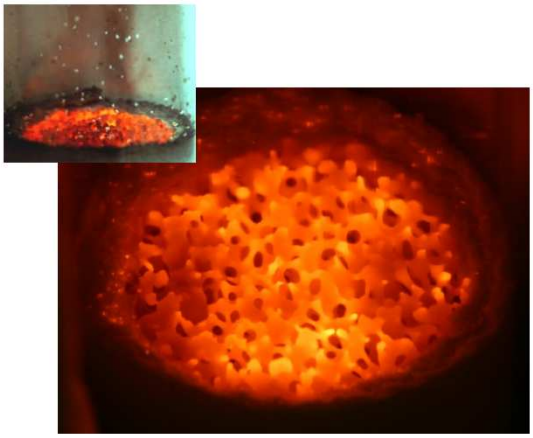

Figure 1.9: Glowing catalyst bed and reaction of cellulose particles on the catalyst surface.[36]

projects focus on this area.[35]

1.2.3 Millisecond Catalytic Autothermal Reforming

Millisecond autothermal catalytic reforming has the potential to provide a simple and inexpensive thermochemical processing route for biomass, alternative to traditional gasification/FT and pyrolysis. The research group of Professor Lanny Schmidt at the University of Minnesota has pioneered this technology using noble metal catalysts on ceramic foam supports in simple reactors that require reaction times typically less than 10 milliseconds (Fig. 1.9). The process is autothermal, can be easily scaled, has rapid startup times, can respond quickly to process fluctuations. This process has been successfully demonstrated to convert a variety of gas and liquid feedstocks to clean syngas or intermediate chemicals with 100 % feedstock conversion. Recent millisecond autothermal reforming of solid cellulose particles, a model for biomass, has shown 100 % conversion, no tar formation, and high adjustable selectivities to hydrogen and carbon monoxide.

In the early 1990's, autothermal catalytic reforming was first investigated to reform methane to clean syngas in air and at atmospheric pressure.[37] Methane was reacted over rhodium and platinum catalysts prepared on 30 - 50 ppi (pores per linear inch) α-Al_2O_3 monoliths with 100 % conversion according to the overall reaction,

$$CH_4 + \tfrac{1}{2}O_2 \rightarrow CO + 2H_2 \qquad \Delta H^\circ = \text{- } 35.6 \text{ kJ mol}^{-1} \tag{1.3}$$

With residence times between 10^{-4} and 10^{-2} seconds and temperatures of 827 to 1127 °C, hydrogen and carbon monoxide selectivities of 90 and 96 % could be achieved, respectively. These results presented an efficient and potentially economic syngas production route, alternative to the slow and endothermic traditional steam reforming processes.

Other noble and transition metals were investigated for use as autothermal reforming catalysts.[38] Rhodium was found to be the best catalyst for syngas production with high stability and resistance to coke formation. Platinum's ability to oxidatively dehydrogenate molecules was ideal for olefin production. Iridium, nickel, palladium, cobalt, rhenium, ruthenium, and iron were also examined but found to have lower selectivities or deactivate by coke and/or metal volatilization. Further research has confirmed the high selectivity to syngas over Rh, as well as the advantages provided by the addition of cerium metal and a γ-Al_2O_3 washcoat to the catalyst.[39–42]

Catalytic autothermal reforming was found to produce high and tunable selectivities to syngas as well as a variety of olefins by adjusting the fuel and air feed ratio. Higher hydrocarbon fuels such as alcohols, cyclohexane, n-hexane, isooctane, gasoline, and diesel, among other alkanes, were all successfully converted, exemplifying the consistence and robustness of the process.[42–44] All fuels investigated were shown to achieve at least 80 % selectivity to syngas or 50 % to olefins, depending on the catalyst, feed gas compostion, and total flow rate.

Recently, research focus has shifted to the utilization of biomass as a renewable source of carbon for fuels and energy. Fermentation of biomass to alcohols can be an effective way to produce liquid fuel, but is slow and inefficient. The pyrolysis of biomass is also a promising technology and produces liquid products, but the pyrolysis oil is highly complex and requires upgrading. Current biomass gasification technologies require three energy intensive steps: volatilization of the feed, cleanup of carbon-rich tars from the syngas product, and water-gas-shift reaction to alter the H_2/CO syngas ratio before processing to liquid fuels by Fischer-Tropsch. Catalytic autothermal reforming is capable of completely converting 300 μm cellulose particles to clean syngas in under 30 ms without tar formation and with the ability to tune the syngas ratio by adjusting operating conditions.[36,45] This technology may by extended to perform autothermal oxidative pyrolysis, providing an efficient way to convert lignocellulosic biomass to liquid fuels and chemicals.

Lignocellulosic biomass represents a major renewable resource, however traditional processing methods are frequently inefficient and unprofitable. Therefore, a new cat-

alytic process is proposed to convert biomass into useful fuels and chemicals. The evolution of catalytic autothermal reforming and its ability to process gases, volatile liquids, nonvolatile liquids, and finally solids, shows potential to be successful in such a process. Autothermal oxidative pyrolysis could have several advantages over traditional biomass processing methods to produce liquid products. This process can potentially produce chemicals with higher selectivity in a fast and inexpensive way. With millisecond residence times, operations would not require large-scale facilities and could be operated locally. With small, local facilities, less material would need to be collected to be economical and fewer transportation requirements would reduce costs. As an autothermal process, no expensive heat inputs are required, unlike traditional pyrolysis. The solid catalytic bed facilitates heat transfer within the reactor and the plug flow properties prevent radial product variations. The potential to produce liquid fuels in a single-stage reactor is also beneficial over the intensive multi-step processing of gasification and Fischer-Tropsch.

CHAPTER

TWO

REACTIVE BOILING OF CELLULOSE FOR INTEGRATED CATALYSIS THROUGH AN INTERMEDIATE LIQUID[1]

Advanced biomass processing technology integrating fast pyrolysis and inorganic catalysis requires an improved understanding of the thermal decomposition of biopolymers in contact with porous catalytic surfaces. High speed photography (1000 frames per second) reveals that direct impingement of microcrystalline cellulose particles (300 μm) with rhodium-based reforming catalysts at high temperature (700 °C) produces an intermediate liquid phase that reactively boils to vapors. The intermediate liquid maintains contact with the porous surface permitting high heat transfer (MW m^{-2}) generating an internal thermal gradient visible within the particle as a propagating wave of solid to liquid conversion. Complete conversion to liquid yields a fluid droplet on the catalyst surface exhibiting a linear decrease in droplet volume with time leaving behind a clean surface absent of solid residue (char). Under specific interfacial conditions, conversion with large cellulosic particles on the length-scale of wood chips (millimeters) occurs continuously as generated liquid and vapors are pushed into the porous surface.

[1]Portions of this chapter appear in P.J. Dauenhauer, J.L. Colby, C.M. Balonek, W.J. Suszynski, L.D. Schmidt, "Reactive boiling of cellulose for integrated catalysis through an intermediate liquid," *Green Chemistry* **11** (2009) 1555-1561.

2.1 Introduction

The search for advanced processing technologies capable of efficiently converting biomass to fuels and chemicals has led to the combination of solid biomass pyrolysis and catalytic processes. Direct utilization of catalysts with biomass requires the large biopolymers of lignocellulose to be broken down to species capable of interacting with catalytic active sites while maintaining catalyst integrity.[46] Emerging technologies have shown that high temperature decomposition (e.g. fast pyrolysis) pairs well with the use of inorganic catalysts due to similar processing rates, occurring orders of magnitude faster than existing biological processes (e.g. enzymatic hydrolysis).[47,48] Recently, Huber et al. demonstrated mixed pyrolysis/catalysis by rapid heating of cellulose particles in the presence of aluminosilicates (e.g. ZSM-5), which both cracked large biopolymers and converted the organic intermediates to highly desirable gasoline-like aromatic species.[49] Additionally, Schmidt et al. demonstrated that alumina-supported reforming catalysts combined with cellulose pyrolysis efficiently produce synthesis gas (H_2 + CO) and allow for selective tuning of product ratios.[36,45]

However, the mechanism by which cellulose thermally decomposes to volatile organic compounds (VOCs) on catalytic surfaces for downstream processing is unknown, hindering advancement of catalytic biomass reactors. The process generally occurs by cellulose particles impacting a high temperature surface, driving endothermic pyrolysis of the polymer structure to VOCs. These products are then convected from the particle to the neighboring solid, interacting chemically with the catalyst surface. Unknowns within this complex set of interacting phenomena are the dominant method of heat transfer to particles (convection, radiation, or conduction), the state of the cellulose particle over the course of conversion (solid or liquid), the extent of particle homogeneity, the physical interaction between the particle and surface, and the rate limiting phenomenon (pyrolysis or some mode of heat transfer). The complex nature of the system prevents substantial understanding by transport models integrating particle, surrounding gas, and surface chemistry.

This paper examines the conversion of cellulose particles in direct contact with high-temperature catalytic reforming catalysts in the presence of oxygen. Small, pure particles of cellulose on the length scale of 10 - 400 μm are observable under significant optical and temporal magnification (1000 frames per second). Variation of the catalytic surface between realistic porous foam supports and experimental flat surfaces permits a clear observation of the particle/surface interaction. Additionally, dimensional tracking of particles with time reveals the extent of conversion from solid

cellulose to intermediate phases, and it permits an indirect measurement of surface-to-particle heat transfer.

The results show that micron- to millimeter-scale particles decompose to an intermediate liquid droplet before further decomposing and boiling completely to volatile species. The intermediate particle predominately exists as a heterogeneous mixture of solid and liquid with linear reduction in height with respect to time indicating a potential for continuous processing of larger particles. Therefore, additional experiments consider high temperature reforming catalysts in contact with large particles (rods, 7 x 7 x 500 mm)that extend away from the surface permitting examination of continuous catalytic processing of cellulose. The processing rate was measured as a function of the interfacial temperature and the applied pressure between the cellulose feedstock and the catalytic surface.

2.2 Experimental

Catalytic reforming of cellulose particles was examined in three separate experimental apparatuses due to the significant difference in cellulose feedstock dimensions (micron- versus centimeter-scale) and catalyst supports (foam versus flat surfaces).

2.2.1 Catalyst preparation

The catalyst in Figure 2.1(a) was supported on an 80 pores per inch (ppi) α-Al_2O_3 foam cylinder 17 mm in diameter and 10 mm in length with visible struts and tortuous pores. The flat catalytic surface (wafer) in Figure 2.1(b) was prepared by compressing α-Al_2O_3 powder into a disk 2 mm thick and 22 mm wide, sintering at 800 °C for 30 hrs and 1180 °C for 8 hrs. Both catalysts were prepared by wet impregnation of Rh-Ce (2.5 wt% of the support each), drying, and calcination at 600 °C for 6 hrs.

2.2.2 Micron-scale particle processing on foam supports

Small particle (< 500 mm) autothermal conversion was examined in a 20 mm I.D. quartz reactor tube described previously.[36] Three foams were stacked on top of each other along with a fourth blank 80 ppi foam on the bottom, wrapped in ceramic paper (for friction fit), and slid into the reactor tube. A type-K thermocouple was inserted 10 mm from the leading surface. A 1 cm pyrex tube combined with a size 20 pyrex reactor tube end cap provided the connection between the reactor and a cellulose hopper necessary for solid particle delivery. A quartz light pipe was inserted through

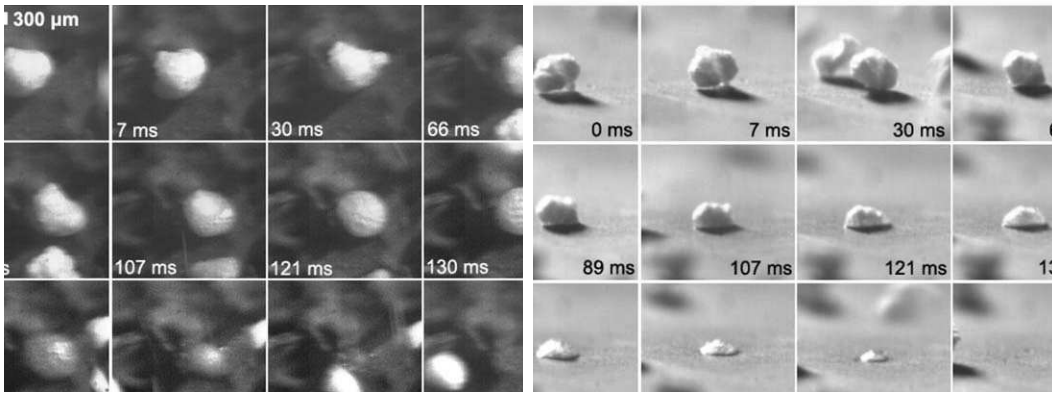

(a) (b)

Figure 2.1: Millisecond visualization of cellulose particle decomposition. a, Microcrystalline cellulose particles ($\sim$ 300 μm) reacting to form volatile species in air on 700 °C Rh-Ce/α-Al_2O_3 have been visualized with high-speed photography (1000 frames/second) on an 80 ppi α-Al_2O_3 foam support at C/O = 1.15. b, A separate experiment examined cellulose decomposition on a smooth 700 °C Rh-Ce/α-Al_2O_3 disk support. Particles exhibit poor surface contact (0.7 ms) before forming a liquid intermediate species capable of intimately contacting the catalytic surface (66 - 176 ms). The molten intermediate liquid appears to nucleate volatile species (107 - 130 ms) before completely converting without char formation (171 - 176 ms).

the end cap and contacted the leading surface providing a light sample to an optical pyrometer. The cellulose particles (avg. 315 μm) stored in an acrylic tube hopper ($\sim$ 10 cm diameter) were pushed into a feed tube (0.25 inch I.D.) using a 0.25 inch wood auger driven in reverse with a servo motor permitting variable feed rates. Air was supplied by a gas cylinder and metered by a flow control valve calibrated with a bubble column.

The quartz reactor was wrapped in a resistive heater controlled by a variac and wrapped in insulation. Autothermal operation was initiated with air flow of 1.5 standard liters per minute (SLPM) by heating the reactor externally to $\sim$ 400 °C at which point particles were continuously delivered to the surface. Steady autothermal operation was obtained within five minutes, and the heater was turned off. Varying surface temperatures were obtained by varying the air flow rate or cellulose flow rate. The high speed camera was placed $\sim$ 45 ° from the surface normal, obtaining light through the curved quartz reactor wall. Light for high-speed photography was provided to the front of the particles. Figure A.1 of the supplementary information depicts the experimental setup.[†]

[†]Supplementary information in Appendix A

2.2.3 Micron-scale particle processing on flat supports

Particles of cellulose and sucrose pyrolyzing on a flat catalytic wafer (Rh-Ce/α-Al_2O_3, 2.5 wt% each) were observed using a high speed camera. A quartz reactor tube was fixed in place 12 cm above the catalytic wafer by metal clamps. Air was supplied by a high pressure gas cylinder through a needle valve, and particles of solid material were applied down the reactor tube to the catalytic surface from a side tube sealed with a pushrod. A quartz fiber light pipe delivering light to an optical pyrometer was attached through the quartz reactor such that it contacted the catalytic surface. A butane torch was clamped directly below the catalytic wafer such that its distance was adjustable to control the surface temperature. The high speed camera was placed ~ 80 ° from the surface normal, obtaining light through a flat pyrex protector plate. Light for high-speed photography was provided from behind the particles. Figure A.9 of the supplementary information depicts the experimental setup.[†]

2.2.4 Centimeter-scale particle processing

Large particles of cellulose (7 x 7 x 500 mm) were prepared by pulping a mixture of mainly hemicellulose and cellulose (79.8 % glucan, 19.5 % xylan, 0.3 % lignin, 0.4 % ash) in deionized water, drying the pulp in a mold (50 x 50 x 1 cm), and cutting the dried block to the desired dimensions.

Processing of large particles occurred on catalytic foams in a 20 mm I.D. reactor described above with the addition of a 1 cm I.D. pyrex tube extending ~ 1 m from the top of the reactor. Cellulose rods were pressed against the catalytic foam from above by weights placed within the sealed tube. The bulk surface temperature was varied from $\sim$ 600 - 900 °C by varying the dilution of methane and oxygen feed gas with the constraint that C/O = (fuel C)/(atomic oxygen from O_2) = 0.8 and total gaseous flow rate was 5.0 SLPM. Gaseous reactor effluent was collected and measured by gas chromatography to validate rod conversion rates. Figure A.18 of the supplementary information depicts the experimental setup.[†]

Experiments were setup such that a rod of cellulose, 500 mm in length, was suspended 5 cm above the foam catalysts by a pin extending out of the reactor through a sealed port. Nitrogen, oxygen, and methane, flowing around the suspended cellulose and through the catalyst, were heated by an external torch applied to the reactor wall near the catalyst to initiate autothermal reforming. The experiment was initiated by removing the pin permitting the cellulose rod to fall to the catalyst surface while simultaneously adjusting the oxygen/nitrogen/methane flow rates to

satisfy C/O = 0.8. The rate at which the cellulose sample ablated on the catalyst was measured by recording the movement of the cellulose end as it passed graduations on the feed tube with time. Downstream gas samples were collected and analyzed by gas chromatography for carbon monoxide and carbon dioxide to verify carbon processing rates.

2.2.5 High-speed photography

Digital video was obtained by focusing a Photron Fastcam Ultima APX with color image through a curved quartz reactor or pyrex plate. The four optical devices placed in series to obtain the presented magnification were: 1) a Micro-NIKKOR 105 mm lens by Nikon of Japan, 2) a Nikon PN-11 extension tube by Nikon of Japan, 3) a Kenko extension tube for Nikon/AF 36 mm by Kenko of Japan, and 4) a Kenko 2x Teleplus MC7 telephoto extension tube by Kenko of Japan. Light was provided to the catalyst necessary for high speed imaging by a Solarc Light LB-50 by Welch Allyn, Inc. of New York, USA.

Visualization videos of particle conversion on catalytic foams were collected through the 2 mm thick quartz reactor tube, while particles on wafers were obtained through 0.5 cm pyrex glass used to protect the camera. Particle sizes were obtained by relating the measured number of pixels within a frame to known sizes of objects (thermocouple or quartz light pipe).

2.3 Results and discussion

In the integrated pyrolysis/catalysis process examined here, particles of cellulose in air impact a glowing ($\sim$ 700 °C) Rh-Ce/α-Al_2O_3 foam catalyst in a quartz reactor tube and pyrolyze completely under extreme thermal gradients to VOCs at millisecond time-scales. The VOCs flow into the catalyst, react with oxygen exothermically, and generate sufficient heat to maintain the catalyst at 700 - 800 °C driving endothermic pyrolysis in an overall exothermic, autothermal process.[36] This arrangement has been shown to efficiently produce equilibrium selectivity to clean synthesis gas without detectable char formation.[45]

Through the use of ultra high-speed imaging (1000 frames per second) we definitively demonstrate the existence of a liquid intermediate during the rapid heating of cellulose particles. Figure 2.1(a) shows the conversion of a single $\sim$ 300 μm diameter cellulose particle on an operating foam catalyst at $\sim$ 700 °C from $\sim$ 45 ° relative

to the catalyst surface. After coming to rest on the surface (0 ms), the particle appears to initially rotate (7 & 30 ms) before the appearance of a smooth liquid layer along the bottom right edge (66 ms) distinguishable by its specular highlight. The development of a liquid phase continues to progress from the bottom of the particle (89 & 107 ms) until the entire particle exists as a hemispherical liquid droplet (121 ms). Clearly visible within the liquid layer are gaseous bubbles developing within the liquid sphere (107, 121, and 130 ms) moving to the surface and eventually the surrounding gas until the entire particle volatilizes leaving a clean surface (171 ms).

In a different experiment (Fig. 2.1(b)) we examined the impact of cellulose particles in air on a flat Rh-Ce/α-Al_2O_3 surface heated from below by a butane torch to 700 °C. Viewed at 80 ° from the surface normal, the particle initially exhibits poor surface contact (0.7 ms) before forming a liquid clearly in intimate contact with the catalyst (66 - 107 ms). Conversion to a liquid at 130 ms produces a hemispherical shape, which fully volatilizes leaving a clean surface at 176 ms.

The existence of a liquid intermediate from cellulose, often referred to as "active cellulose," has elicited controversy.[50–53] Several multi-step cellulose decomposition mechanisms include an intermediate cellulose-like biopolymer of reduced degree of polymerization to fit empirical data.[54–57] Further depolymerization and fragmentation to organic liquids (e.g. methanol, hydroxyacetaldehyde, levoglucosan) dominates around 500 °C in seconds, while higher temperatures favor gases (e.g. CO, H_2, CO_2) and lower temperatures favor dehydration chemistry to solid char. Previous evidence for depolymerized liquid intermediate formation was observed by showing that cellulose rods, similar to ice or meltable polymers, can be ablated on hot surfaces.[58] A different set of experiments exposed small particles of cellulose to very short durations of applied heat and observed solid products with smooth surfaces, indicative of intermediate liquids.[51,59] However, the present evidence clearly shows a liquid state forming spherical conformations and interacting with surfaces and other particles.[†]

Dimensional tracking of several particles (Fig. 2.2(a)) on the catalytic foam shows that the conversion time is directly proportional to the square of the initial particle diameter, even for particles as small as 100 μm. Furthermore, measurements shown in Figure 2.2(b) (height and width) depict the lifetime of both particles in Figure 2.1 and reveal three stages in particle volatilization. In region A, the particle exhibits poor surface contact and no apparent change in size. In region B, intermediate liquid formation propagates up the particle, coinciding with a nearly linear reduction in height. Finally, in region C, the liquid droplet undergoes further pyrolysis to gases and volatile organics, exhibiting constant decrease in width and volume as shown in

Figure A.13 of the supplementary information.†

The nature of the intermediate liquid has enormous implications on the rate of heat transfer from catalytic surfaces for thermal conversion of cellulosic materials. Particle pyrolysis is categorized in two ways, according to the dominant mode of heat transfer (internal or external) and the rate limiting phenomenon (chemical conversion by pyrolysis, product gas mass transfer or heat transfer).[60] In this case, the thermal decomposition chemistry of cellulose above 400 °C is sufficiently fast to never be rate limiting for particles on the order of ten microns and larger.[61,62] Additionally, the chemistry observed in Figure 2.1 and the data in Figure 2.2(b) clearly shows that solid to intermediate liquid conversion dominates the conversion time eliminating gas phase product mass transfer from being rate limiting. Therefore, conversion can only be limited by heat transfer to the particle by radiation, convection, conduction from the surface, or internal particle heat transfer (Fig. 2.2(a)).

The behavior of total conversion time as directly proportional to the square of the initial diameter has previously indicated internal heat transfer limitation, thereby requiring the ratio of external to internal heat transfer (described by the Biot number, Bi = hD/k) to be large (Bi > 10) where k is the thermal conductivity of cellulose, D is the particle diameter, and h is the external heat transfer coefficient.[53,63] Neither maximum radiation, $\varepsilon = 1$ and T_{inf} = 700 °C ($10^{-2} < Bi_{radiation} < 10^{-1}$), nor gas convection calculated from the Ranz and Marshall correlation ($Bi_{convection} \sim 1$) are sufficiently large to limit the system by internal particle heat transfer.[64] External heat transfer from the surface by conduction can be estimated from

$$q_{Conduction} = \rho \frac{dV}{dt} \frac{\triangle H_{pyrolysis}}{A_{Contact}} = h_{Conduction}(\triangle T) \tag{2.1}$$

The volume of the liquid droplet, V, in each frame was calculated by assuming the droplet was a portion of a sphere as shown in Figure A.12 of the supplementary information.† This method reveals that the change in volume, dV/dt, of the liquid droplet (Fig. 2.2, region C) is constant as shown in Figure A.13 of the supplementary information.† By calculating dV/dt from ∼ 200 measurements of several particles (Fig. 2.2, region C) and assuming $\triangle H_{pyrolysis}$ = 538 kJ kg^{-1}, ρ = 650 kg m^{-3}, the heat flow, $q_{Conduction}$, is 3.4 ± 0.2 MW m^{-2} as shown by a histogram in the Figure 2.2(b) inset of all experimental measurements.†[65] Further assuming the intermediate liquid is approximately the fusion temperature described by Lede (739 K), then △T ∼ 200 °C, and $h_{surface}$ must be (1.7 ± 0.1) x 10^4 W m^{-2} K^{-1}, satisfying Bi ∼ 10 and concluding that surface heat transfer is overwhelming and dominant.[58] Convection

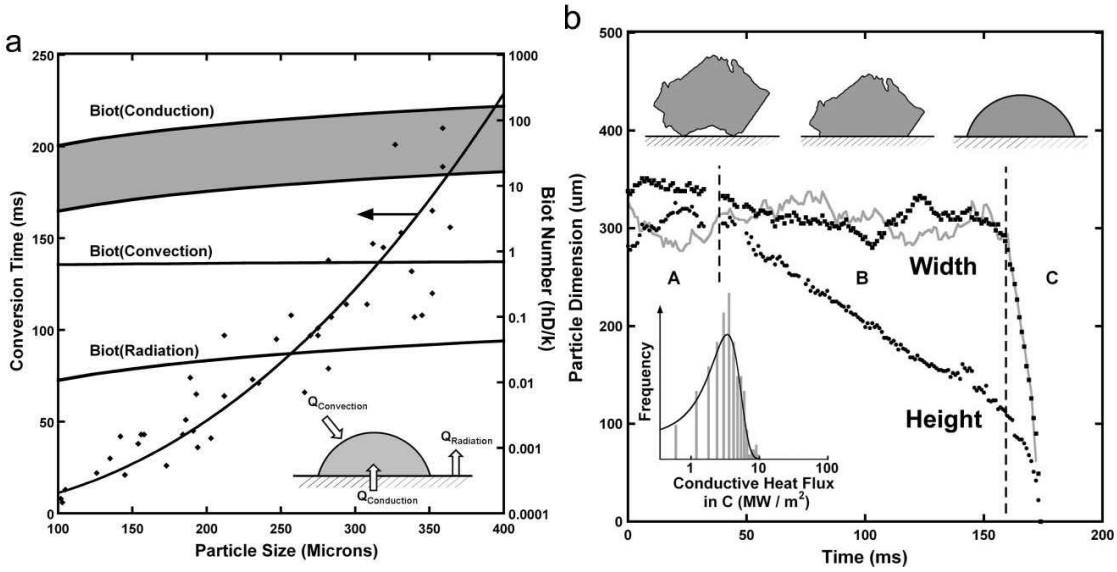

(a) (b)

Figure 2.2: Dimensional tracking of cellulose particle conversion for surface heat flux estimation. (a) The time for observed particles to completely convert was proportional to the square of the initial particle diameter (T_c =k$D_\circ^2$) consistent with internal particle heat transfer control thereby requiring the ratio of external to internal heat transfer (Biot Number) to be larger than $\sim$ 10. Only a conductive heat transfer coefficient of h = 10^4 - 10^5 W m^{-2} K^{-1}(shaded region) can result in a Biot >> 1 describing the thermal and reacting wave observed in Figure 1. (b), The conversion of a single cellulose particle ($\sim$ 300 μm) on a 700 °C surface appears to occur in three phases (A, B, and C) shown as a cartoon and described by height and width for flat surfaces (data points) and foams (grey line). (A) Initial impact with a catalytic surface exhibits very poor surface contact and slow initial heating. (B) Particle surface contact points eventually pyrolyze to a biopolymer liquid (active cellulose) which can contact the surface and permit rapid pyrolysis with a linear decrease in height. Gas nucleation was observed in the height around 140 - 150 ms. (C) An active cellulose drop exhibits linear decrease in volume (and radius of curvature) with time and an enormous heat flux of 3.4 $\pm$ 0.2 MW m^{-2} (inset).

and radiation are included by this method of estimating the heat transfer rate, but their magnitude is on the order of the experimental error or less.

The mechanism permitting high conductive heat transfer to the particle can be observed in Figure 2.1. Droplets of volatile fluids such as glycerol, heptane, or dodecane commonly exhibit film boiling (the Leidenfrost effect) which lift them off very hot surfaces, slowing conductive heat transfer.[†66,67] However, experiments with cellulose (and additional experiments with sucrose available as Figures A.15 and A.16 in the supplementary information[†]) show that the liquid intermediate on a $\sim$ 700 °C catalytic surface maintains contact, dramatically improving conductive heat transfer to the particle.

High heat flux through an intermediate liquid species has unique implications for the chemistry of cellulose decomposition. As observed in Figure 2.1, cellulose conversion occurs as a thermal wave passing through the particle. For small particles considered here ($<$ 500 μm), no portion of the particle exists sufficiently long at low temperature ($\sim$ 300 - 400 °C) for char forming chemistry to occur appreciably. However, as a particle increases in size to 1 mm or greater (e.g. wood chips), it becomes unavoidable that a portion of the solid biopolymer away from the hot surface will exist within the char-producing temperature range. One demonstrated solution to this fundamental problem utilizes high heat transfer rates between a large (thermally-thick) particle and a hot non-catalytic surface moving relative to the sample to mechanically sweep away pyrolysis products.[68–70] However, more simple processing of cellulose can occur with a stationary surface utilizing a catalyst on a porous surface.

A different experiment with cellulose (Fig. 2.3(a)) demonstrates that high heat flux through the liquid intermediate on catalytic surfaces can also process large rods (7 x 7 x 500 mm) rapidly. By pressing a cellulose rod directly onto a Rh-Ce/Al_2O_3 foam co-reforming methane, the rate of cellulose pyrolysis was measured as a function of applied pressure (12.36 kPa) and bulk catalyst surface temperature. Below a surface temperature of about 750 °C, the rod exhibited the expected behavior of intermediate char formation which permitted the rod to pass through the catalyst only as fast as the intermediate char gasification rate, $\sim$ 50 kg m^{-2} hr^{-1}. However, above approximately 750 °C, the rod processing rate was considerably higher ($>$ 300 kg m^{-2} hr^{-1}), linear in temperature, and a strong function of applied pressure, indicating that pyrolysis at the leading cellulose edge is the rate limiting step.[71]

Figure 2.3(b) describes a qualitative temperature distribution consistent with experimental observations. As heat flow from the surface (Q_{flux}) increases, the thermal gradient within the solid cellulose particle increases and the length of cellulose (a in

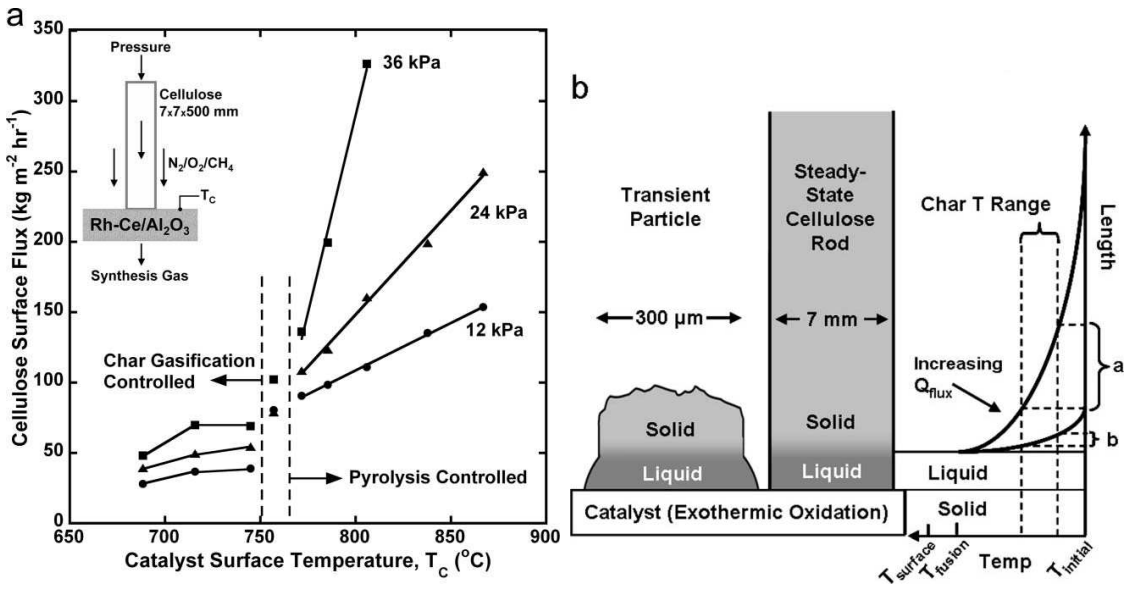

(a) (b)

Figure 2.3: Large particle conversion on catalytic surfaces. a, Cellulose particles (7 x 7 x 500 mm) reacted to synthesis gas on a Rh-Ce coated alumina foam by direct impingement in the presence of oxygen. The interface pressure was varied from 12.36 kPa, and the catalyst surface temperature was controlled by methane catalytic partial oxidation at C/O = 0.8 diluted with varying amounts of N_2 (total gas flow rate was a constant 5 SLPM). Cellulose conversion exhibited a distinct change in conversion rate (surface flux) between the char gasification rate control and linear pyrolysis rate control around 750 °C. Error bars (not shown) of ± 21 kg m^{-2} hr^{-1}represent a 95% confidence interval. b, The form of the cellulose temperature profile is depicted as a function of the rod length. As heat flux, Q_{flux}, from the catalyst through cellulose increases, the thermal gradient increases (becomes sharper). At high heat flux from the surface, Q_{flux}, the sharp temperature gradient permits very little (length b) of the extended cellulose rod to exist within the char-forming temperature range (∼ 300 - 400 °C). However, as $T_{surface}$ decreases below ∼ 750 °C, Q_{flux} decreases and more of the extended rod (length a) forms char such that char removal by gasification becomes the rate-limiting process.

Fig. 2.3(b)) existing within the char-forming temperature region decreases (b in Fig. 2.3(b)). At heat fluxes present in the described experiments, the thermal gradient within the cellulose rod is sufficiently steep to result in negligible char formation.

The decomposition of cellulose at the rod tip in contact with the catalytic surface likely undergoes very complex multiphase rearrangement. As solid cellulose decomposes to intermediate liquid, it is pushed into the pores of the catalyst. Additionally, individually developed fluid droplets are likely to coalesce to larger ones.

This phenomenon has been observed on catalyst foams when two small particles, each ~ 300 μm, come to rest near each other and decompose to an intermediate liquid during the same period of time as shown in Figure 2.4. Within 80 ms of the first particle landing, the particle on the right is fully liquid and the particle on the left is mostly liquid. Within a few milliseconds, the two liquid droplets combine to form a single particle. The most violent motion forming the bridge between the two particles occurs faster than a single millisecond and can only be inferred from the frames and video. The combined particle continues to form a spherical shape in the next 25 ms before completely volatilizing at 180 ms.

The existence of a processing regime capable of combining pyrolysis of biomass particles with catalysis facilitates the development of new reactor designs and chemistries. Many of the conclusions developed here regarding the liquid intermediate, high heat transfer rates, and large particle processing can be extended to previous non-catalytic biomass reactors (e.g. biomass ablative vortex reactor).[72] Additionally, new combinations of pyrolysis and catalysis become more viable, including mixed pyrolysis/hydrogenation, pyrolysis/hydrodeoxygenation, or pyrolysis/cracking. However, additional research will be required to more fully describe the solid-nonvolatile fluid heat transfer mechanism as well as the operating parameters that control the large particle regime transition.

2.4 Conclusions

High speed photography reveals that direct impingement of microcrystalline cellulose particles with Rh-based reforming catalysts at 700 °C produces an intermediate liquid phase that reactively boils to vapors. The intermediate liquid maintains contact with the catalyst surface permitting high heat transfer (3.4 MW m^{-2}) generating an internal thermal gradient visible within the particle as a wave of solid to liquid conversion. During the period of solid to liquid conversion, the particle height decreased linearly with time. Complete conversion to liquid yields a fluid droplet on the catalyst

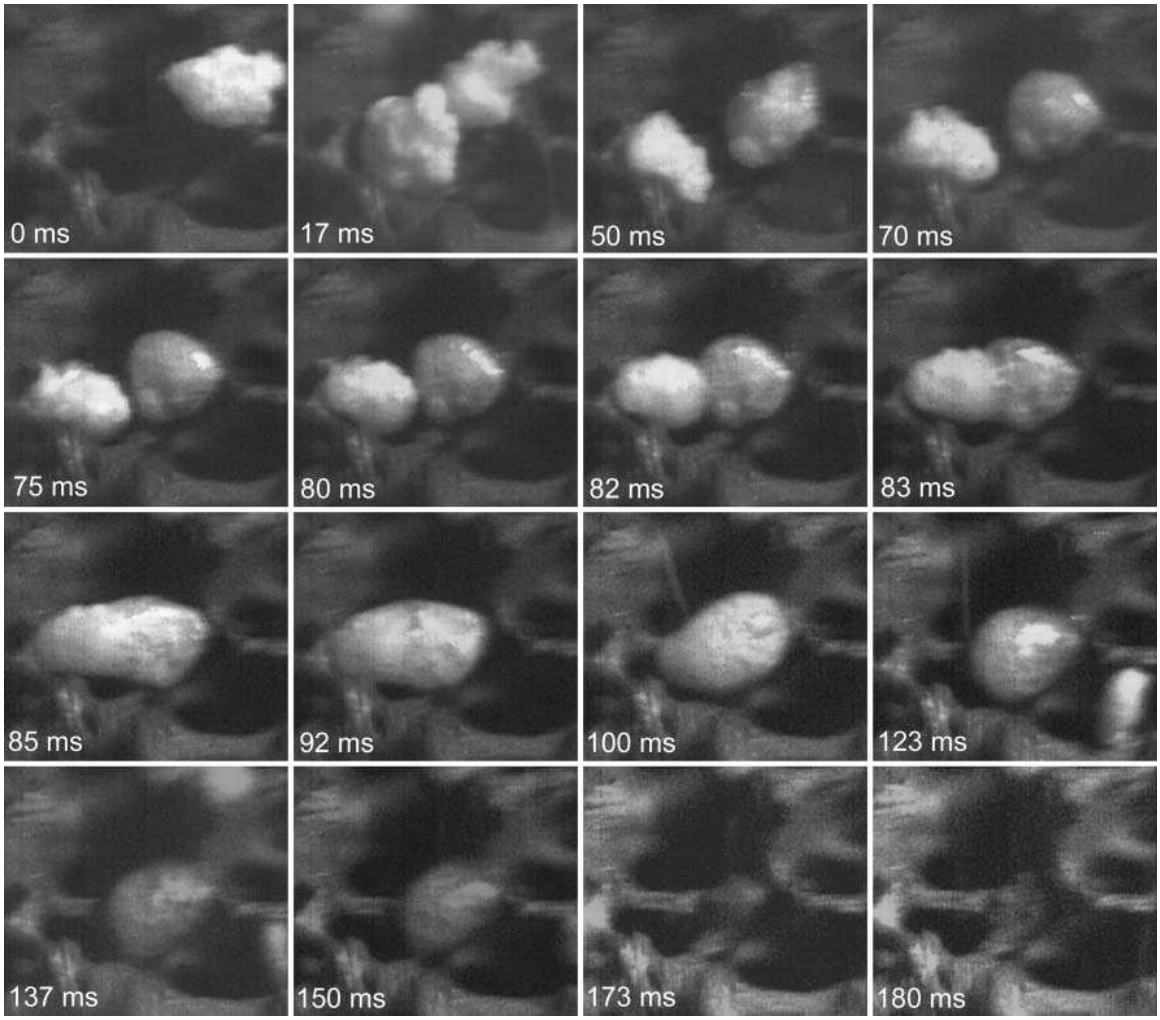

Figure 2.4: Millisecond coalescence of cellulose intermediate liquid droplets. Two microcrystalline cellulose particles ($\sim$ 300 μm each) reacting to volatile species in air on 700 °C Rh-Ce/α-Al_2O_3 surface have been observed with high-speed photography on an 80 ppi α-Al_2O_3 foam support at C/O = 1.15 from 45 ° from the surface normal) with temporal resolution of one millisecond. Two particles (coming to rest at 0 and 17 ms) convert to a liquid. The liquid droplets coalesce rapidly (82.85 ms) to a single particle which reactively boils to volatile species observable as gaseous bubbles (100 - 137 ms) leaving a clean surface (180 ms).

surface exhibiting linear decrease in droplet volume with time leaving behind a clean surface absent solid residue (char). Under specific interfacial conditions, conversion with large cellulosic particles on the length-scale of wood chips occurs continuously as generated liquid and vapors are pushed into the porous surface.

2.5 Acknowledgments

We acknowledge funding from the U.S. Department of Energy and the Initiative for Renewable Energy and the Environment (IREE) at the University of Minnesota. We also acknowledge assistance from Professor Ulrike Tschirner in preparing and analyzing cellulose samples. We also thank Jennifer Dederich for photographic assistance.

CHAPTER

THREE

AUTOTHERMAL OXIDATIVE PYROLYSIS OF MONOAROMATICS OVER NOBLE METALS [1]

To examine the possiblity of processing lignocellulosic biomass by oxidative pyrolysis, model compounds are vital to simplify experiments and provide clear insights. As discussed in Section 1.1.3, lignin is a complex structure of aromatics and a variety of functional groups. Benzene, toluene, ethylbenzene, cumene, and styrene were chosen as lignin surrogates for the research presented in this chapter. The autothermal oxidative pyrolysis these monoaromatics were independently studied over five noble metal-based catalysts: Pt, Rh, Rh/γ-Al_2O_3, Rh-Ce, and Rh-Ce/γ-Al_2O_3, as a function of carbon-to-oxygen feed ratio. The Rh-Ce/γ-Al_2O_3 catalyst exhibited the highest feedstock conversion as well as selectivities to both synthesis gas and hydrocarbon products (lowest selectivities to H_2O and CO_2). Experimental results demonstrate a high stability of aromatic rings within the reactor system. Benzene and toluene appear to react primarily heterogeneously, producing only syngas and combustion products. Ethylbenzene and cumene behaved similarly, with higher conversions than benzene and toluene, and high product selectivity to styrene, likely due to homogeneous reactions involving their alkyl groups. Styrene exhibited low conversions over Rh-Ce/γ-Al_2O_3, emphasizing the stability of styrene in the reactor system.

[1]Portions of this chapter appear in C.M. Balonek, J.L. Colby, L.D. Schmidt, "Millisecond catalytic reforming of monoaromatics over noble metals," *AIChE Journal* **56** (2010) 979-988.

3.1 Introduction

Aromatic compounds are frequently found in the polymer structures of biomass, particularly in the lignin component. An understanding of their catalytic degradation would provide insight for the processing of biomass through oxidative pyrolysis. Research involving the high temperature pyrolysis or oxidation of monoaromatic species is limited. Brooks *et al.* , Alzueta *et al.* , and Da Costa *et al.* studied the gas phase pyrolysis and oxidation of benzene.[73–75] Brooks *et al.* also studied gas phase ethylbenzene pyrolysis and observed hydrogen and styrene as the primary products. [76] Pant *et al.* observed toluene pyrolysis with steam to produce methane, benzene, bibenzyl, and carbon oxides with coke yields $\leq$ 10.4 %.[77]

Noble metal-based catalysts have previously been shown to convert a variety of fuels autothermally on millisecond time scales with up to 100 % conversion and no coke formation.[36,42,45,78] This work examines the effect of catalyst, support, and carbon-to-oxygen feed ratio during the autothermal oxidative pyrolysis of monoaromatics (benzene, toluene, ethylbenzene, cumene, and styrene) over noble metal-based catalysts (Rh and Pt) to investigate the behavior of aromatic rings and the role of substituted groups within the reactor system.

3.2 Experimental

Monoaromatics were autothermally reformed in a 19 mm ID quartz tube reactor system (Fig. 3.1). Nitrogen and oxygen at air stoichiometry were fed by Brooks 5850i mass flow controllers and monitored using LabView 6.1. Liquid monoaromatics were fed by an ISCO 500D syringe pump ($\pm$ 0.001 mL min^{-1}) and completely vaporized using a glass nebulizer (Precision Glassblowing) and a 20 cm heated bed of glass beads (200 $\pm$ 5 °C) 27 cm upstream of the catalyst. Liquid flows were typically 1 to 3 mL min^{-1}.

Two uncoated α-Al_2O_3 45 pores per linear inch (ppi) monoliths were placed at the front and back face of the catalyst as heat shields and friction fit in the reactor tube using 1 mm thick ceramic insulation. Temperatures at the catalyst front and back face, and throughout the system, were measured using type-K thermocouples and monitored with LabView. The entire apparatus was wrapped in 2.5 cm thick ceramic fiber insulation to minimize heat loss (typically $\leq$ 15 %). Reactor effluent was immediately and completely incinerated.

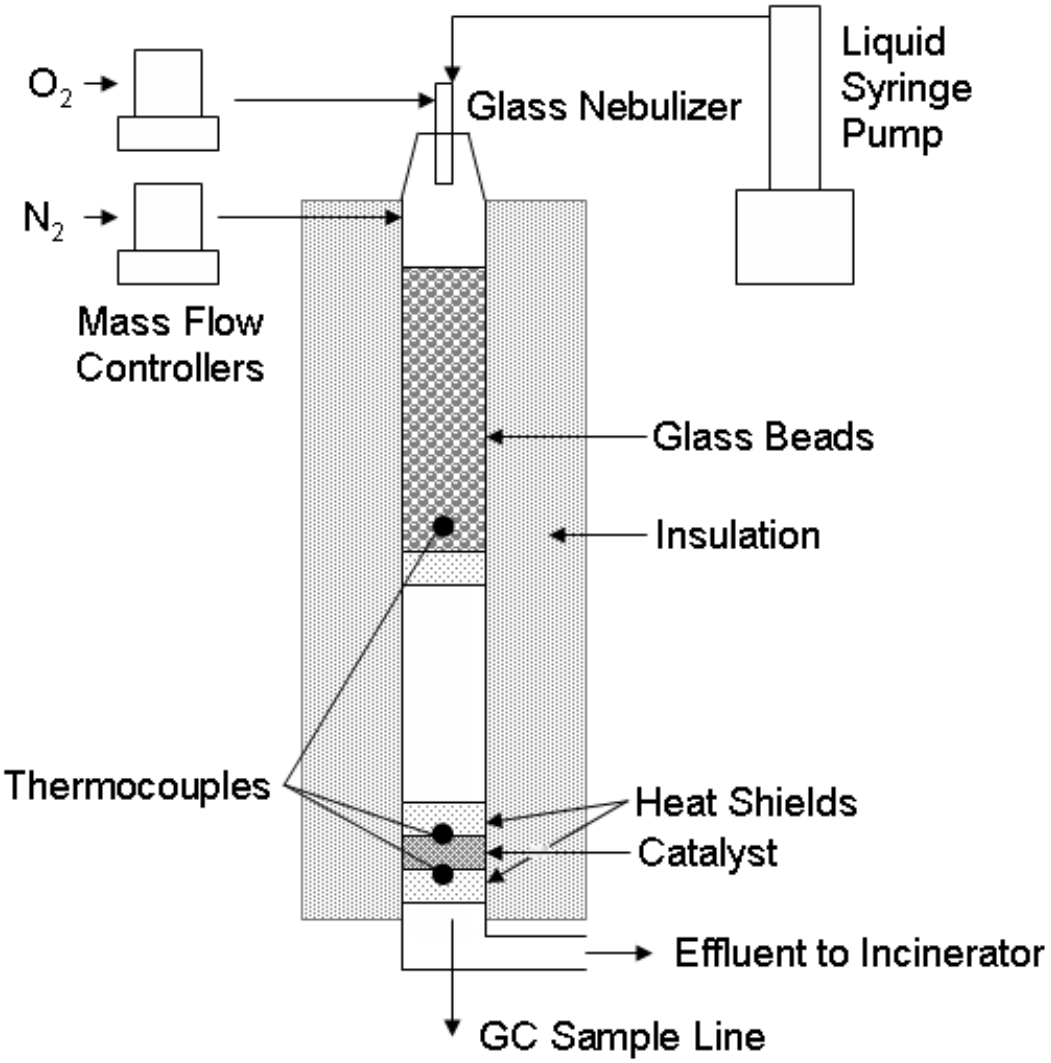

Figure 3.1: Schematic of apparatus used for monoaromatic experiments.

3.2.1 Catalyst Preparation

All catalysts were deposited on 1.6 cm diameter, 1 cm long cylindrical 45 ppi α-Al_2O_3 monoliths. 2.5 wt% Rh was applied to a blank monolith as aqueous $Rh(NO_3)_3$ using the incipient wetness technique, dried, then calcined for 6 hours at 600 °C.[43] Rh-Ce catalysts (2.5 wt% each) were prepared by the same method, with Ce deposited as $Ce(NO_3)_3{\cdot}6H_2O$. For washcoated catalysts, 5 wt% washcoat was applied by aqueous slurry of γ-Al_2O_3 powder then calcined before application of desired metal. 2.5 wt% Pt was loaded as aqueous H_2PtCl_6, dried, then reduced under H_2 and N_2 at 500 °C for 6 hours. All Rh-based catalysts were run for $\geq$ 60 hours without noticeable deactivation.

3.2.2 Reactor Startup and Operation

The apparatus was first externally heated under nitrogen flow sufficiently above the boiling point of the liquid feed. The desired flow conditions were chosen based on the feed C/O ratio, defined as the ratio of the inlet carbon atoms to the inlet oxygen atoms. C/O ratios between 1.0 (fuel lean) and 3.0 (fuel rich), in increments of 0.2, were tested for each feed and catalyst combination. The total inlet flow was held constant at 4 SLPM with N_2 and O_2 at air stoichiometry. C/O = 1.6 was chosen for reactor startup to be outside the combustion zone and to prevent coke formation.

Once the reactor was heated and the desired feed ratio was flowing, an isolated portion of the catalyst was heated externally to ~ 250 °C with a butane torch to begin autothermal catalytic reaction of the feed. The heat and reaction then propagated throughout the catalyst bed, noted by a dramatic increase in catalyst temperature. After reactor startup, the system was allowed to reach steady state for 30 minutes before data acquisition.

Reactor shutdown was initiated by turning off the oxygen, followed by the liquid feed. Nitrogen was flowed at 2 SLPM until the entire system cooled below 150 °C.

3.2.3 Data Acquisition and Analysis

Products were sampled directly below the catalyst bed through a quartz capillary to a stainless steel line heated to 200 ± 5 °C, preventing effluent condensation. The residence time in the sample line was varied to confirm there was negligible downstream chemistry during sampling.

An HP 6890 Gas Chromatograph equipped with autosampling, a 30 m, 320 μm ID HP-Plot Q capillary column, and a thermal conductivity detector was used to identify and quantify permanent gases, C_2 hydrocarbons, and unreacted monoaromatics.

Three effluent samples (generally $\leq$ 5 % carbon error each) were analyzed and averaged for each data point. Product selectivities were measured and defined as the ratio of atoms in the product species to the atoms in the converted aromatic feed. Unidentified effluent species were grouped according to number of carbon atoms (verified by a separate HP 5890 Gas Chromatograph Mass Spectrometer with the same column) and used to estimate carbon error. To ensure data reproducibility and negligible catalyst deactivation, C/O ratios were repeated periodically and duplicate catalysts were tested.

3.3 Results

Each of the five monoaromatic feeds were tested on each of the five noble metal-based catalysts. Benzene, toluene, ethylbenzene, and cumene were run stably on all Rh-based catalysts with no observable coke formation. Experiments on Pt catalysts were unsuccessful due to coking and will not be included in references to "all data/experiments" hereafter. Styrene was run without severe coke formation on Rh-Ce/γ-Al_2O_3 only.

3.3.1 Catalyst Temperatures

Catalyst back face temperatures were consistently hotter than the front face and both temperatures decreased as C/O ratio increased for all experiments (Fig. 3.2). All feeds produced similar catalyst temperatures, although benzene and toluene typically had higher temperatures than ethylbenzene and cumene ($\sim$ 50 - 100 °C). The Rh catalyst had the smallest axial temperature gradient, as well as the lowest back face temperatures. Generally, catalyst back face temperatures increased and front face temperatures decreased in the order of Rh/γ-Al_2O_3, Rh-Ce, and Rh-Ce/γ-Al_2O_3.

3.3.2 Conversion

Conversion of each feed decreased as C/O ratio increased (Fig. 3.3). Benzene and toluene behaved very similarly on all catalysts with the lowest conversions of all fuels. Ethylbenzene and cumene had consistently higher conversion, reaching 100 % at low C/O ratios on some catalysts. Styrene conversions on Rh-Ce/γ-Al_2O_3 were similar to benzene and toluene. Conversion increased in the order of Rh < Rh/γ-Al_2O_3 < Rh-Ce < Rh-Ce/γ-Al_2O_3.

3.3.3 Hydrogen Selectivity

Benzene and toluene produced similar selectivity to hydrogen-containing products, as did ethylbenzene and cumene. For all experiments, hydrogen selectivity to H_2 (S_{H_2}) decreased with increasing C/O ratio (Fig. 3.4 and 3.5). As benzene and toluene generally produced only hydrogen and water, changes in S_{H_2} were met with equal and opposite changes in selectivity to water. Ethylbenzene and cumene had lower S_{H_2}, as a variety of hydrocarbons were observed in the effluent. Styrene converted on Rh-Ce/γ-Al_2O_3 had a large range of values for S_{H_2}, varying between $\sim$ 20 and 80 % over all C/O ratios.

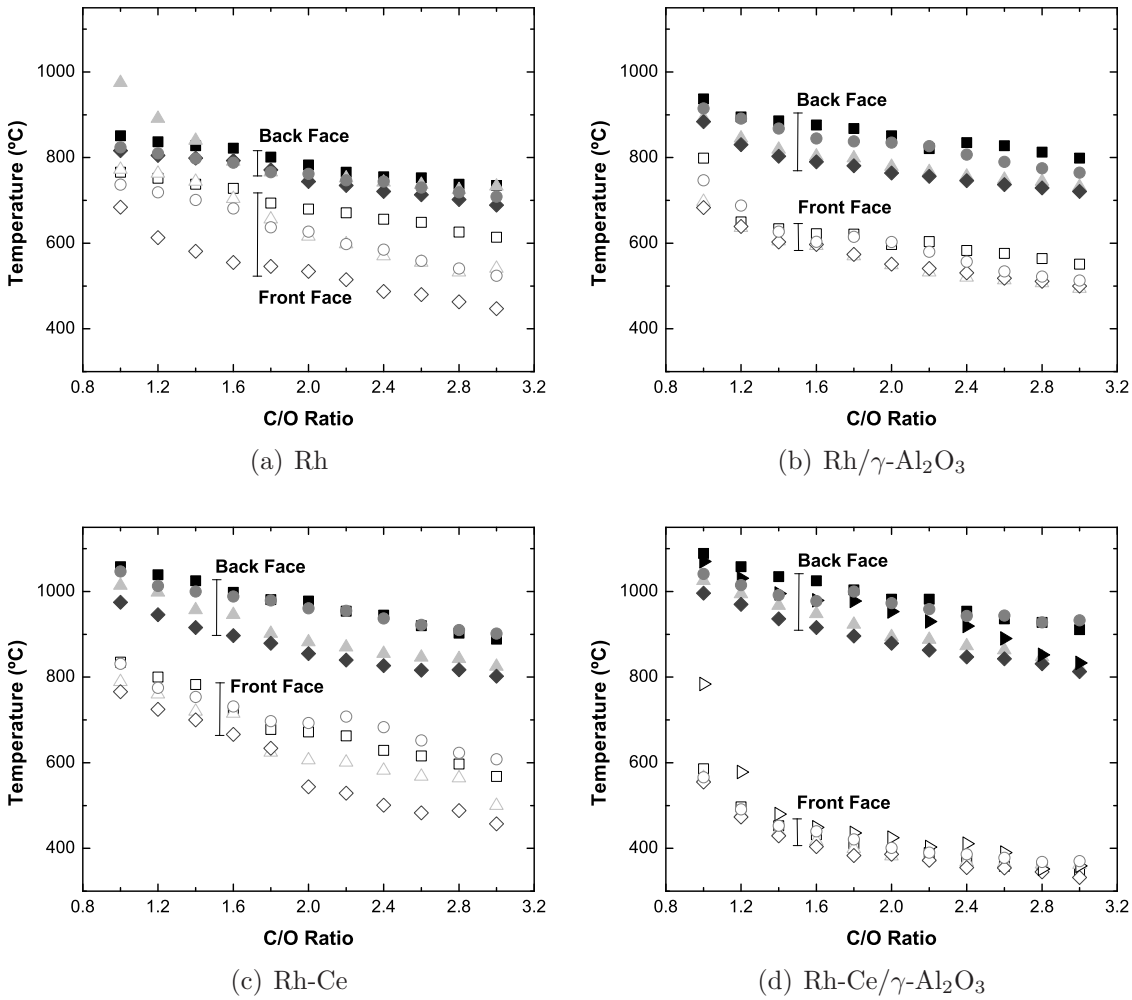

(a) Rh (b) Rh/γ-Al_2O_3

(c) Rh-Ce (d) Rh-Ce/γ-Al_2O_3

Figure 3.2: Front (open) and back (filled) face catalyst temperatures for ■ benzene, ● toluene, ▲ ethylbenzene, ♦ cumene, and ► styrene on (a) Rh, (b) Rh/γ-Al_2O_3, (c) Rh-Ce, and (d) Rh-Ce/γ-Al_2O_3.

S_{H_2} was lowest on the Rh catalyst, generally $\leq$ 20 % for all feeds, and highest on the Rh-Ce/γ-Al_2O_3 catalyst. Rh-Ce and Rh/γ-Al_2O_3 produced selectivities between these extremes, with Rh-Ce more selective to H_2 than Rh/γ-Al_2O_3 for benzene and toluene.

3.3.4 Carbon Selectivity

Carbon Oxides

Very similar carbon selectivities were observed for benzene and toluene as well as ethylbenzene and cumene. For all experiments, S_{CO} was always higher than S_{CO_2}.

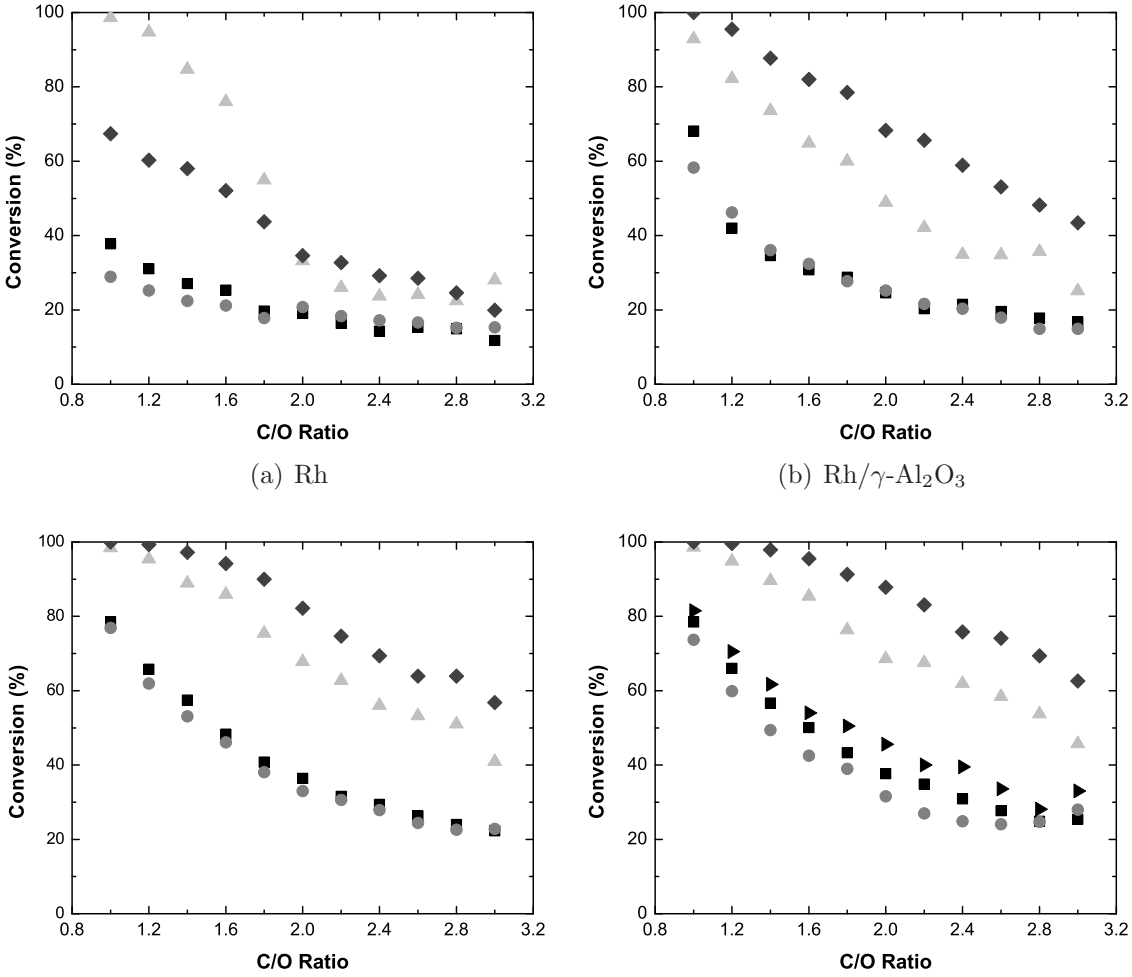

(a) Rh (b) Rh/γ-Al_2O_3

(c) Rh-Ce (d) Rh-Ce/γ-Al_2O_3

Figure 3.3: Percent fuel conversion of ■ benzene, ● toluene, ▲ ethylbenzene, ♦ cumene, and ► styrene on (a) Rh, (b) Rh/γ-Al_2O_3, (c) Rh-Ce, and (d) Rh-Ce/γ-Al_2O_3.

Benzene exhibited the highest S_{CO} (Fig. 3.6) and generally only produced carbon oxides. Toluene behaved similarly to benzene, though with a slightly smaller difference between S_{CO} on each catalyst. S_{CO} were similar for cumene and ethylbenzene. Styrene on Rh-Ce/γ-Al_2O_3 exhibited much higher S_{CO} than ethylbenzene or cumene.

Rh-Ce/γ-Al_2O_3 gave the highest S_{CO} for all feeds. Rh-Ce had the next highest S_{CO}, though performed similar to Rh-Ce/γ-Al_2O_3 below C/O of 1.6 for benzene and toluene. Rh had the lowest S_{CO}, while Rh/γ-Al_2O_3 performed between Rh and Rh-Ce.

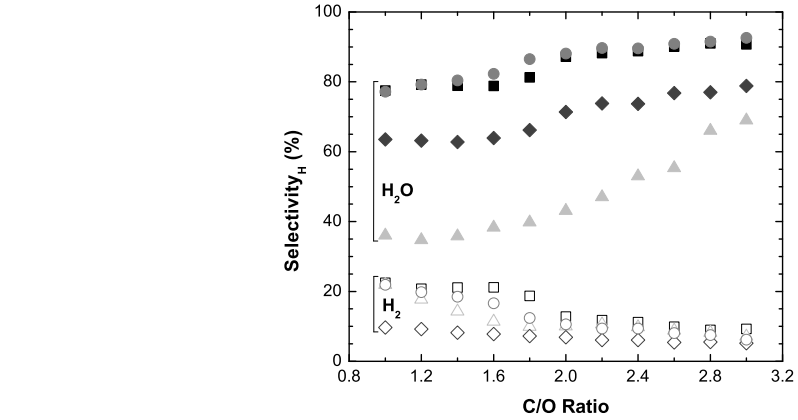

(a) Rh

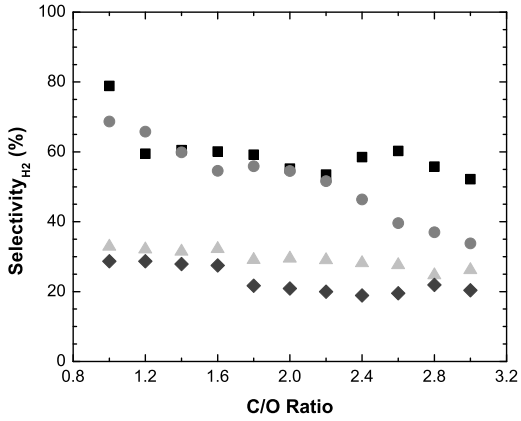

(b) Rh/γ-Al_2O_3, H_2 Selectivity

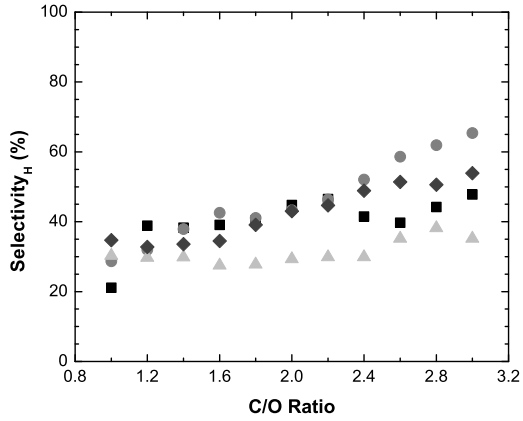

(c) Rh/γ-Al_2O_3, H_2O Selectivity

Figure 3.4: Hydrogen selectivity to H_2 and H_2O of ■ benzene, ● toluene, ▲ ethylbenzene, ♦ cumene, and ► styrene on (a) Rh, and (b), (c) Rh/γ-Al_2O_3.

Hydrocarbons

Benzene on Rh/γ-Al_2O_3 produced trace amounts ($\ll$ 1 %) of methane, ethylene, and acetylene between C/O of 1.2 and 1.8. Only syngas and combustion products were observed for all other benzene experiments. Methane ($<$ 1 %) and benzene (1 - 2 %) were also observed in the toluene effluent for all experimental conditions.

Styrene was consistently the most abundant hydrocarbon product for both ethylbenzene and cumene (Fig. 3.7). For cumene, benzene, methane, and ethylene were the next three most abundant hydrocarbon products with selectivities $\leq$ 11, 5, and 6 %, respectively. All other species exhibited selectivities less than 2.5 %. For ethylbenzene, benzene, toluene, and ethylene were the next three most abundant hydrocarbon products with selectivities $\leq$ 14, 11, and 7 %, respectively. All other species were observed at trace amounts except for methane, which never exceeded a selectivity of

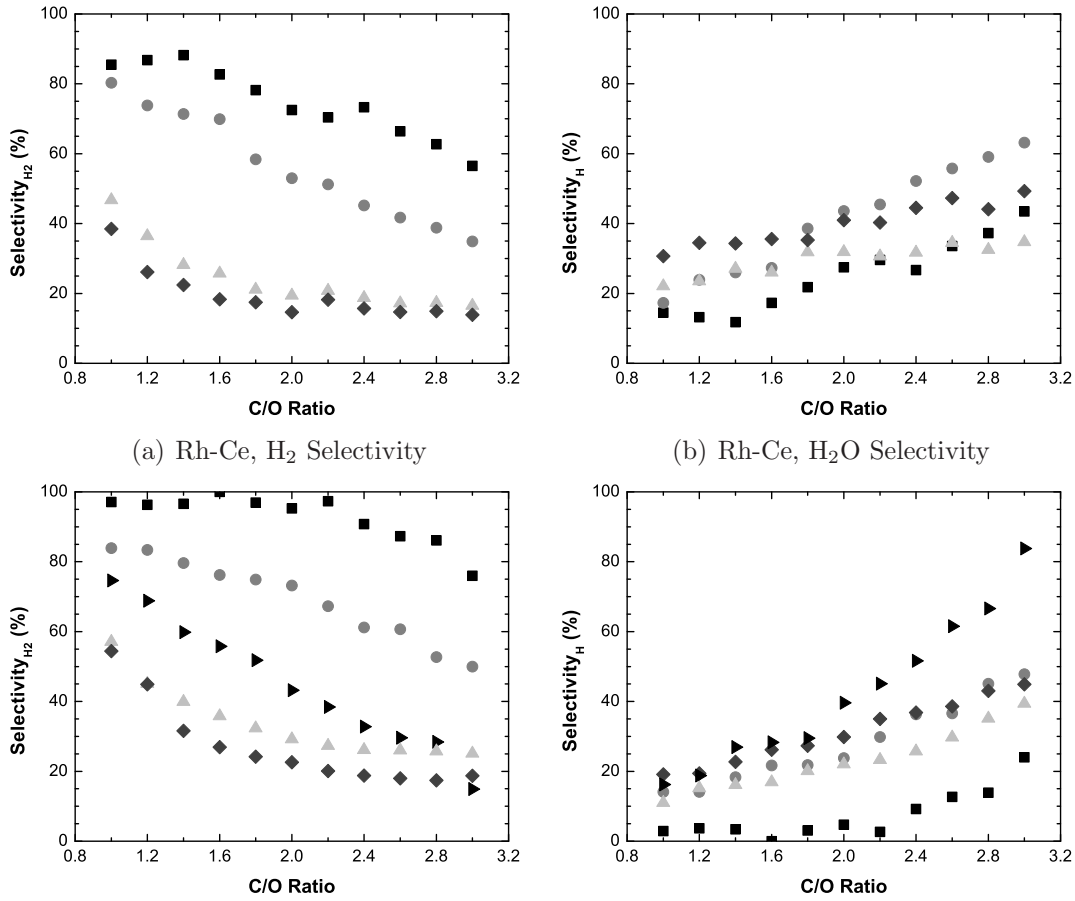

(a) Rh-Ce, H_2 Selectivity

(b) Rh-Ce, H_2O Selectivity

(c) Rh-Ce/γ-Al_2O_3, H_2 Selectivity

(d) Rh-Ce/γ-Al_2O_3, H_2O Selectivity

Figure 3.5: Hydrogen selectivity to H_2 and H_2O of ■ benzene, ● toluene, ▲ ethylbenzene, ♦ cumene, and ► styrene on (a), (b) Rh-Ce, and (c), (d) Rh-Ce/γ-Al_2O_3.

2.7 %.

Styrene exhibited a low selectivity to hydrocarbons on Rh-Ce/γ-Al_2O_3. Carbon selectivity was highest to benzene and ethylene, $\leq$ 10 and 5 %, respectively. Methane, acetylene, toluene, and ethylbenzene were also observed, but never exceeded a selectivity of 2.2%.

3.4 Discussion

3.4.1 Monoaromatics

Benzene and Toluene

Benzene appears to react primarily at the catalyst surface with little homogeneous gas-phase reaction. Benzene adsorbs by π-bonding parallel to the Rh surface, typically

over a three-fold hollow site with very limited molecular desorption.[79–83] Decomposition begins by C-C bond cleavage and surface carbon species can react with adsorbed oxygen.[80,82,83] The presence of hydrocarbon surface species facilitates carbon movement on the metal surface for further reaction, limiting coke formation.[82] CO, CO_2, H_2, and H_2O are produced primarily through heterogeneous catalytic reactions.

The large bond dissociation energies and high resonance stability associated with an aromatic ring limit homogeneous reactions.[74] This stability requires higher temperatures and longer residence times to homogeneously react benzene than those present in the experimental system.[74,76] However, temperatures throughout the catalyst were sufficient to initiate benzene oxidation for all C/O ranges. Therefore only trace amounts of benzene reacted homogeneously to produce methane, ethylene, and acetylene.[75,76]

Toluene has been shown previously to behave similar to benzene on metal catalytic surfaces, in agreement with the presented experimental results.[81–84] For all catalysts and feed ratios, benzene and toluene had nearly identical conversions and selectivities. Carbon selectivity to methane and benzene from toluene were 1 - 2 % for all C/O ratios, likely produced from homogeneous reactions, as routes to products $> C_1$ on Rh from toluene are unknown at the presented experimental conditions.[80,81]

Ethylbenzene and Cumene

Addition of a functional group to an aromatic ring can increase homogeneous and heterogeneous reactivity.[85,86] The larger alkyl groups and the weak secondary and tertiary C-H bonds of ethylbenzene and cumene can participate in homogeneous reactions and also adsorb more favorably onto the catalyst surface than benzene. Homogeneous reactions of these alkyl groups produce the wide range of hydrocarbons observed in the effluent during experiments.[87]

Ethylbenzene and cumene had similar conversion trends on all catalysts (Fig. 3.3), excluding low C/O ratios on Rh. Both fuels consistently had higher conversion than benzene or toluene due to higher homogeneous reactivity. High styrene selectivity (Fig. 3.7) may indicate homogeneous dehydrogenation of ethylbenzene for all experiments. Benzene and ethylene may have been produced by homogeneous cleavage of the alkyl group from the aromatic ring. Toluene and methane were also observed as gas phase products. Of the converted fuel, at least one third survived as an aromatic ring.

Cumene generally had higher conversion than ethylbenzene due to the increased homogeneous reactivity of the larger alkyl group. Again, styrene was the major

homogeneous product, resulting from the cleavage of one carbon from the isopropyl group. Benzene and ethylene were also observed in equal molar amounts in the effluent of cumene experiments, possibly as a result of further homogeneous reaction of styrene.

Styrene

On Rh-Ce/γ-Al_2O_3, styrene exhibited conversion similar to that of toluene and benzene across all C/O ratios, much lower than ethylbenzene or cumene (Fig. 3.3). Hydrogen and carbon oxide species were the main products, resulting primarily from catalytic reactions. The only hydrocarbon selectivities larger than ~ 2 % were those to benzene and ethylene, resulting from the homogeneous cleaving of the ethenyl group from the aromatic ring. The high selectivity to styrene of both ethylbenzene and cumene in combination with styrene's lower conversion may indicate a higher gas phase stability, resulting from the higher bond energy associated with the carbon double bond of the ethenyl group.

3.4.2 Catalysts

Platinum

Data were not collected on Pt catalysts due to severe coking and catalyst deactivation during operation. Benzene and other aromatics adsorb on Pt in the same manner as on Rh.[79,88] However, C-H bonds are the first to break on Pt, rather than the C-C bonds.[82,88,89] The formation of strong C-C networks and the lack of mobile C-H surface species contribute to the formation of unreactive coke, which deactivates the catalyst.

Pt was successfully lit off, but deactivated within 90 s of startup. Deactivation likely began at the front face (as indicated by an initial front face temperature drop) where cooler temperatures facilitated solid carbon formation. Catalyst coking propagated rapidly through the catalyst, quenching the reaction. Similar results were observed previously.[38]

Rhodium

The rhodium catalyst reformed all monoaromatics autothermally, excluding styrene, to a mixture of syngas and hydrocarbons.

Generally, benzene and toluene were observed to have higher front and back face temperatures than the higher alkylated aromatics (excluding styrene on Rh-Ce/γ-Al_2O_3). Reforming reactions with steam generated in the catalyst bed and endothermic homogeneous cracking of ethylbenzene, cumene, and their gas phase products may have resulted in lower temperatures throughout the catalyst (Fig. 3.2). The higher gas phase stability of benzene, toluene, and styrene limited endothermic reactions, maintaining high catalyst temperatures.

Rh generally exhibited high S_{CO}, especially for benzene and toluene (Fig. 3.6). Ethylbenzene and cumene exhibited lower S_{CO} due to their high gas phase reactivity to hydrocarbons. S_{CO_2} was very similar for all feeds and much lower than S_{CO}. As discussed earlier, the majority of carbon oxide products are believed to be produced on the catalyst surface. High temperatures observed at low C/O ratios reduce species' surface residence time on the catalyst, resulting in higher fuel conversion and higher selectivity to CO, as CO will more likely desorb on Rh than react with an additional surface oxygen.[82] As C/O ratio increases, the system becomes more fuel rich, decreasing temperatures and lengthening the surface residence time, producing more CO_2 and less CO.

Similar to S_{CO}, S_{H_2} on Rh was highest for benzene and toluene (Fig. 3.4). However, S_{H_2O} was consistently higher than S_{H_2} for all feeds, possibly due to reactions of O_2 with desorbed H_2 throughout the catalyst bed. Ethylbenzene and cumene had lower S_{H_2} and S_{H_2O} than benzene and toluene due to their high selectivity to hydrocarbons.

Rh/γ-Al_2O_3

The addition of a γ-Al_2O_3 washcoat to Rh catalysts has been shown to increase catalytic sites and maintain catalytic performance at high temperatures by preventing metal sintering.[42,43,90] Compared to the Rh catalyst, the addition of a washcoat increased benzene and toluene back face temperatures by $\sim$ 60 - 80 °C and conversions by $\sim$ 10 % at all C/O ratios (Fig. 3.2 and 3.3). Despite an increase in conversion for ethylbenzene and cumene as well, the back face temperature of Rh/γ-Al_2O_3 was very similar to Rh. This may be due to higher rates of endothermic homogeneous cracking balancing the increase in exothermic catalytic conversion.

Washcoat addition generally decreased the catalyst front face temperature. This change, though only $\sim$ 20 °C, may be caused by an increase in reforming at the front face. Rh has been shown to be a very active steam reforming catalyst, and the addition of washcoat increases reforming activity by increasing the number of catalyst sites.[91] The increase in catalytic activity also increased the selectivity to

syngas products for all feeds. A dramatic increase in S_{H_2} was observed, especially for benzene and toluene, which was matched by an equal drop in S_{H_2O} (Fig. 3.4).

Rh-Ce

Cerium addition to a Rh catalyst has been shown to stabilize the Rh metal, increase catalyst selectivities to syngas, and prevent coke formation by increasing oxidation rates at the surface.[40–42,90,92,93] For all fuels, addition of Ce gave the same, or slightly higher front face temperatures than the Rh catalyst. However, the back face temperatures increased dramatically, higher than either Rh or Rh/γ-Al_2O_3 by 100 - 200 °C(Fig. 3.2). Overall conversions for all fuels were also significantly higher at all C/O ratios.

For benzene and toluene, Ce addition increased selectivity to syngas and decreased S_{H_2O} and S_{CO_2} more than the addition of a washcoat (Fig. 3.4-3.6). However, the selectivity differences between Ce and washcoat addition were difficult to distinguish for ethylbenzene and cumene due to the high rates of homogeneous chemistry for both.

Rh-Ce/γ-Al_2O_3

The Rh-Ce/γ-Al_2O_3 catalyst was the only catalyst able to reform styrene for all C/O ratios without severe coke formation. This catalyst also experienced the largest temperature gradient of all catalysts. The front face temperature was significantly lower, below 400 °C at high C/O ratios (Fig. 3.2). As with Rh/γ-Al_2O_3, the lower temperatures may be explained by an increase in endothermic steam reforming activity at the front face, facilitated by washcoat addition.[78] The back face temperatures and conversions, higher than both Rh and Rh/γ-Al_2O_3, were very similar to those of the Rh-Ce catalyst. Addition of Ce to Rh appears to have a stronger effect on increasing exothermic surface oxidation reaction rates than does addition of washcoat.

For benzene and toluene, Rh-Ce/γ-Al_2O_3 had the highest selectivity to syngas and the lowest to H_2O and CO_2 of any catalyst (Fig. 3.4-3.6). The same was true for ethylbenzene and cumene, however the difference was considerably smaller. The combination of washcoat and Ce increased catalytic sites and activity to maximize syngas selectivity and minimize total oxidation products.

3.5 Conclusions

Benzene and toluene behave similarly on all catalysts and they generally react heterogeneously to produce syngas and combustion products. Toluene produces small amounts of benzene and methane, primarily from homogeneous reactions. Ethylbenzene and cumene also behave similarly, with high conversion and large amounts of hydrocarbon and aromatic products (mostly styrene) due to homogeneous reactivity of the alkyl group. Styrene conversion was similar to benzene and toluene possibly due to higher homogeneous stability than ethylbenzene and cumene. Styrene was only stably reformed on Rh-Ce/γ-Al_2O_3, mainly producing syngas and combustion products with small amounts of benzene and ethylene. Overall, the aromatic ring was very stable in the reactor.

Comparing catalyst performance, Pt coked severely and deactivated for each feed tested. Rh successfully converted monoaromatics, excluding styrene, autothermally on millisecond time scales. Back face temperatures were consistently higher than the front face due to heat produced from oxidation reactions throughout the catalyst. The addition of a γ-Al_2O_3 washcoat stabilized Rh catalyst sites, lowering the front face temperature because of an increase in endothermic steam reforming activity, and producing higher overall conversions and syngas selectivities. The addition of Ce more effectively increased conversion and syngas selectivity than washcoat for benzene and toluene. However, selectivity differences between Rh-Ce and Rh/γ-Al_2O_3 for ethylbenzene and cumene were unclear due to their high selectivities to homogeneous products. Fuel conversion and back face temperatures were very similar between Rh-Ce and Rh-Ce/γ-Al_2O_3. However, Rh-Ce/γ-Al_2O_3 produced the highest selectivities to syngas of any catalyst and was the only catalyst able to convert styrene.

Finally, product selectivities can be adjusted by changing the C/O ratio. Low C/O ratios (fuel lean) produced higher temperatures, conversions, and syngas selectivities. Higher C/O ratios resulted in lower conversions and temperatures and higher selectivities to hydrocarbon and combustion products.

Acknowledgments

This material is based upon work supported under a National Science Foundation Graduate Research Fellowship. This work was also partially supported by U.S. Department of Energy Grant DE-FG02-88ER13878.

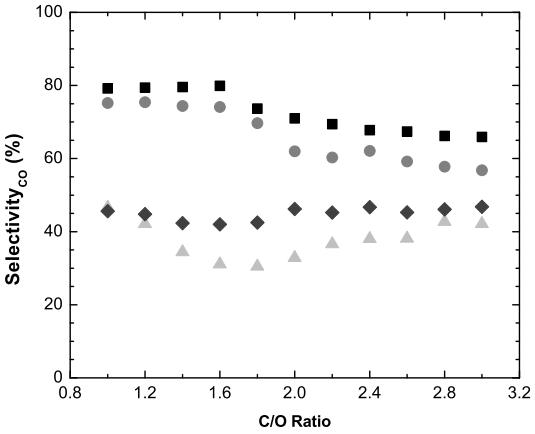

(a) Rh, CO Selectivity

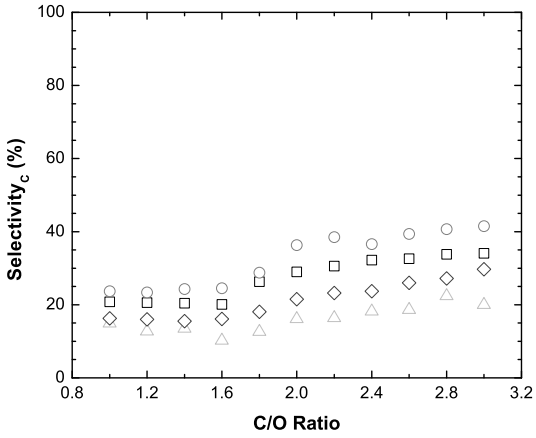

(b) Rh, CO_2 Selectivity

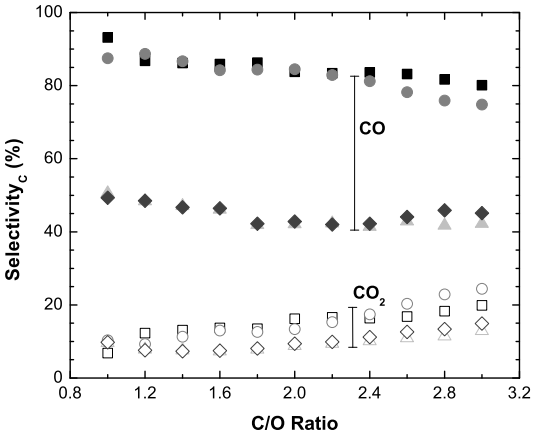

(c) Rh/γ-Al_2O_3

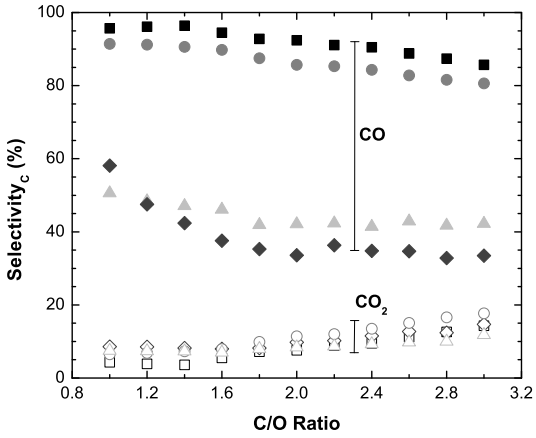

(d) Rh-Ce

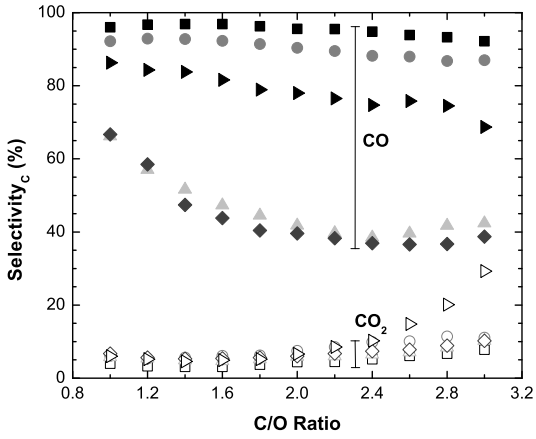

(e) Rh-Ce/γ-Al_2O_3

Figure 3.6: Carbon selectivity to CO (filled) and CO_2 (open) of ■ benzene, ● toluene, ▲ ethylbenzene, ♦ cumene, and ► styrene on (a), (b) Rh, (c) Rh/γ-Al_2O_3, (d) Rh-Ce, and (e) Rh-Ce/γ-Al_2O_3.

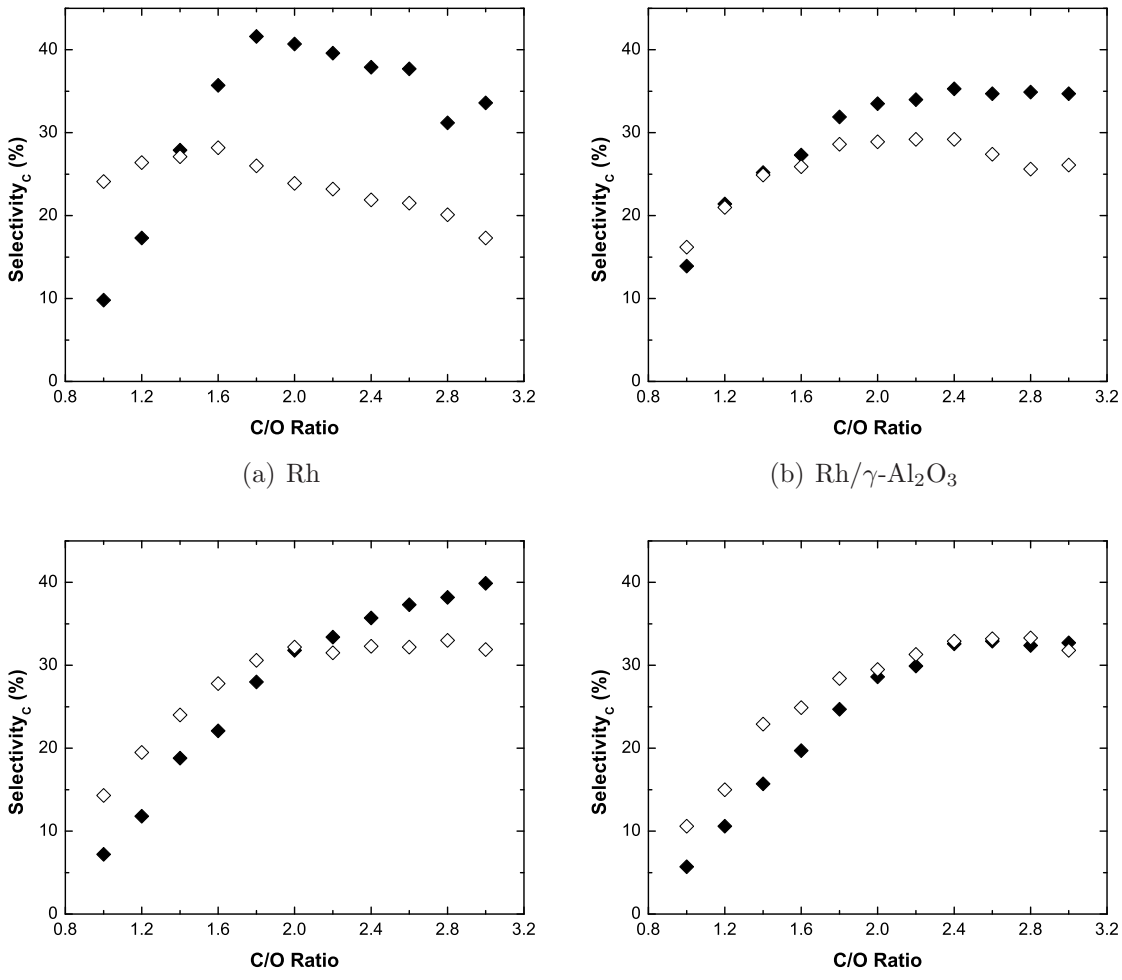

(a) Rh (b) Rh/γ-Al_2O_3

(c) Rh-Ce (d) Rh-Ce/γ-Al_2O_3

Figure 3.7: Carbon selectivity to styrene of ethylbenzene (filled) and cumene (open) on (a) Rh, (b) Rh/γ-Al_2O_3, (c) Rh-Ce, and (d) Rh-Ce/γ-Al_2O_3.

CHAPTER

FOUR

RAPID ABLATIVE PYROLYSIS OF CELLULOSE IN AN AUTOTHERMAL FIXED-BED CATALYTIC REACTOR[1]

Chapter 3 discussed the behavior of lignin surrogates during oxidative pyrolysis. Cellulose is another major component of lignocellulosic biomass and is easily obtained in a pure form. Here, a fixed bed Pt or Rh-Ce catalytic reactor has been shown to produce high carbon selectivity to pyrolysis oil from cellulosic feedstock. Heat was generated in situ by the sacrificial oxidation of pyrolysis vapors. High heat transfer rates within the catalyst bed allowed for 100 % conversion of the cellulose feed while maintaining char-free and autothermal operation. Variations in support geometry, catalyst, and H_2 addition were investigated to manipulate the yield of pyrolysis products. Carbon selectivity to pyrolysis products as high as 60 % was achieved with a Pt combustion catalyst.

4.1 Introduction

Many biological, chemical, and thermal pathways have been investigated as potentially efficient processing methods to utilize biomass as a renewable feedstock. Pyrolysis of biomass has been investigated as a process to produce gas and liquid products using fluidized bed, rotary kiln, and plate ablative reactors, among others.[94,95] However, many pyrolysis reactors are hindered by char production resulting from limited heat transfer rates to the reactor. As a result, reactors are difficult to scale up due

[1]Portions of this chapter appear in C.M. Balonek, J.L. Colby, N.E. Persson, L.D. Schmidt, "Rapid ablative pyrolysis of cellulose in an autothermal fixed-bed catalytic reactor," *ChemSusChem* **3** (2010) 1355-1358.

to the large heat inputs required to maintain operation, causing pyrolysis oil yields to suffer.

Heat transfer rates to feed particles should be sufficiently high to prohibit char formation within pyrolysis reactors. Previous research has demonstrated the volatilization of cellulose particles on the front face of a Rh-Ce/α-Al_2O_3 catalyst bed.[96] High speed photography was used to image 300 μm cellulose particles impacting the 700 °C catalyst, pyrolyzing to liquid intermediate compounds that were then volatilized and convected into the catalyst bed and further reacted to synthesis gas. High heat transfer rates to the particles (3.4 MW m^{-2}) resulted in the complete conversion of cellulose particles without char formation.

An ideal pyrolysis reactor should operate continuously, efficiently, and char-free to maximize pyrolysis oil yield. Graham et al. demonstrated an ultra-fast pyrolysis process that converted cellulose to more than 80 wt% gases at temperatures between 750 and 900 °C on millisecond timescales.[97] Wei et al. examined the fast pyrolysis of different biomass feedstocks using a free-fall reactor with a residence time < 2 s.[98] Particles (300 - 450 μm) pyrolyzed at 700 - 800 °C yielded up to 80 wt% gases and 20 wt% char. Similar to these pyrolysis processes, the reactor presented here operates at millisecond residence times and high temperatures (700 - 900 °C); however, it is able to select for larger hydrocarbon liquid products, rather than gas products. A fraction of the cellulose pyrolysis vapors (10 - 40 %, Table 4.1) are sacrificially oxidized to CO_2 and H_2O to provide heat to the front face for pyrolysis allowing for autothermal and char-free operation.

4.2 Experimental Details

Reactions were carried out in a quartz reactor tube (19 mm ID) over a fixed catalyst bed (1 cm) represented in Figure 4.1. Two types of supports were used: a cylindrical monolith (16 mm diameter, 10 mm long, 65 ppi α-Al_2O_3, 5 wt% γ-Al_2O_3 washcoat) and spheres (1 cm bed, 1.3 mm diameter α-Al_2O_3). Metals were impregnated onto the supports using the incipient wetness technique, described previously.[99] Rh-Ce catalysts contained 2.5 wt% of each metal, Pt was applied to the support at 2.5 wt%. Mass flow controllers fed N_2, O_2, CH_4, and H_2 to the reactor. 0.1 SLPM methane was added to the feed during every experiment to suppress feed ignition before reaching the catalyst.[100] An auger/hopper system (Schenck AccuRate) fed microcrystalline cellulose (300 μm) to the reactor. Heavy pyrolysis vapor products were condensed out, while permanent and light gases were identified and quantified using a gas chro-

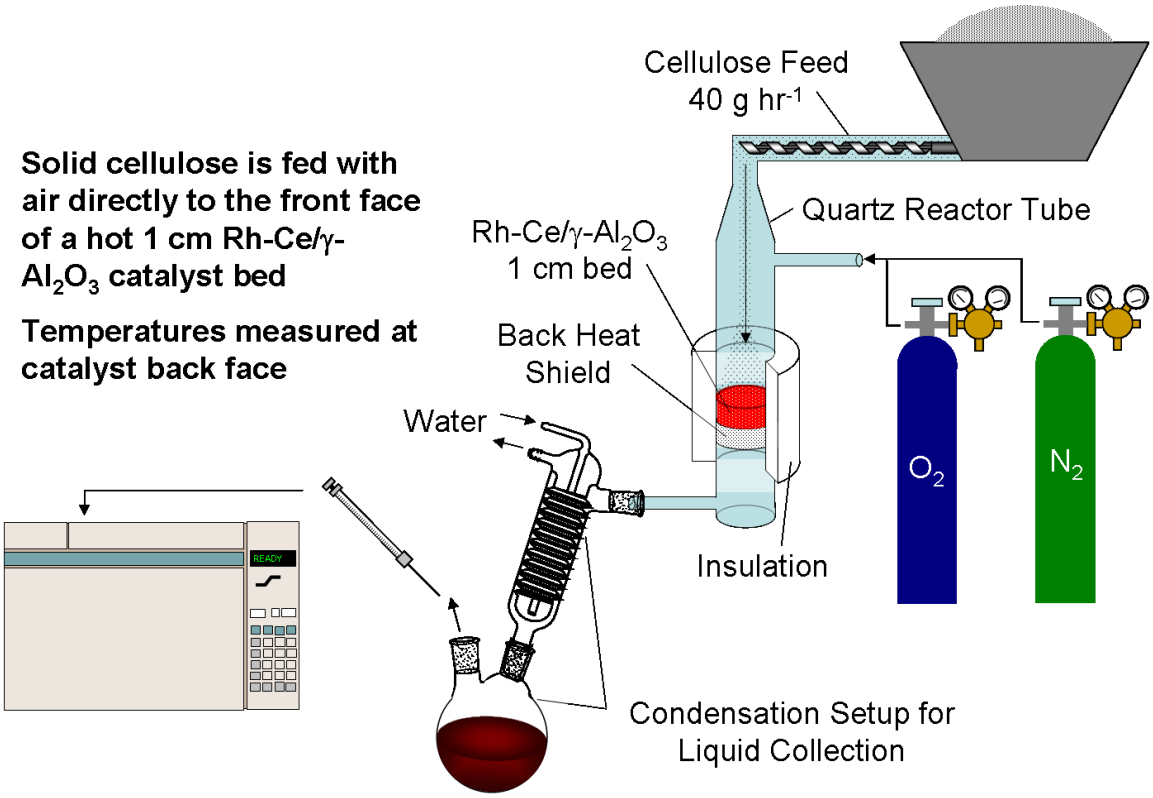

Figure 4.1: Experimental schematic for the production of pyrolysis oils from cellulose feedstock.

matograph (HP 6890). All carbon-containing products not quantified as CO_2, CO, or CH_4 are classified as 'pyrolysis products'. For all experiments, cellulose was completely pyrolyzed at the front face of the catalyst to give 100 % conversion of the solid feed. Each catalyst operated for $\sim$ 30 hours with negligible coke formation.

Calculations were performed to determine pyrolysis oil yields in an idealized reactor (Fig. 4.2, dashed line). Assuming autothermal and adiabatic reactor operation, all non-pyrolysis products would be CO_2 and H_2O, as combustion will maximize energy available while minimizing fuel sacrificed to produce that energy. As a result, all O_2 is assumed to react with cellulose pyrolysis vapors according to: $C_6H_{10}O_5 + 6O_2 \rightarrow 6CO_2 + 5H_2O$. The remaining cellulose pyrolysis products are plotted in terms of carbon selectivity (S_{PP}) against the C/O ratio, which is the ratio of carbon atoms in the solid feed to the atoms of oxygen in the O_2 feed (Fig. 4.2, dashed line). All carbon not quantified as CO_2 is classified as a pyrolysis product (PP). Calculations were also performed to determine the effect of using a sacrificial combustion fuel to reduce the need for cellulose combustion (Fig. 4.3, dashed lines). A supplemental H_2 feed was assumed to completely combust with O_2 ($H_2 + 0.5O_2 \rightarrow H_2O$), leaving the

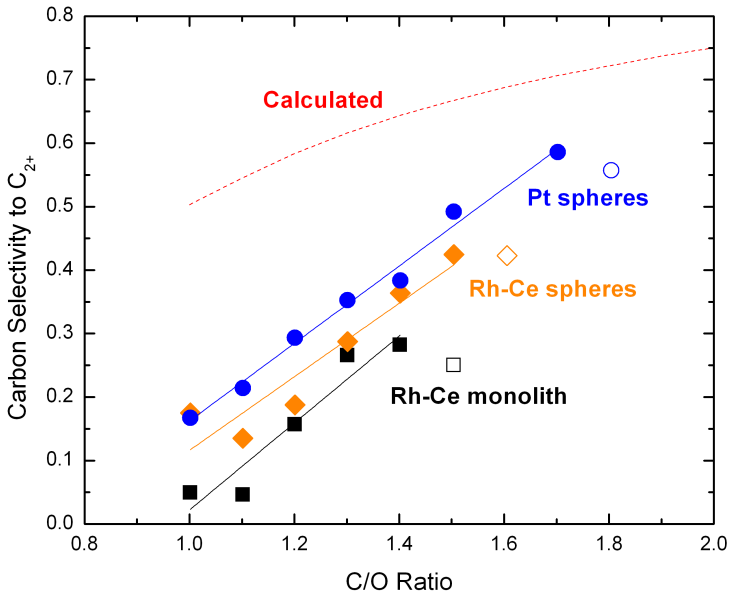

Figure 4.2: Carbon selectivity to pyrolysis products vs. C/O ratio. 60 g hr^{-1} cellulose feed rate; N_2 and O_2 feed air stoichiometry and rate to achieve desired C/O ratio with 0.1 SLPM CH_4; solid points indicate experimental data obtained at autothermal, steady operation with no accumulation of cellulose on the catalyst front face; open points indicate the conditions at which cellulose began to accumulate on the front face, affecting reactor operation; dashed line represents yield calculated at idealized reactor conditions.

remaining O_2 to combust with cellulose. Addition of 0.4 SLPM H_2 is calculated to increase S_{PP} from 50 % to 72 % at C/O = 1.0 (Table 4.1, italics).

4.3 Results and Discussion

It is favorable to limit the O_2 available for combustion to produce just enough heat required for pyrolysis of cellulose at the catalyst front face. This minimizes the fuel sacrificed for heat and increases the yield of pyrolysis products. Figure 4.2 demonstrates the effects of the C/O ratio, catalyst support, and catalyst metal on the carbon selectivity to pyrolysis oils. For all experiments, S_{PP} increases with C/O ratio. However, as the amount of combustion decreases at higher C/O ratios, the catalyst eventually cools to a critical temperature at which cellulose accumulates at the front face and autothermal operation of the reactor cannot be maintained. These points are represented in Figure 4.2 as open symbols and occur at catalyst back face

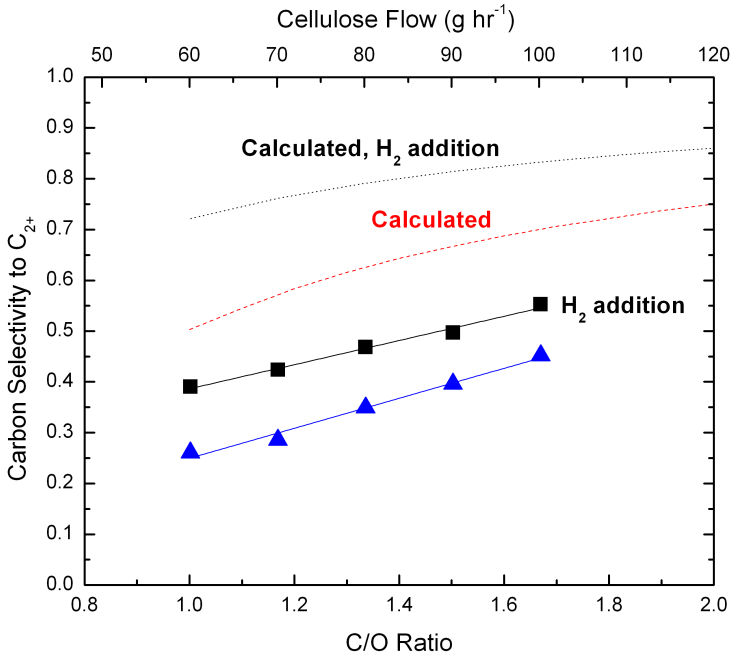

Figure 4.3: Carbon selectivity to pyrolysis products vs. C/O ratio on 2.5 wt% Pt/α-Al_2O_3 spheres. N_2, O_2, and CH_4 feed rates were held constant at 2.5, 0.452, and 0.1 SLPM; cellulose flow rate was varied (top x axis) to achieve the desired C/O ratio; 0.4 SLPM H_2 was added to the feed as indicated; solid points indicate experimental data obtained at autothermal, steady operation with no accumulation of cellulose on the catalyst front face; dashed line represents yield calculated at idealized reactor conditions.

Table 4.1: Selected experimental data for the autothermal oxidative pyrolysis of cellulose over Rh based fixed bed catalysts.

Experiment[a]	1	2	3	4	5	6	7	8	9	10	11	12	13	14
Catalyst	Rh-Ce/ γ-Al_2O_3	Rh-Ce/ γ-Al_2O_3	Rh-Ce/ γ-Al_2O_3	Rh-Ce/ γ-Al_2O_3	Rh-Ce	Rh-Ce	Pt	Pt	Pt	Pt				
Support	monolith	monolith	monolith	monolith	sphere	sphere	sphere	sphere	sphere	sphere				
Cellulose (g hr^{-1})	60	100	60	100	60	100	60	60	60	100	60	60	60	200
C/O	1.0	1.7	1.0	1.7	1.0	1.7	1.0	1.7	1.0	1.7	1.0	3.0	1.0	3.0
Gas Feed (SLPM)[b]														
N_2	2.500	2.500	2.500	2.500	2.500	2.500	1.700	1.000	2.500	2.500	1.700	1.000	2.500	2.500
O_2	0.452	0.452	0.452	0.452	0.452	0.452	0.452	0.266	0.452	0.452	0.452	0.266	0.452	0.452
H_2	0.0	0.0	0.4	0.4	0.0	0.0	0.0	0.0	0.4	0.4	0.0	0.0	0.4	0.4
$S_{H \rightarrow H2}$ (%)[c]	30	30	40	28	38	33	31	5	26	14	0.0	0.0	0.0	0.0
C Sel. (%)[d]														
CO	46	45	50	40	41	33	44	19	41	29	0.0	0.0	0.0	0.0
CO_2	35	26	17	33	25	38	18	18	12	50	17	28	8	
CH_4	1	3	2	3	1	2	0.8	5	3	4	0.0	0.0	0.0	0.0
PP[e]	18	26	21	41	25	39	17	59	39	55	50	83	72	92
Temp. (°C)[f]	960	770	850	710	870	702	851	661	807	772	1440	708	1353	701

[a] Data in italics are calculated values.
[b] All gas feeds include 0.1 SLPM methane.
[c] H Selectivity to H_2.
[d] C Selectivity to indicated species
[e] All carbons not accounted for in CO, CO_2, or CH_4 are considered pyrolysis products (PP).
[f] Temperatures measured at the back face of the catalyst bed using a type-K thermocouple.

temperatures of 650 - 700 °C. It is also important to note the discrepancy between the calculated S_{PP} and that measured during laboratory experiments. The amount of heat available for pyrolysis, and thus yields of desired products, was limited by lab-scale system heat losses, endothermic partial oxidation of cellulose (H_2 and CO products observed, Table 4.1), and endothermic reforming of pyrolysis vapors, as well as other reactions. This is expected as Rh is widely regarded as an excellent partial oxidation catalyst with high reforming activity.[101]

Support geometry also plays an important role in pyrolysis oil yield. The fixed bed of spheres consistently gave higher yields of desired products than the monolithic catalyst bed. SEM micrographs of used catalysts show differences in Rh-Ce particle size on the support surface (Fig. 4.4). Metal particles on alumina spheres are generally spherical and ~ 50 nm (Fig. 4.4(c)). In contrast, Rh-Ce accumulates over the γ-Al_2O_3 washcoat on the monolith support as much larger and less uniform particles (Fig. 4.4(a) and (b). Previous work has also demonstrated that spherical γ-Al_2O_3 supports yield much higher metal dispersion, and therefore higher catalyst activity, than the monolithic support, where metals form films and/or much larger particles.[42,102] This suggests that the more active sphere catalysts would yield less pyrolysis oil than monoliths: opposite what was observed. Michael et al. found that increased catalytic activity did not affect the length of the oxidation zone within a catalytic monolith, indicating that the system is mass transfer limited, which has also been discussed by Horn et al.[101,103] Higher mass transfer rates can allow complete oxygen consumption early in the catalyst bed, yielding high front face temperatures and abundance of heat for pyrolysis. Michael's experiments show that oxygen is consumed within 2 mm of an 80 ppi, 5 wt% Rh monolithic catalyst. These results can be compared to those of Panuccio et al., who show that oxygen is consumed within 1.3 mm of a 5 wt% Rh sphere bed at the same C/O ratio, indicative of higher mass transfer rates within the catalytic sphere bed.[104] Hohn et al. discuss the differences in heat transfer between monolithic and sphere bed catalysts that may account for differences in performance.[105] Spheres had consistently high front face temperatures due to higher conductive heat transfer rates as compared to monoliths, where convective heat transfer was more influential. Applied to the present system, higher rates of mass and conductive heat transfer with the sphere bed may account for the higher yields of pyrolysis oil and steady operation at higher C/O ratios than with the monolith by raising O_2 consumption rates and front face temperatures.

Platinum-coated spheres were observed to give higher selectivity to pyrolysis products and were able to operate at higher C/O ratios than Rh-Ce catalysts. Rh-Ce

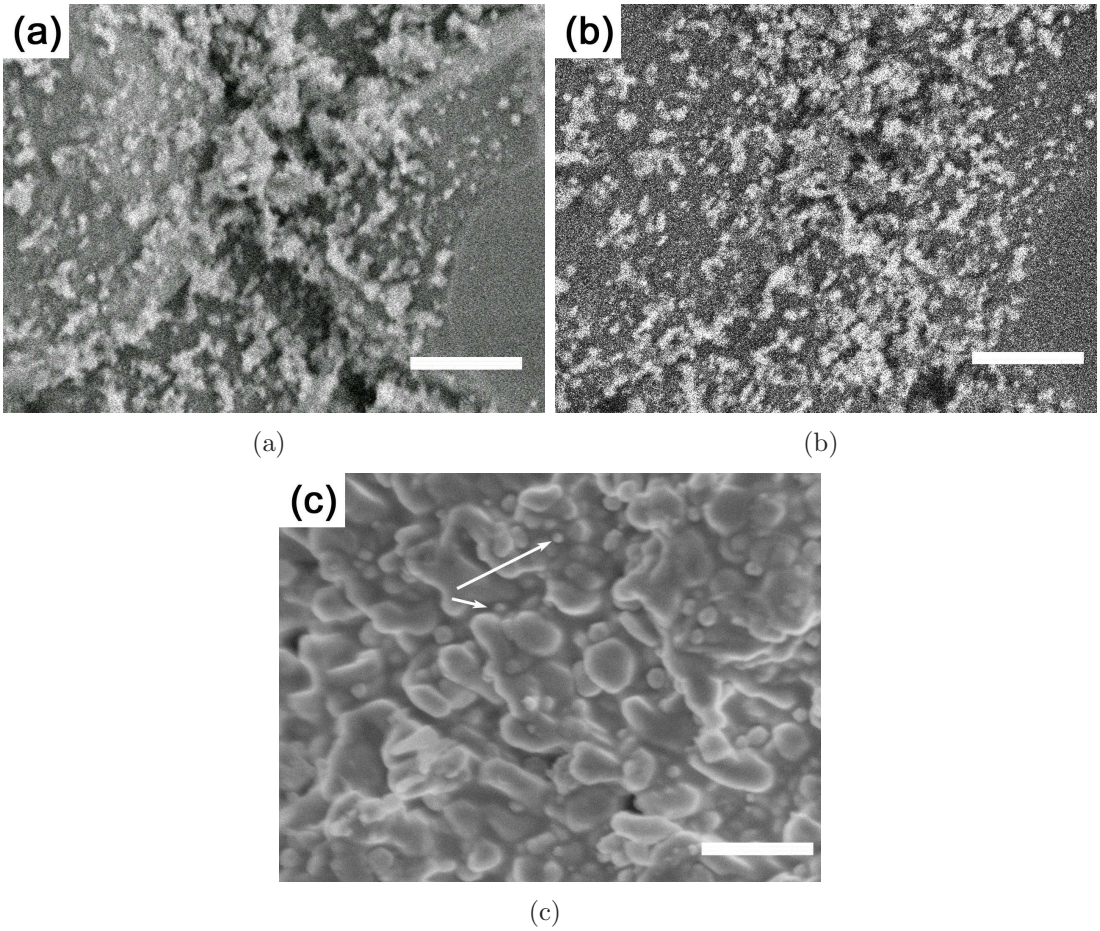

Figure 4.4: SEM micrographs of used Rh-Ce catalysts. All scale bars are 500 nm. (a). Secondary electron detection image of Rh-Ce/γ-Al_2O_3 monolith. Smooth surfaces are the α-Al_2O_3 monolith and clusters are γ-Al_2O_3 washcoat and Rh-Ce particles. (SEI, 2.5 kV, x30,000, WD 10.2 mm) (b). Backscattered electron detection of the same location as image ((a)). Rh-Ce is dispersed on washcoated areas. (BSE, 2.5 kV, x30,000, WD 10.2 mm) (c). Secondary electron detection image of Rh-Ce impregnated spheres. Arrows point out two particles of Rh-Ce on the support surface. (SEI, 2.5 kV, x100,000, WD 3.7 mm)

catalysts were investigated as they have been shown to be stable for long periods of time at high operating temperatures without signs of coke formation or catalyst deactivation.[106] However, it is desirable to minimize the endothermic partial oxidation and reforming activity of the catalyst in order to maximize the extent of pyrolysis reactions. Pt is frequently used as a combustion catalyst and has been shown to have minimal reforming activity downstream of the oxidation zone in the catalyst bed.[107,108] Experiments 3, 4, 9, and 10 of Table 4.1 show that Pt spheres select for 10 % less CO than the same experiments over a Rh-Ce/γ-Al_2O_3 monolith. Pt spheres also yielded lower CO_2 and H_2 selectivities, indicating less overall partial oxidation rather than consumption of CO by the water-gas-shift reaction.[109]

Hydrogen was added to the feed gases to investigate the effect of a sacrificial fuel on S_{PP}. Experiments were performed with a constant gas flow rate and an increased N_2 flow (2.5 SLPM) as a safety precaution for lab-scale operation. The cellulose flow rate was varied to obtain the desired C/O ratio (Fig. 4.3). Over the Pt sphere fixed bed, autothermal, steady state operation was achieved at cellulose flow rates up to 100 g $hr^{-1}$with S_{PP} of 45 % without addition of H_2. Addition of 0.4 SLPM H_2 consistently increased S_{PP} by 10-15 %. A similar trend was seen for H_2 addition over Rh-Ce/γ-Al_2O_3 monoliths (Table 4.1). The rapid consumption of O_2 by reaction with H_2 limited the O_2 available to react with cellulose pyrolysis vapors. Previous work by Donazzi et al. shows the selective oxidation of H_2 over Rh/α-Al_2O_3 during the catalytic partial oxidation of CH4.[110] Additionally, Michael et al. demonstrated the sacrificial oxidation of H_2 in a catalytic partial oxidation system to increase the yield of olefin products.[111] This effect is attributed to the higher sticking coefficient on noble metal catalysts and the higher diffusion coefficient of H_2 than alkanes in a mass transfer limited system.

4.4 Conclusions

Experiments have demonstrated that a fixed-bed catalytic pyrolysis reactor can run autothermally to produce high yields of pyrolysis oil from cellulose with no observable char formation. These properties allow for continuous operation without the need for external heating, thus increasing the overall energy efficiency of pyrolysis oil production. The use of platinum spheres, which favor combustion and have low reforming activity, along with a high C/O feed ratio of 1.7 maximizes carbon selectivity to pyrolysis oil. H_2 addition as a sacrificial fuel improved reactor performance at higher cellulose feed rates and lower C/O ratios. Preliminary product characterization has

revealed a very acidic liquid product (pH $\sim$ 2) with acetic acid, formic acid, propanoic acid, phenol, and levoglucosan as major products, which agrees with previous work. [112,113] However, a much more detailed analysis is required. Future experimentation and characterization of the pyrolysis oil product is proposed and discussed in Chapter 6.

4.5 Acknowledgments

We would like to thank Reetam Chakrabarti for obtaining the SEM micrographs printed in this article. Parts of this work were carried out in the Characterization Facility, University of Minnesota, which receives partial support from NSF through the MRSEC program.This article is also based on work supported under a National Science Foundation Graduate Research Fellowship and partially supported by U.S. Department of Energy Grant DE-FG02-88ER13878.

CHAPTER

FIVE

EFFECT OF ALKALI METAL IMPURITIES ON CO-RE CATALYSTS FOR FISCHER-TROPSCH SYNTHESIS FROM BIOMASS-DERIVED SYNGAS[1]

Chapters 2, 3, and 4 discussed catalytic oxidative pyrolysis of lignocellulosic biomass as an alternative technology to traditional pyrolysis. Gasification of biomass followed by Fischer-Tropsch (FT) processing is another means to produce liquid products. The Schmidt group has previously demonstrated the ability to produce clean synthesis gas with high selectivity from biomass (Section 1.2.3). Here, the effect of biomass inorganics is discussed in the context of processing biomass-derived synthesis gas over a Co-based Fischer-Tropsch catalyst. The effects of Na, K, Li, and Ca impurities on γ-Al_2O_3-supported CoRe powder catalysts were studied at impurity loadings between 25 and 1,000 ppm. Impurity addition did not have any effect on H_2 chemisorption, but the catalyst activity decreased during FT synthesis experiments. The impurities were also found to slightly increase the reduction temperatures of Co. Carbon selectivities to CH_4 decreased with increasing impurity loading, while CO_2 and C_{5+} hydrocarbon selectivities increased. Catalyst behavior was attributed mostly to electronic effects from the alkali addition, leading to decreased surface H concentrations and increased CO adsorption and dissociation.

[1]Portions of this chapter appear in C.M. Balonek, A.H. Lillebo, S Rane, E. Rytter, L.D. Schmidt, A. Holmen, "Effect of alkali metal impurities on Co-Re catalysts for Fischer-Tropsch synthesis from biomass-derived syngas," *Catalysis Letters* **138** (2010) 8-13.

5.1 Introduction

Recent interest in alternative fuel sources has been motivated by increasing environmental concerns and fossil fuel prices. Biomass represents the only practical renewable source of carbon, necessary for the production of liquid hydrocarbon fuels and chemicals. Biomass to liquids (BTL) is a process that gasifies biomass to synthesis gas (syngas) and then utilizes processes such as Fischer-Tropsch (FT) synthesis to create liquid fuels from syngas. FT synthesis using coal-derived syngas is a well-understood process to create synthetic gasoline (CTL). However, using biomass-derived syngas as the feedstock (BTL) involves mitigating a new set of impurities that may affect catalyst performance.

Biomass ash refers to the total inorganic content present in biomass and typically contains alkali metals, in particular sodium and potassium.[114–116] Potassium is a common promoter for FT and ammonia synthesis over unsupported iron catalysts.[35,117,118] Compared to iron catalysts, Co catalysts have shown to have high stability and selectivity to normal paraffins and have a lower deactivation rate.[24,119] Re is used as a promoter for Co catalysts to improve Co dispersion and facilitate reduction.[120] However, studies regarding the addition of potassium and other alkalis to cobalt catalysts are limited because they have been shown to severely reduce catalyst activity.[35] Existing studies examine K on various metal surfaces, but investigation of other alkalis are also limited. Alkaline earth elements are also found in biomass ash[121,122], but again research is limited. Therefore, we have chosen to study the effects of sodium, potassium, lithium, and calcium over Co-Re FT catalysts at ppm levels commonly present in biomass-derived syngas.

Impurity loading on the Co-Re/γ-Al_2O_3 catalyst was varied between 25 and 1000 ppm by weight to study the effect on Co dispersion and catalyst reducibility and performance. In a commercial process, inorganics may be introduced to the reactor in a variety of ways, e.g. as ash entrained in the syngas stream. The following experiments do not seek to investigate the mechanisms of inorganic introduction or deposition on the catalyst surface, but rather to study the effects of inorganics on catalyst performance once on the surface. Co dispersion and catalyst reducibility were investigated using hydrogen chemisorption and temperature programmed reduction, respectively. Catalyst performance was studied during FT synthesis reactions by measuring site-time yields and selectivities to common products.

Table 5.1: Catalysts prepared with the indicated metal impurities and loadings.

Metal Impurity	Impurity Loading (ppm)	Co Dispersion (%)	Reduction Temperature (°C) $Co_3O_4 \rightarrow CoO$	$CoO \rightarrow Co$
None[1]	0	7.9	372	589
Na	25	8.1	383	600
	50	7.8	381	598
	100	7.8	390	615
	200	8.2	391	602
	500	7.8	385	601
	1000	7.8	382	600
Li	200	8.1	381	596
	500	8.0	383	598
	1000	7.9	380	598
Ca	200	7.9	378	594
	500	8.2	378	597
	1000	8.0	381	604
K	200	7.9	384	598
	500	8.0	385	603
	1000	8.1	379	601

[1]Referred to as the "standard" catalyst.

5.2 Experimental

5.2.1 Catalyst Preparation

Catalysts were prepared by incipient wetness technique on 53 - 90 μm γ-Al_2O_3 powder. The support was Sasol GmbH Puralox SCCa γ-Al_2O_3 (BET 162 m^2 g^{-1}, pore volume 0.6 cm^3, average pore diameter 10.2 nm). 20 wt% Co and 0.5 wt% Re were co-impregnated as $Co(NO_3)_2 \cdot 6H_2O$ and $HReO_4$, respectively. Catalysts were dried, then calcined in air at 300 °C for 16 hours. Metal impurities were then impregnated onto the catalyst as nitrates using the incipient wetness technique to achieve the desired ppm loading with an error generally less than 0.5 % (Table 5.1). Catalysts were again dried and calcined in air at 300 °C for 16 hours. Following calcination, the added alkali metals likely exist as metal oxides on the catalyst surface. However, efforts to characterize the state of the impurities would not correspond to that during reactor operation. Catalysts prepared without impurities are referred to as "standard" catalysts hereafter. Catalysts used for Fischer-Tropsch synthesis were sieved to 53-90 μm particle diameter.

5.2.2 Hydrogen Chemisorption

To study the effect of metal impurities on Co dispersion, hydrogen chemisorption was performed on a Micromeritics ASAP 2010 unit. Prior to chemisorption, the catalysts were reduced in situ under H_2 at 350 °C for 16 hours (ramp rate of 1 °C min^{-1} from 20 °C), then cooled to 40 °C under vacuum. To calculate the dispersion from the resulting adsorption isotherms between 0.020 and 0.667 bar, it was assumed that one Co site is occupied by one H atom and that neither Re nor the impurity adsorb hydrogen.[120,123] Reported dispersion data are an average of two chemisorption measurements.

5.2.3 Temperature Programmed Reduction

Temperature programmed reduction (TPR) was performed in a quartz reactor tube under a flow of 7 % H_2 in Ar. The catalyst and reactor tube were heated in a furnace at 10 °C min^{-1} from 20 °C to 935 °C. Effluent passed through a 2-propanol and dry ice cold trap before hydrogen consumption was analyzed using a thermal conductivity detector (TCD).

5.2.4 Fischer-Tropsch Synthesis

FT synthesis was carried out in a stainless steel, 10 mm ID fixed bed reactor at 210 °C and 20 bar with a syngas feed of $H_2/CO = 2.1$. 1 g of catalyst was mixed with 4 g of inert SiC to improve heat distribution throughout the catalyst bed, then loaded with quartz wool into the reactor tube.

The catalyst was reduced in situ under H_2 with a temperature ramp of 1 °C min^{-1} to 350 °C and held for 16 hours. The catalyst was then cooled to 170 °C, pressurized to 20 bar, and the syngas feed was introduced at 0.25 SLPM. The temperature was then ramped at 0.5 °C min^{-1} to 190 °C, then 5 °C h^{-1} to 200 °C, and finally 0.1 °C min^{-1} to 210 °C. The synthesis experiments were run in two stages. First, a constant syngas feed rate of 0.25 SLPM was maintained. Next, the feed rate was adjusted to maintain $\sim$ 50 % conversion of inlet CO as measured by a gas chromatograph. Reported data were obtained after $\sim$ 30 hours on stream at constant volumetric syngas feed rate and at $\sim$ 24 hours on stream at constant CO conversion ($\sim$ 54 total hours on stream), i.e. after the feed had been adjusted to give a CO conversion of $\sim$ 50 %.

Two traps were maintained downstream of the catalyst bed at 90 °C and 20 °C to

condense heavy hydrocarbon and liquid products, respectively. Gases lighter than C_5 hydrocarbons were then fed to an HP 6890 gas chromatograph with a GS-Alumina PLOT column, TCD, and flame ionization detector (FID) for identification and quantification. The GC quantified species to within 0.5 %. The $\sim$ 3 % N_2 present in the feed gas served as an internal standard for quantification.

5.3 Results

5.3.1 Hydrogen Chemisorption

Dispersion of Co metal on the catalysts calculated from H_2 chemisorption data is presented in Table 5.1. All catalysts had a dispersion of $\sim$ 8 $\pm$ 0.5 % and the impurity metals had an indistinguishable effect on Co dispersion, even at 1000 ppm loading. Previous work demonstrated that potassium loading of 0.4 wt% over γ-Al_2O_3-supported Co decreased dispersion by 1.2 %, which was assumed to be due to blockage or poisoning of the cobalt sites by the alkali.[117] However, this loading was 4 times greater than the 1000 ppm loading examined here, and it is likely that the effect of such low alkali loadings falls within the error of the chemisorption unit.

5.3.2 Temperature Programmed Reduction

The hydrogen consumption profiles obtained during temperature programmed reduction of the standard and 1000 ppm-loaded catalysts are plotted in Figure 5.1. The two main peaks of the profiles are associated with the two-step reduction of cobalt(II,III) oxide to cobalt metal: at $\sim$ 385 °C Co_3O_4 is reduced to CoO, and at $\sim$ 600 °C CoO is reduced to Co metal.[117,120] The much smaller third peak present at $\sim$ 310 °C results from the reduction of residual nitrates present after calcination. The temperatures of the cobalt reduction peaks for all catalysts are listed in Table 5.1. While the shape of the profiles was consistent for all catalysts, the peak temperatures of catalysts loaded with impurities increased $\sim$ 5 - 15 °C compared to those of the standard catalyst. This indicates that adding alkali impurities to the catalyst hinders its reducibility.

5.3.3 Fischer-Tropsch Synthesis

FT synthesis data is reported after $\sim$ 30 hours of catalyst operation at constant feed rate and $\sim$ 24 hours at 50 % conversion of CO feed. Catalyst activity is reported as site-time yields (STY = mol CO converted·mol Co sites^{-1} s^{-1}) and plotted in

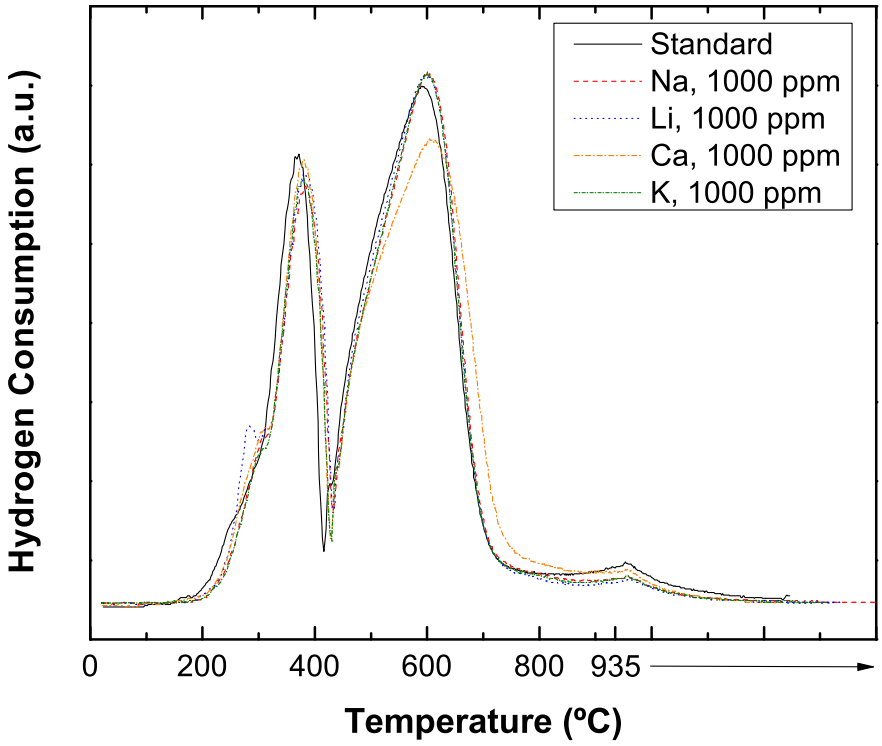

Figure 5.1: TPR profiles of temperature vs. hydrogen consumption of standard and 1000 ppm-loaded catalysts.

Figures 5.2(a) and 5.2(b). As the Na loading increases to 1000 ppm, the site-time yield decreases by roughly half as compared to the standard catalyst. Li, Ca, and K also decrease catalyst activity at 200 ppm loading in the order K > Ca > Li.

Selectivity to C_{5+} hydrocarbons was also affected by alkali metal impurities (Fig. 5.2(c), 5.2(d)). Selectivity increases as Na loading increases, though only by ~ 2 %. CO_2 selectivity also increased minimally with increasing impurity loading (Fig. 5.3(a), 5.3(b)). Finally, Figures 5.3(c) and 5.3(d) illustrate a decrease in CH_4 selectivity with increasing impurity loading. However, 200 ppm loading of calcium had only a very small effect on CH_4 selectivity and slightly decreased C_{5+} hydrocarbons.

5.4 Discussion

Addition of Na, K, Li, and Ca to Co-Re/γ-Al_2O_3 catalysts had a measurable effect on both catalyst reducibility and FT synthesis performance, despite an indistinguishable

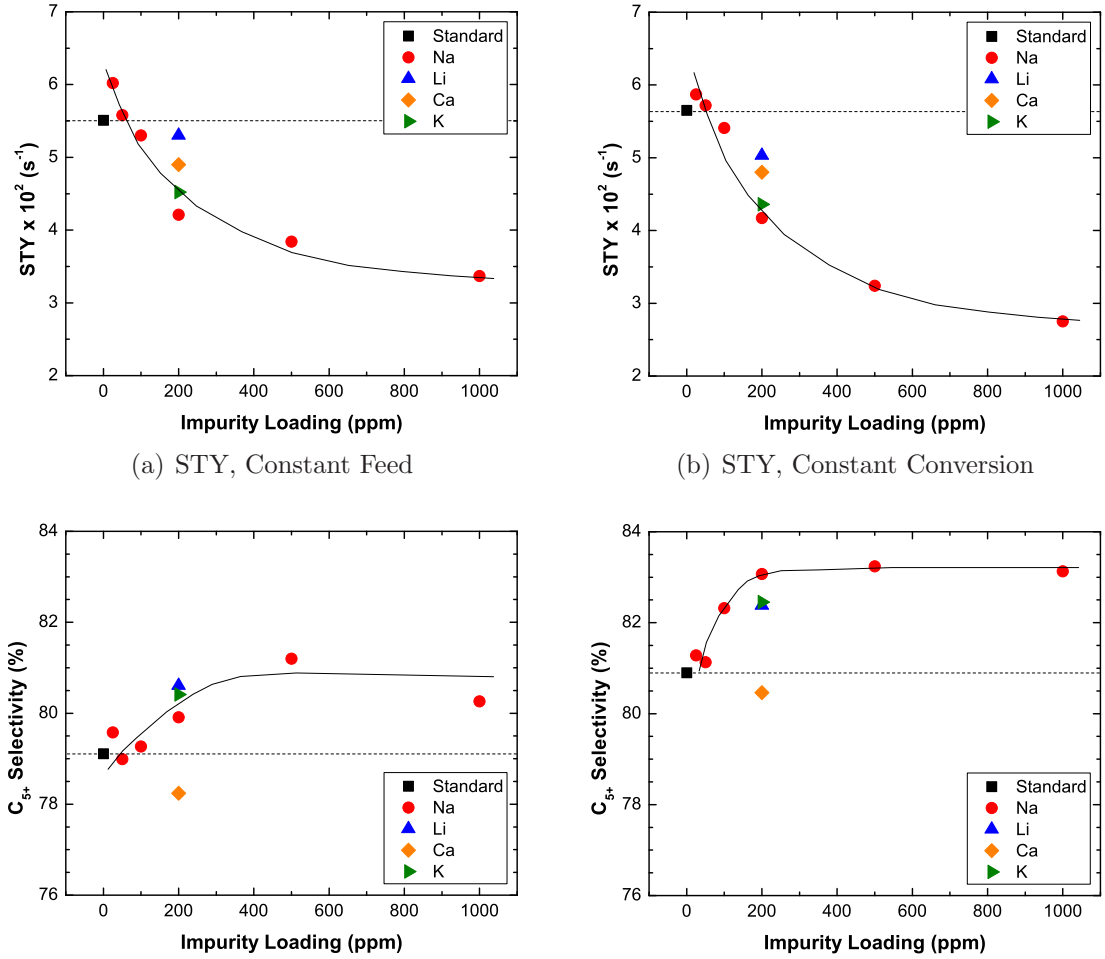

(a) STY, Constant Feed

(b) STY, Constant Conversion

(c) C_{5+} Selectivity, Constant Feed

(d) C_{5+} Selectivity, Constant Conversion

Figure 5.2: Metal impurity loading vs. (a),(b) catalyst STY and selectivities to (c),(d) C_{5+} at constant syngas feed experimental conditions and constant CO conversion, as indicated. Trend lines are to guide the eye.

effect during hydrogen chemisorption. The temperatures of both Co reduction steps increased by 10 °C with addition of only 25 ppm Na. This inhibition of catalyst reducibility may be attributed to increased Co-support interactions upon addition of alkali promoters, which has been theorized in previous work. Trepanier et al. observed a slight increase in reduction temperatures ($\sim$ 5 - 10 °C) of carbon nanotube-supported Co catalysts with addition of 33 and 66 ppm K.[119] Ma et al. observed a larger change by adding 2 wt% K to 15 wt% Co supported on activated carbon, which increased reduction temperatures by $\sim$ 25 °C.[124]

The changes in catalyst performance during FT synthesis can be a result of geometric effects, i.e. site blockage. Alkalis can cover otherwise active Co sites and

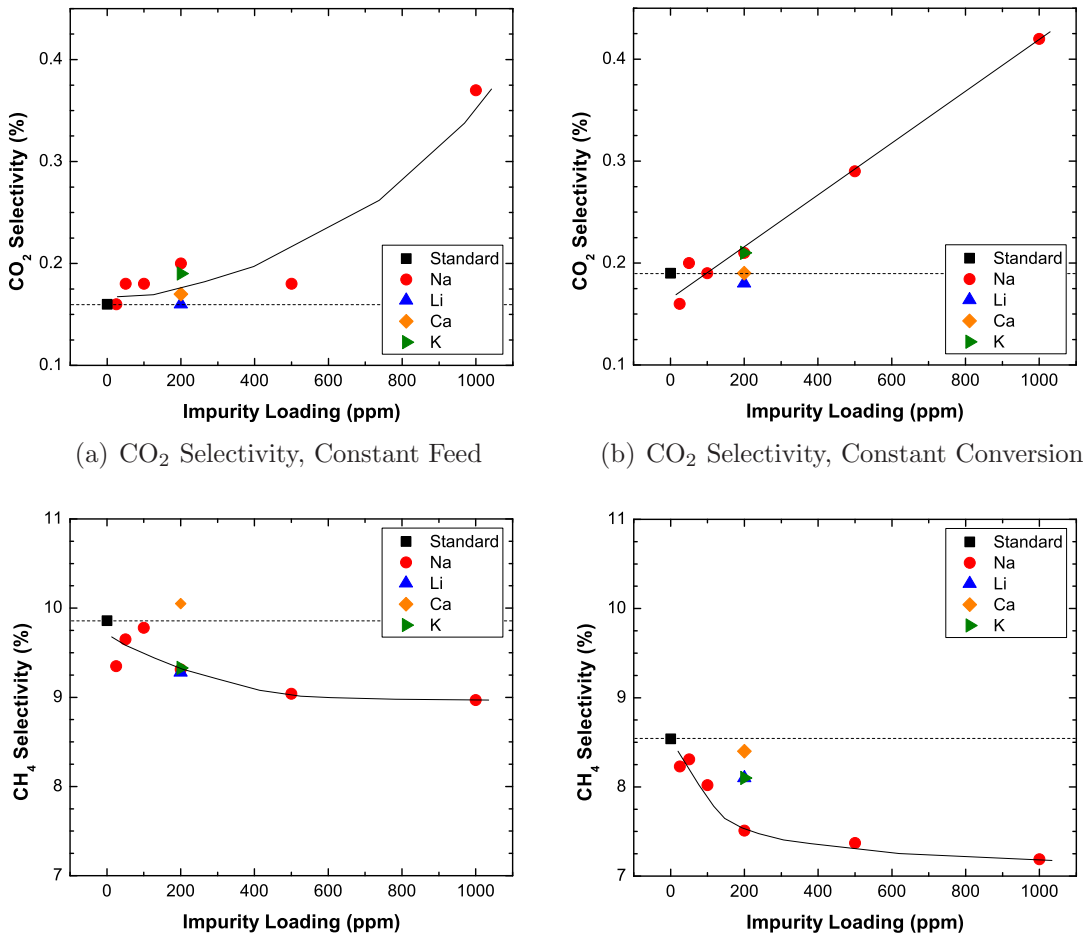

(a) CO_2 Selectivity, Constant Feed

(b) CO_2 Selectivity, Constant Conversion

(c) CH_4 Selectivity, Constant Feed

(d) CH_4 Selectivity, Constant Conversion

Figure 5.3: Metal impurity loading vs. selectivities to (a),(b) CO_2 and (c),(d) CH_4 at constant syngas feed experimental conditions and constant CO conversion, as indicated. Trend lines are to guide the eye.

discourage H_2 dissociation, as H_2 generally requires two adjacent metal sites to dissociate.[123,125] A decrease in available surface H reduces CH_4 selectivity and increases selectivity to larger hydrocarbon products[124,126,127], both observed in the present work. However, the chemisorption results indicated that the addition of up to 1000 ppm of impurity did not affect the hydrogen adsorption. Considering the very low impurity loadings examined here in combination with negligible changes in the amount of hydrogen adsorbed, we surmise that geometric effects from alkali loadings were minimal and electronic effects were largely responsible for the changes observed during FT synthesis.

We postulate that the electronic effects can be attributed to the changes in the adsorption of the reactants on the catalyst surface. Electropositive alkalis added to the Co catalyst transfer charge to the catalyst surface, inducing "long-range electronic effects" and influencing H_2 and CO adsorption and dissociation.[118,123,125,128–131] K addition to Fe(100), Fe(111), Pt(111), and Pd(100) has shown to increase the adsorption energy of H_2, decrease the sticking coefficient of H_2, stabilize H_2 on the surface, and discourage dissociation due to electron donation from K to the bulk metal.[118,123,125,128,130] Blekkan et al. associated this decrease in available surface H with less catalytic activity and a higher hydrocarbon selectivity for K on Co.[117]

A study by Ma et al. showed that the selectivity to CO_2 increased with increased K loading on activated carbon-supported Co catalysts, which was attributed to an increase in water gas shift activity resulting from an increase in adsorbed CO species.[124] Several other studies discuss the increased adsorption and dissociation of CO on Fe and Co.[35,118,126,129] Previous work credited these adsorption effects for reducing methane formation on activated carbon-supported Co[124] and Fe[126] catalysts, increasing water-gas-shift activity[124], and increasing selectivity to large hydrocarbons on Fe[126,127], carbon nanotube-supported Co[119], and other supported FT catalysts.[117] In agreement with these studies, we observed significant reduction in catalyst activity, increased selectivity to C_{5+} hydrocarbons, decreased selectivity to methane, and a slight increase in CO_2 production.

5.5 Conclusions

This work examined the effect of ppm-level alkali impurities on Co-based FT catalysts. The behavior of such impurities, specifically sodium, is important for understanding the effects that biomass-derived syngas may have on FT synthesis over Co-Re catalysts. Alkalis had a negligible effect on Co dispersion and slightly hindered catalyst

reducibility by increasing the Co reduction temperatures. Na was found to greatly decrease catalyst activity and selectivity to CH_4, while increasing selectivity to CO_2 and C_{5+} hydrocarbons. Such effects are attributed minimally to geometric effects of surface alkalis, which can block active catalyst sites, and mostly to electronic effects which have been shown previously to affect H_2 and CO adsorption and dissociation.

5.6 Acknowledgments

This material is based upon work supported under a National Science Foundation Graduate Research Fellowship. Support was also received from the Research Council of Norway and the Norwegian University of Science and Technology. Statoil is acknowledged for providing the standard catalysts.

CHAPTER

SIX

FUTURE WORK

Current thermochemical methods for converting lignocellulosic biomass to liquid products include pyrolysis and gasification/Fischer-Tropsch. However, both methods have challenges that limit their use on a commercial scale. Pyrolysis technologies are energy intensive, create undesirable solid char, and are not chemically selective. Gasification operations require large-scale facilities to be economical and extensive downstream cleanup of the syngas before reaction in a Fischer-Tropsch unit. Catalytic oxidative pyrolysis of solid biomass to liquid products may provide a small-scale, efficient, and economical alternative to traditional technologies.

Chapter 1 introduced millisecond catalytic autothermal reforming technology after discussing the disadvantages and current state of commercial biomass to liquid technologies. Chapter 2 demonstrated the existence of an intermediate liquid during the catalytic reforming of cellulose, while Chapters 3 and 4 examined the extension of this technology to perform autothermal oxidative pyrolysis of biomass models for liquid production. After successful demonstration of pyrolysis oil production from cellulose in an autothermal catlaytic reactor, it is of interest to be able to characterize the resulting pyrolysis products. Chapter 6 will discuss characterization of cellulosic pyrolysis oil and examine the effect of operating conditions and catalyst metal on product selectivity and tunability. Also discussed in this chapter are experiments to study oxidative pyrolysis of plastic feedstocks.

Table 6.1: Typical properties of wood pyrolysis bio-oil and of heavy fuel oil.[134]

Physical Property	**Bio-oil**	**Heavy Fuel Oil**
Moisture Content, wt%	15-30	0.1
pH	2.5	-
Specific Gravity	1.2	0.94
Elemental Composition, wt%		
C	54-58	85
H	5.5-7	11
O	35-40	1.0
N	0-0.2	0.3
ash	0-0.2	0.1
HHV, MJ kg^{-1}	16-19	40
Viscosity (at 50 °C), cP	40-100	180
Solids, wt%	0.2-1	1

6.1 Selectivity of Cellulosic Pyrolysis Oil

There are several characteristics of biomass-based pyrolysis oil that inhibit its widespread use with existing technologies. First, pyrolysis oil has a very high oxygen content when compared to fossil fuels (Table 6.1). The abundance of alcohols, acids, and other oxygenated species results in a low pH and a low heating value of the pyrolysis oil. The corrosiveness of the oil can make it difficult to use in existing infrastructure. The large water content of pyrolysis oils also contributes to the low heating value and severely limits the use of pyrolysis oil in ignition engines.[132] A study by Shihadeh and Hochgreb compared the use of No. 2 diesel fuel with two types of pyrolysis oil in a direct injection diesel engine.[133] They found that the pyrolysis oils had significant ignition delays and required air preheating to combust reliably. Pyrolysis oils are also known for being reactive over time, resulting in larger molecules and higher viscosities that can negatively impact use of the fuel.

Chapter 4 demonstrated the ability of an autothermal catalytic oxidative pyrolysis reactor to convert cellulose with high carbon selectivities to pyrolysis products. Ideally, the liquid product would be tunable and selective to desired compounds. To investigate the ability of the reactor to accomplish this, involved characterization of the pyrolysis oil is necessary. In particular, the identification and quantification of product species by GCMS, pH, water content, and aging characteristics will be studied.

6.1.1 Experimental Details

Catalyst Selection

Pyrolysis oil production will be conducted over Rh, Rh-Ce, Pt, and Pt-Sn catalysts. The catalyst bed will be 3.1 g (equivalent to 1 cm bed height) of 1.3 mm diameter α-Al_2O_3 spheres. Results in Chapter 4 showed that catalyst deposited on α-Al_2O_3 spheres, rather than monoliths, had higher carbon selectivity to pyrolysis products, which may be a consequence of higher O_2 consumption rates and front face temperatures. Therefore, spheres are chosen for these experiments to maximize pyrolysis oil yields.

Rhodium catalysts used in catalytic partial oxidation have consistently demonstrated high fuel conversions, high syngas yields, high stability, and resistance to coke deposition.[38,39,41,135] Rh has a high tendency to produce H_2 since the activation barrier to dimerize hydrogen is lower than that of OH and H_2O. Previous experiments have shown that catalyst loadings between 0.05 and 15 wt% Rh loading had very little effect on fuel conversion and product selectivities.[38,42,43] 2.5 wt% Rh loading is chosen for experiments to be well within this region.

Addition of cerium to a Rh catalyst is chosen based on cerium's ability to stabilize the noble metal catalyst, improve desired product selectivities, and prevent coke formation. Previous research has consistently shown that metal catalysts have significantly higher selectivities to syngas upon cerium addition due to increased water-gas-shift activity.[40–42] Addition of cerium also increases the stability of metal catalysts by increasing oxidation rates on the surface, preventing coke formation.[90] As an active oxidation catalyst, cerium can store and donate oxygen for reactions on Rh sites.[41,90,92,93]

Platinum was chosen as the second noble metal catalyst based on its ability to select for larger hydrocarbons and combustion products, rather than synthesis gas. Minimizing partial oxidation of cellulose, which is endothermic, and selecting for complete oxidation can maximize heat available for pyrolysis reactions while sacrificing the least amount of feedstock. Pt has previously been shown to be a very effective catalyst for olefin production by oxidative dehydrogenation, as well as an effective combustion catalyst with minimal endothermic reforming activity.[38,107,108] Chapter 4 discusses the higher yields of pyrolysis products obtained over a Pt catalyst when compared to Rh-based catalysts. Finally, Sn is proposed as an additive to Pt to further promote oxidation activity.[136]

Catalyst Preparation

Catalysts will be prepared on 1.3 mm diameter α-Al_2O_3 spheres. Rhodium catalysts with a desired loading of 2.5 wt% are prepared by creating an aqueous solution of Rh, as $Rh(NO_3)_3$, and using an incipient wetness technique to apply the solution dropwise to the blank α-Al_2O_3 spheres. The coated and dried spheres are then calcined for 6 hours at 600 °C in air at atomspheric pressure. Rh-Ce catalysts are also prepared in a similar manner, with a desired loading of 2.5 wt% each of Rh and Ce, using an aqueous solution of Rh and Ce, as $Ce(NO_3)_3{\cdot}6H_2O$, to coat blank spheres. Platinum catalysts are prepared similarly, with a desired loading of 2.5 wt%, using an aqueous solution of Pt, as H_2PtCl_6, but rather than calcining in air, Pt catalysts are reduced under a mixture of hydrogen and nitrogen by ramping the temperature 5 °C min^{-1} from 25 °C to 500 °C and holding at 500 °C for 6 hours. Pt-Sn catalysts are 2.5 wt% Pt and 2.5 wt% Sn (Tin(II) chloride) and are reduced in the same manner.

Reactor Setup

Similar to experiments discussed in Chapter 4, cellulose pyrolysis will be conducted over a fixed bed catalyst contained in a 19 mm ID quartz reactor tube (Fig. 6.1). The catalyst bed will be 3.1 g of coated spheres, equivalent to a 1 cm bed. Mass flow controllers will feed O_2 and N_2 to the reactor with air stoichiometry. A 0.1 SLPM CH_4 feed will suppress cellulose ignition before reacting the catalyst bed.[100] A Schenck AccuRate auger/hopper system will feed 60 g h^{-1} of 300 μm microcrystalline cellulose to the reactor. A round bottom flask will collect liquid products and be placed into a dry-ice bath to maximize condensation. The effects of N_2 and O_2 feed rates and catalyst metal on the pyrolysis oil yields and composition will be studied.

During reactor operation a HP 6890 GC will be used to identify and quantify gas samples of oxidation and C_1 products. All carbon species not identified as CO, CO_2, or CH_4 will be grouped and identified as pyrolysis products. Pyrolysis oil collected during reactor operation will be characterized using several different methods. All characterization will be conducted within 6 hours of pyrolysis oil collection. pH will be measured with a Corning Model 430 pH meter. Water content will be measured by the Dean-Stark method, Figure 6.2.[137] The water fraction collected will be characterized with a GCMS to account for any other species that may have remained in the aqueous phase.

In addition to pH and water content measurements, the pyrolysis oil will be analyzed by GCMS. Pyrolysis oil will be filtered using a 0.45 μm PTFE syringe filter

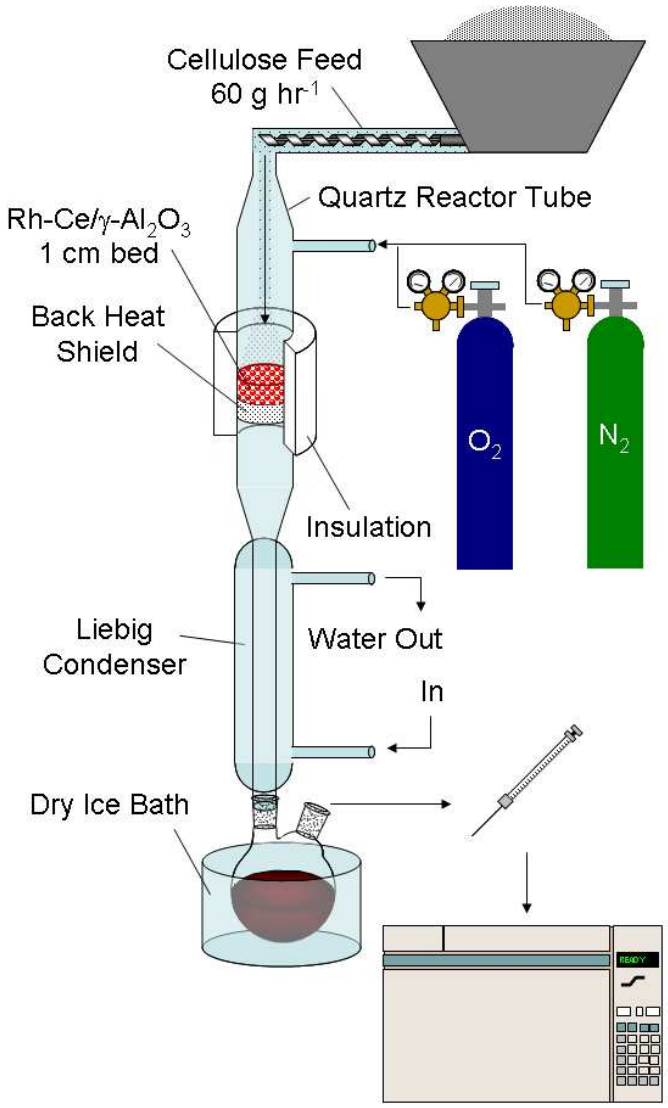

Figure 6.1: Experimental schematic for the collection of pyrolysis oils produced from cellulose feedstock.

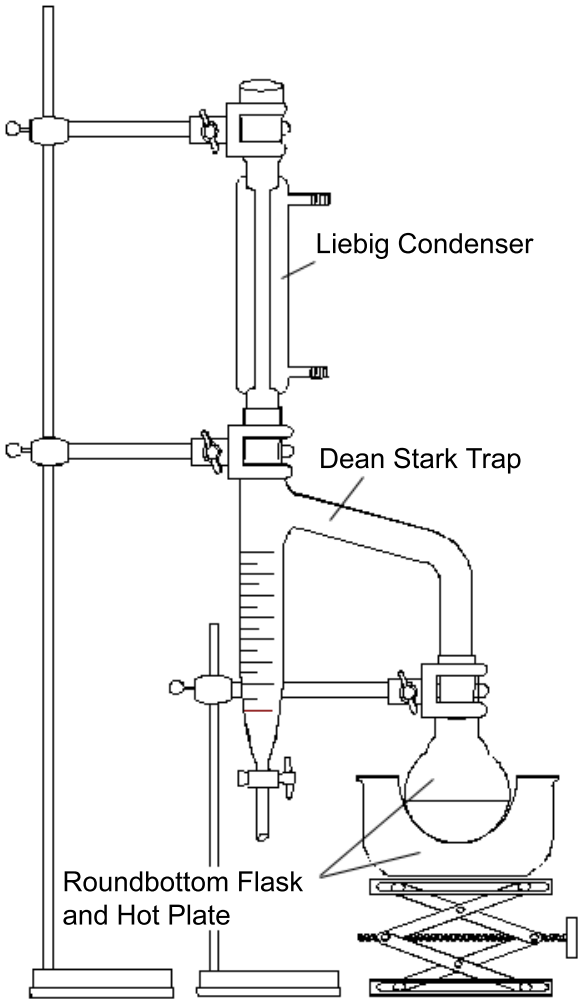

Figure 6.2: Dean stark apparatus used to determine water fraction of pyrolysis oil. Adapted from Academie Reims.[138]

before analysis. An optical microscope was used to identify small particles (2 μm) in the pyrolysis oil during preliminary experiments, which are capable of clogging a GC column. 1 wt% iso-propanol is added to the pyrolysis oil sample as an internal standard. The GCMS is equipped with a 30 m x 0.32 mm x 0.50 μm DB-WAX column to separate pyrolysis species. Peaks were identified on the MS and the twelve largest peaks were selected for calibration (Table 6.2). Example chromatographs (MS Scan mode) with selected species are shown in Figure 6.3. Selected Ion Monitoring (SIM) mode on the MS is used to identify the five most abundant ions for each species for quantification (Table 6.1).[139] Compared to scan mode, SIM mode offers longer dwell times, lower detection limits, and less noise, allowing for more accurate quantification of species.

6.1.2 Preliminary Data/Discussion

Preliminary experiments have been conducted with the 2.5 wt% Pt catalyst. Data has been obtained for both gas and liquid products for C/O ratios (carbon atoms in cellulose feedstock/oxygen atoms in oxygen feed) of 1.2 to 1.8 in 0.1 increments. Cellulose was fed at 60 g hr^{-1} and the catalyst was operated for 20+ hours without observable char formation or deactivation.

Data for non-condensible gases was obtained with a HP 6890 gas chromatograph. H_2, CO, CO_2, and CH_4 were quantified and lumped to determine the mass fraction of gaseous products. Figure 6.4 shows the mass fraction of gaseous products based on the cellulose feed (black squares). The remaining fraction is designated as pyrolysis products. Research groups investigating pyrolysis oil production frequently report mass yields of products. However, pyrolysis oils can contain large amounts of water that contribute to liquid yield, but not to valuable products. Carbon selectivity may be a better metric and therefore the selectivity to gaseous products (CO, CO_2, CH_4) is also shown in Figure 6.4 (gray squares). Again, the remaining portion is attributed to pyrolysis products.

Pyrolysis products were condensed and collected for analysis at each C/O ratio. All samples were a single aqueous phase and did not phase separate with age. Pyrolysis liquids collected at the lowest C/O ratios tested had a light gold/tan color and were semi-transparent. Liquids collected at the highest C/O ratios were dark brown in color and completely opaque. Opaqueness in the samples is attributed to small particles (2 μm), which were filtered before analysis by GCMS. Particulate matter within the liquid product is assumed to be a result of the condensation apparatus

Table 6.2: Pyrolysis oil compounds identified and to be calibrated.

Chemical Name	Formula	Structure	**Selected Ions**
Acetic Acid	$C_2H_4O_2$	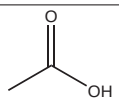	15,42,46,48,60
Formic Acid	CH_2O_2	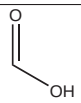	17,29,30,45,46
Propanoic Acid	$C_3H_6O_2$	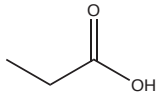	27,28,29,45,74
Propenoic Acid	$C_3H_4O_2$	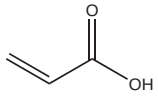	26,27,45,55,72
Ethylene Glycol	$C_2H_6O_2$	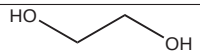	29,31,32,33,43
2H-pyran-2-one	$C_5H_4O_2$	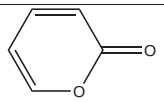	38,39,40,68,96
4H-pyran-2-one	$C_5H_4O_2$	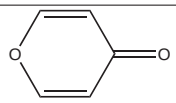	42,68,69,70,96
Phenol	C_6H_6O	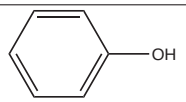	39,40,65,66,94
4-methylphenol	C_7H_8O	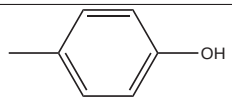	51,77,79,107,108
5-hydroxymethyl-2-furaldyhyde	$C_6H_6O_3$	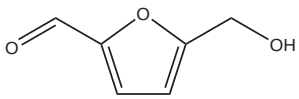	39,41,69,97,126
1,2-benzenediol	$C_6H_6O_2$	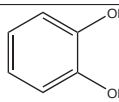	53,63,64,81,110
Levoglucosan	$C_6H_{10}O_5$	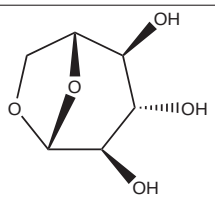	29,56,57,60,73

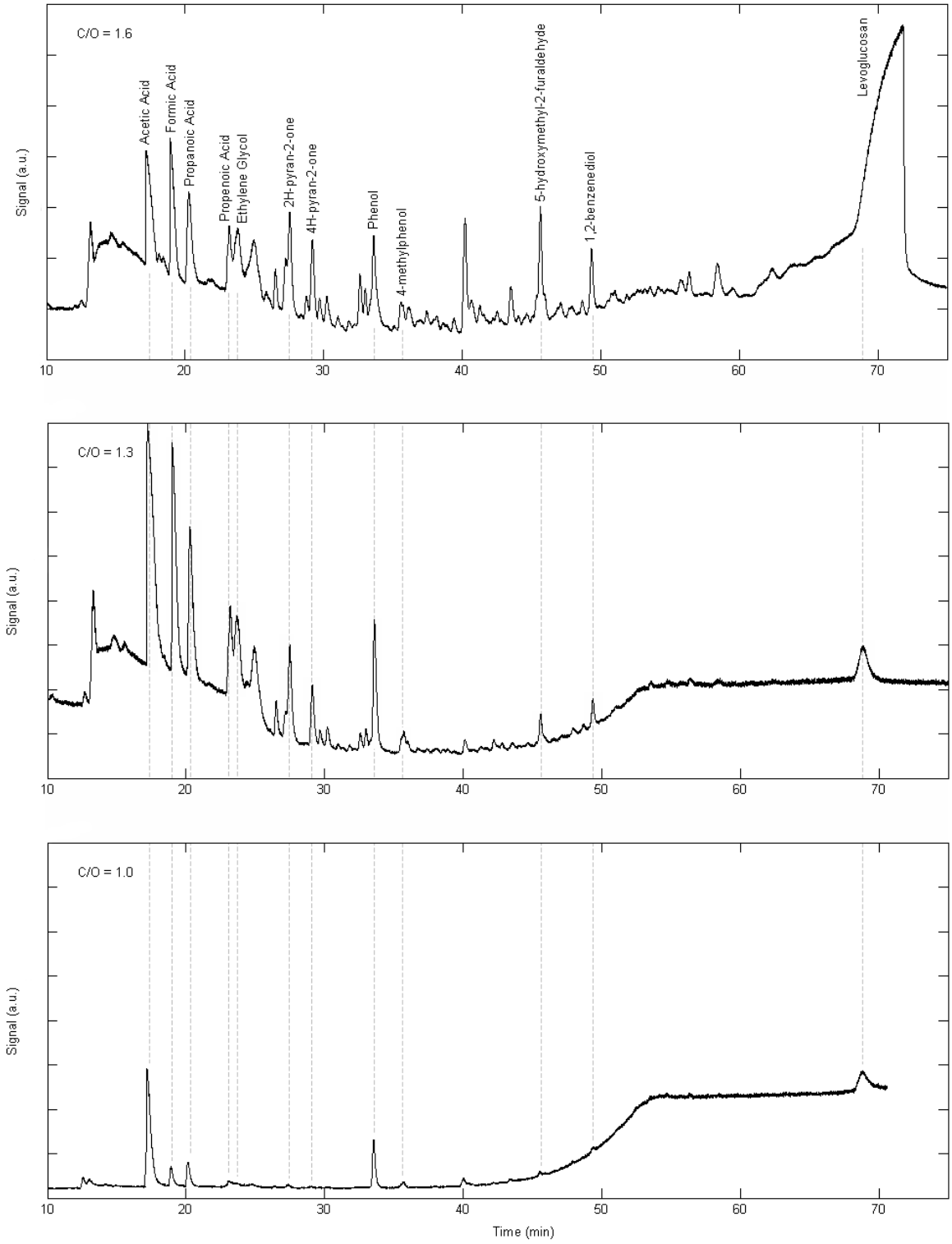

Figure 6.3: Mass spectrometer chromatographs of pyrolysis oil.

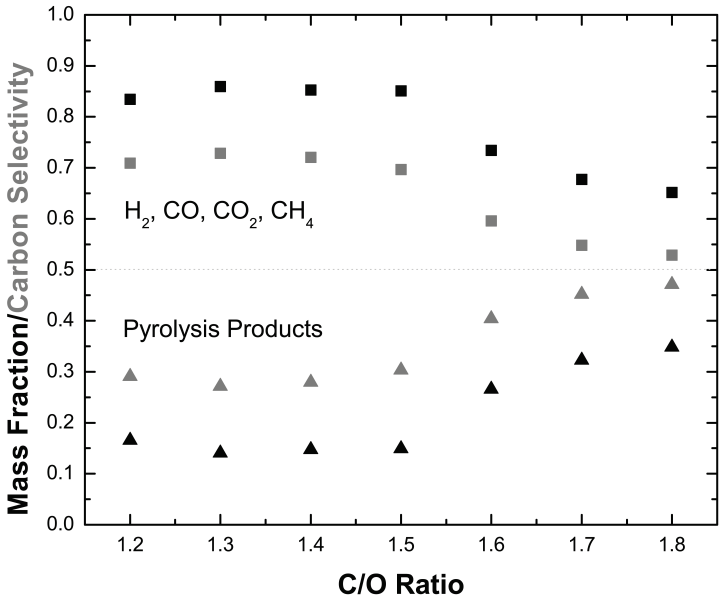

Figure 6.4: Gaseous and pyrolysis products from the oxidative pyrolysis of cellulose over Pt. Squares indicate gaseous products (H_2, CO, CO_2, and CH_4); triangles indicate pyrolysis products. Black symbols indicate mass fraction; gray symbols indicate carbon selectivity.

employed, rather than as a direct result of the catalytic pyrolysis. Immediate cooling of the products is ideal, but unrealistic on the laboratory scale. As mentioned, the catalyst showed no signs of coking or particulate formation during operation.

Figures 6.3, 6.5, and 6.6 highlight some of the preliminary results of the pyrolysis oil analysis. Figure 6.3 shows three MS chromatographs for pyrolysis oils collected at C/O ratios of 1.6, 1.3, and 1.0. Figure 6.5 and 6.6 show the change in pH and water/levoglucosan weight fractions in relation to the change in C/O operating ratio. All other species measured by GCMS were < 1 wt% and are not shown.

At a low C/O ratios, there are few compounds present in the liquid product (bottom panel, Fig. 6.3). The product at C/O = 1.2 is 94 wt% water and has a pH of 2.64. At such low C/O ratios, the relative abundance of oxygen in the reactor increases complete oxidation, as evidenced by the high catalyst temperature and high product selectivity to CO_2 (Fig. 6.7 and 6.8). As the C/O ratio is increased, the catalyst temperature drops steadily, and selectivity to both CO and CO_2 decrease as more carbon remains as pyrolysis products and are condensed. At C/O of 1.6, the chromatograph shows an increase in all products and notably levoglucosan, which increases to 8 wt% of the liquid product at 1.6 and 11 wt% at C/O = 1.8 (Fig. 6.6).

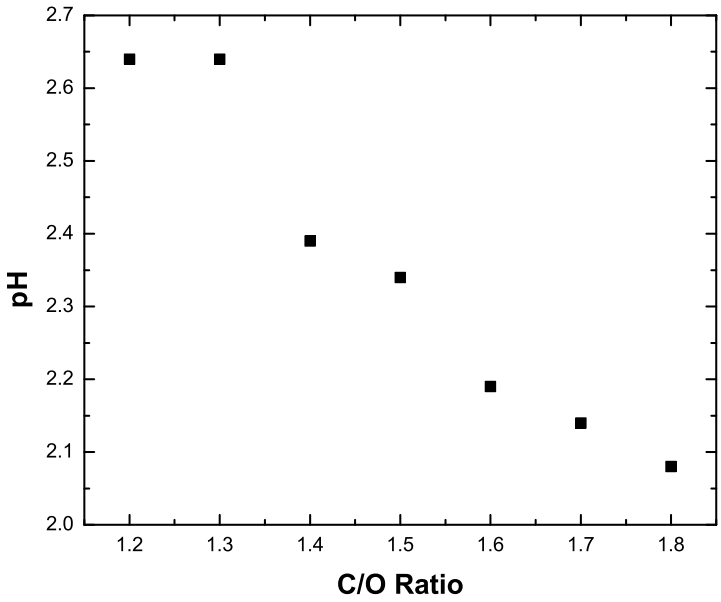

Figure 6.5: pH of pyrolysis oil as a function of reactor C/O ratio.

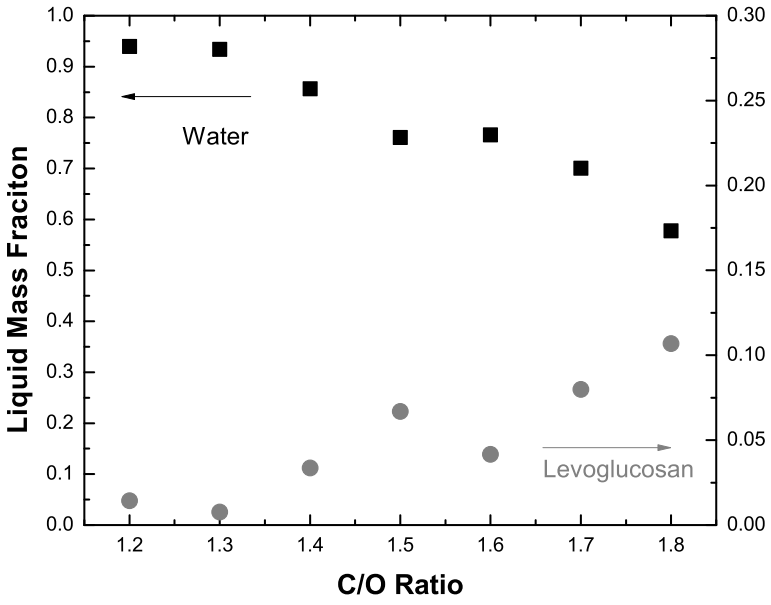

Figure 6.6: Mass fraction of water (measured by Dean-Stark method) and levoglucosan (measured by GCMS) of pyrolysis oil.

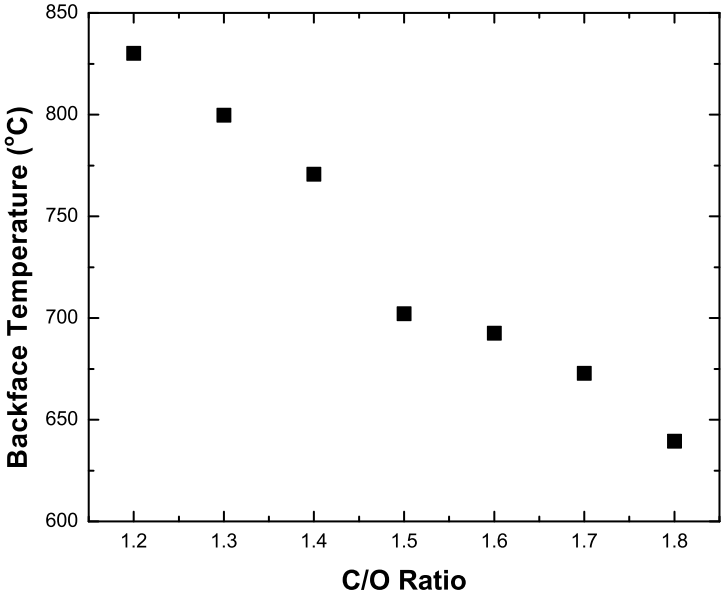

Figure 6.7: Catalyst back face temperatures during operation, measured with a Type-K thermocouple.

Both the pH and water fraction decreased to 2.08 and 58 wt%, respectively. Again, all other species were < 1 wt%.

The proposed Rh, Rh-Ce, and Pt-Sn catalysts remain to be examined and then compared with the preliminary results for the Pt catalyst. Following these experiments, it would be of interest to examine the products resulting from the autothermal oxidative pyrolysis of levoglucosan and hemicellulose. Examining each of these major biomass components separately can simplify the experimental process and eliminate certain complications, such as having a multi-phase liquid product. Additionally, long-term aging experiments of the pyrolysis oil should be conducted. Very fine sediment could be seen accumulating in aged pyrolysis oil collected at C/O ratio of 1.4 over Pt over four weeks. However, no significant changes were observed with MS analysis at one week intervals.

6.2 Oxidative Pyrolysis of Plastics

The efficient conversion of waste plastics to high value liquid fuels and chemicals would provide an alternative route to current technologies. The ability to have high selectivities to plastic monomers would provide an opportunity to directly recycle waste plastics into "virgin" materials. Current pyrolysis technologies to produce liq-

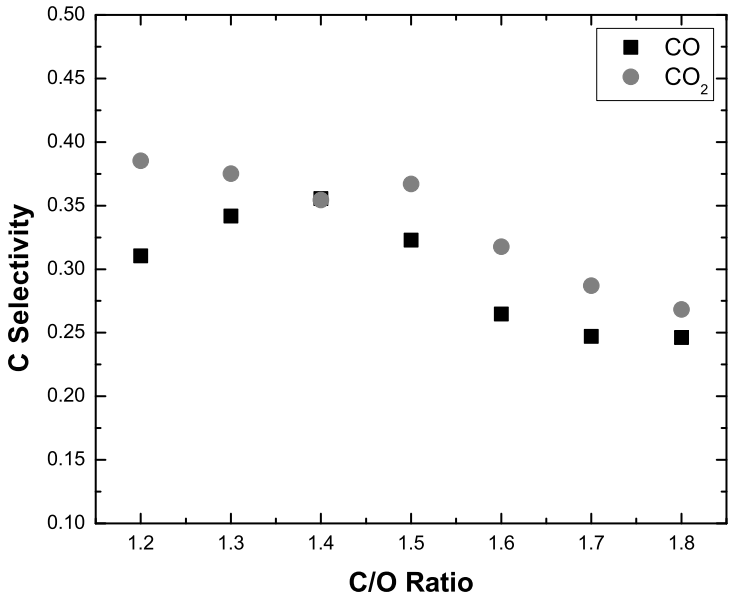

Figure 6.8: Carbon selectivity to CO and CO_2 during pyrolysis experiments.

uid products (similar to biomass-processing technologies) are energy intensive, create large amounts of solid carbon, and are not chemically selective.

Autothermal catalytic oxidative pyrolysis of waste plastics may provide an effective route to produce useful fuels and chemicals in a clean, fast, and efficient manner. A highly heat integrated process, heat produced from oxidatative reactions in the catalyst bed are conducted upstream to the catalyst front face and directly to the solid particles that land on the surface. High heat transfer rates quickly pyrolyze the solids to volatile compounds. Only enough oxidation occurs to maintain autothermal operation.

This process should ideally be able to convert both thermoplastics and thermosets, the two classes of polymers found commercially.

6.2.1 Thermoplastics

Making up $\sim$ 80 % of all US plastic waste, thermoplastics are a class of polymers that have little or no bonding between individual polymer chains and can be softened repeatably when heated.[140] Most thermoplastics can be recycled by traditional primary and secondary recycling methods, however not without degradation of material properties.

The five primary thermoplastics are polyethylene terephathalate (PET), polyethy-

lene (PE), polypropylene (PP), polyvinyl chloride (PVC), and polystyrene (PS). Polystyrene and polyethylene will be chosen to model conversion of plastic waste to liquid products as degradation of these materials produces valuable products for further utilization, in comparison to other thermoplastics.[141] Additionally, experiments involving PS and PE may provide insight for future experiments involving PET and PP. Previous flash pyrolysis of PE and PP have shown to produce similar gas, liquid, and solid product selectivities between 500 and 800 °C.[142] Fluidized bed pyrolysis demonstrated that PE and PP yield very similar molecular weight distribution of aliphatic wax products, including alkanes, alkenes, and alkadienes.[143] However, PP generally produces a larger variety of products than PE due to the methyl side groups.

Flash pyrolysis of PET produces a liquid product of mostly benzene and toluene, as well as a gas phase of H_2 and C_1 - C_3 species. Large amounts of carbon oxides are also produced due to the oxygen present in the polymer.[142] The potential for a wide range of oxygenated products would make characterization of reactor effluent difficult. Pyrolysis waxes of PET have a similar range of molecular weights as PS, and experiments with PS may give insight into PET degradation.[143]

PVC is not proposed for oxidative pyrolysis experiments because of the potential to produce HCl, which can corrode equipment.[140] Additionally, the potential to create highly toxic dioxins is a severe safety concern.

Previous PS pyrolysis research has demonstrated the high selectivity of PS to decompose into its monomer, styrene, and other liquid aromatic products.[140,144] Polystyrene decomposes by random fragmentation and also into its monomer by unzipping reactions.[140] Despite the short residence times of traditional fast pyrolysis processes (generally $\leq$ second), styrene monomers produced can undergo secondary reactions to other aromatic species, such as benzene and toluene. Production of undesirable polyaromatic hydrocarbons, potential carcinogens and coke precursors, is also possible.[145]

Polyethylene decomposes by random fragmentation, producing a large variety of products ranging from $\sim$ 100 - 2000 amu, up to C_{50} species.[140,143,146] PE pyrolysis products are generally of low quality and has "little practical use" due to the very limited product selectivity.[146] In addition to unselective liquid product yields, traditional pyrolysis typically produces solid coke residues. For example, Lee used zeolite Y catalysts to achieve PE pyrolysis liquid yields of 71 - 81 wt%, but also consistently produced 1.5 wt% coke. Additionally, Miskolczi reports that thermal degradation of PE above 450 - 460 °C results in higher rates of cyclization reactions, producing undesirable aromatics and coke.[141]

Autothermal catalytic oxidative pyrolysis of PS and PE may provide a method to produce high yields of liquid product with no char production. The millisecond processing times within the reactor and plug flow properties can yield smaller range of products. Adjusting inlet feed concentrations as well as C/O ratio can also adjust product selectivity.

6.2.2 Thermosets

The second class of plastics, thermosets, are polymers that form three dimensional molecular structures during manufacturing and cannot be softened when reheated, only decomposed. These polymers cannot be recycled by melting or extrusion processes without suffering extensive damage to polymer chains. Therefore, markets for recycled thermoset products are very limited and most are ground and rebonded using adhesives and pressure into low value products.

Millisecond autothermal catalytic oxidative pyrolysis could provide an efficient means to process solid thermoset materials into liquid products. Research has shown successful conversion of cellulose to clean, tar-free syngas in millisecond time scales over a Rh-Ce/γ-Al_2O_3.[36,45] Further research has shown that this conversion occurs through a reactive liquid intermediate at the front face of the catalyst (Fig. 6.9, reprinted from Chapter 2 for convenience).[96] On both a catalytic monolith (Fig. 6.9(a)) and flat surface (Fig. 6.9(b)) high heat transfer rates from the surface to the cellulose particle pyrolytically decomposed the solid into a reactive liquid intermediate, which then further decomposed into volatile species that out gassed quickly without tar formation and within 180 ms. Conversion of polyurethane and styrene-butadiene rubber by a similar process is proposed.

Polyurethane

Polyurethane (PU) is a polymer composed of organic groups bonded by urethanes (Fig. 6.10). By varying the R group structure, a wide range of polyurethanes can be created and used for a wide variety of applications including molded foams, car bumpers, rigid automotive interior parts, and home and refrigerator insulation.[30] As a thermoset, recycling options are limited. Generally, polyurethanes, especially foams, are recycled by mechanical shredding and rebonding into low value products. Ground waste PU can be added to virgin PU products, but the particles must be very small and in limited quantities to avoid seriously affecting product properties. Additionally, PU recycling operations are generally unprofitable due to the collection and product

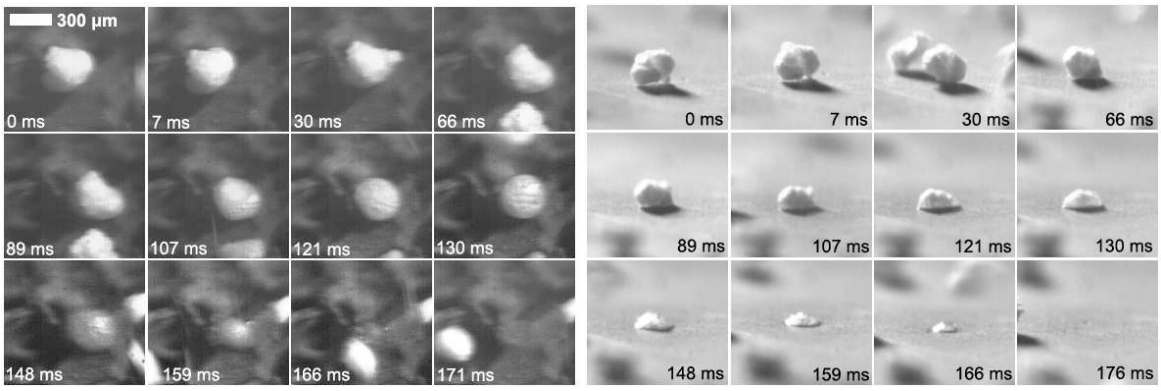

(a) (b)

Figure 6.9: Millisecond visualization of cellulose particle decomposition. (a) Microcrystalline cellulose particles ($\sim$ 300 μm) reacting to form volatile species in air on 700 °C Rh-Ce/γ-Al_2O_3 have been visualized with high-speed photography (1000 frames per second) on an 80 ppi α-Al_2O_3 foam support at C/O = 1.15 from a high angle. (b) A separate experiment examined cellulose decomposition on a smooth 700 °C Rh-Ce/γ-Al_2O_3 disk support at a very low angle. Particles exhibit poor surface contact (0 - 7 ms) before forming a liquid intermediate species capable of intimately contacting the catalytic surface (66 - 176 ms). The molten intermediate liquid appears to nucleate volatile species (107 - 130 ms) before completely converting without char formation (171 - 176 ms).[96]

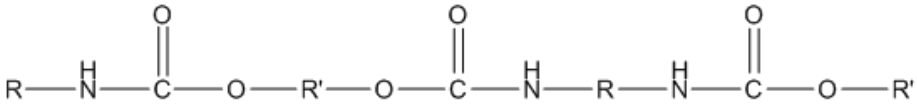

Figure 6.10: Structure of polyurethane. R is an organic group.

quality issues encountered by many plastic recycling efforts.

Previous PU pyrolysis research has shown that degradation begins at 250 °C, proposed to begin with the breaking of the urethane bond to produce CO_2.[143] Pyrolysis makes large amounts of gases, oils, and waxes, little solid char. Fluidized bed pyrolysis of PU at high temperatures (600 - 700 °C) has been shown to produce carbon oxides, methane, and ethane, as well as small amounts of hydrogen cyanide (H-C≡N). However, PU pyrolysis liquid product is generally of limited use as it is very viscous and unstable, solidifying over time due to the highly reactive diisocyanates (N=C=O) formed during pyrolysis.[147]

The presence of nitrogen and oxygen within the PU polymer chain can introduce a variety of products. Pyrolysis at the front face of the catalyst can produce the aforementioned species. Further reaction of these species within the catalyst bed

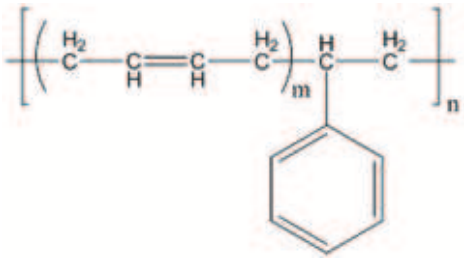

Figure 6.11: Structure of styrene-butadiene rubber.

may be able to react the isocyanate species.

Scrap Tires

Automotive tires are composed of styrene-butadiene rubber (SBR), synthetic or natural polyisoprene rubber, as well as steel, carbon black, and other additives.[140] Tires also contain $\sim$ 2 % sulfur, which is used to vulcanize rubber, creating crosslinked polymers with higher strength and desirable qualities.[30]

The use of recycled tire material in the production of new tires has significantly decreased in recent years due to increased liability concerns and use of synthetic rubbers.[30] In addition to mechanical grinding and rebonding recycling applications, devulcanization of tires can be used to "reverse" the vulcanization process and recover material. However, current devulcanization techniques generally degrade between 30 - 70 % of the polymer, severely affecting material properties.

Pyrolysis of whole tires has also been the focus of previous research. Pyrolysis of whole tires produces large amounts of carbon black due to its use an additive in original tire production. Liquid pyrolysis product, produced from the reactions of the rubber components, contains large amounts of benzene, toluene, and xylene, and is commonly referred to as BTX.[30] As pyrolysis temperatures increase, the concentration of aromatics in the liquid product increases, however total liquid product decreases in favor of gaseous products.[147] Benzene, toluene, and xylene are valuable products individually, however distillation of these aromatics is too difficult and expensive to justify and BTX is generally used as a co-feed to oil refineries. On a commercial scale, Goodyear developed a pyrolysis facility to process whole tires. The facility was unable to be profitable and eventually shut down because the pyrolysis oil product was of very low quality and could only be used as a crude oil blend component.[30]

The sulfur used to vulcanize rubber for use in tires can create small amounts of hydrogen sulfide gas during pyrolysis.[30] Generally, sulfur presents an experimental

concern due to its ability to poison catalysts. Sulfur has been shown to reversibly poison catalytic sites on Rh-Ce catalysts, decreasing feedstock conversion.[108] However, it may not be an issue in the proposed experimental system. The majority of solid degradation occurs at the catalyst front face, where extreme heat transfer rates pyrolyze the solid into volatile species, with little interaction with catalytic sites. Additionally, sulfur has been shown to increase catalyst temperature by decreasing the amount of endothermic steam reforming. Steam reforming is not advantageous to producing liquid products and this sulfur effect may actually be an advantage.

6.2.3 Experimental Methods

The experimental apparatus proposed for liquid production from solid plastic waste by millisecond autothermal catalytic oxidative pyrolysis will be similar to that in Figure 6.1. Mass flow controllers will be used to control nitrogen and oxygen feeds to a custom quartz reactor (Fig. 6.12). A custom hopper/auger will be used to control the flow of solid plastic particles (thermoplastics or thermosets) into the quartz tube and onto the catalyst front face, where they will be expected to pyrolyze into volatile species, which will then enter the catalyst bed and react.

The presented monoaromatic research (Chapter 3 demonstrated high selectivities to styrene and other condensible hydrocarbons at high C/O ratios as a model for lignin pyrolysis. These results may also provide insight to pyrolysis of PS and other aromatic-containing polymers. Operating the proposed catalytic system at high C/O ratios on a short catalytic bed could encourage the cracking of volatile species (evolved from decomposition of solid particles at the front face) to small, condensible hydrocarbons, while preventing complete decomposition into C_1 species. A Rh-Ce/γ-Al_2O_3 catalyst would be ideal for use at high C/O ratios due to its stability and coke resistance.

The oxidative pyrolysis products will be sampled directly below the back heat shield and analyzed via GC. To confirm the accuracy of carbon and other atom balances as well as the solid flow rate, a second catalyst will be placed downstream of the first bed and sampling port (Fig. 6.12). This second and longer catalytic bed would decompose the volatile effluent from the first catalyst into small and easily quantifiable species, allowing for accurate calculation of atom balances. Finally, effluent exiting the reactor after the second catalyst bed will be immediately incinerated to prevent soot and the release of toxic species.

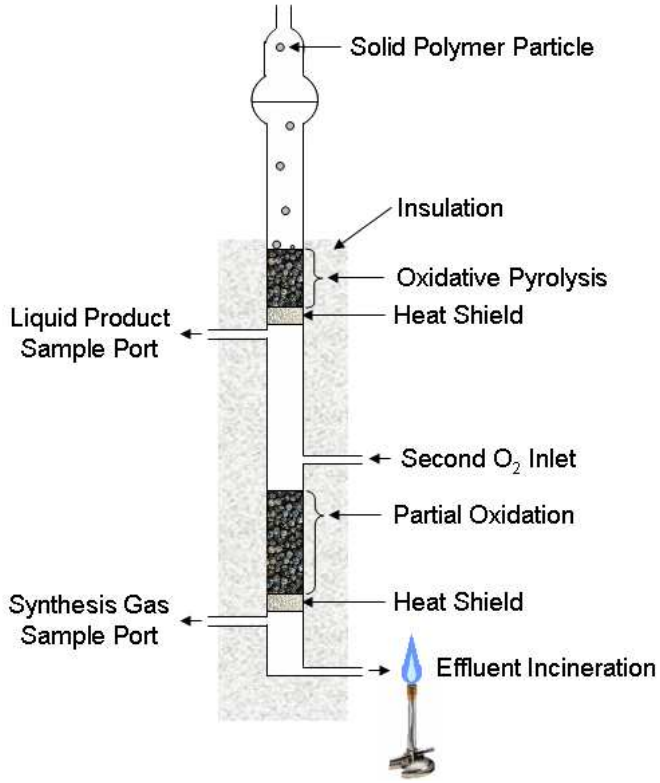

Figure 6.12: Selected reactor portion of the proposed oxidative pyrolysis apparatus. Refer to Figure 6.1 for pre-reactor externalities.

6.2.4 Preliminary Results

Preliminary results for pyrolysis of polyethylene have been obtained using a 1 cm, 65 ppi (pores per linear inch) Rh-Ce/γ-Al_2O_3 monolithic catalyst. These experiments were carried out in the same reactor system shown in Figure 6.1. Products were condensed after the catalyst and collected for characterization. Gas phase carbon products were sampled and analyzed by GC. All carbon species not quantified as CO, CO_2, or CH_4 are classified as pyrolysis products (Fig. 6.13). Very little ethylene was observed (< 1 %) The reactor is able to sustain autothermal and steady operation at much higher C/O ratios with a PE feed than with cellulose (Section 6.1.2). A C/O ratio of 3.4 resulted in a carbon selectivity of 90 % to pyrolysis products.

Pyrolysis products from PE were generally very soft waxes and light brown in color. Samples were dissolved in heptane and analyzed by GCMS. A sample chromatograph is shown in Figure 6.14. C_{12} to C_{30} species were easily identified by the MS. The straight chain monoenes of each species were the most abundant. Dienes and alkanes were also observed (Fig. 6.14, inset).

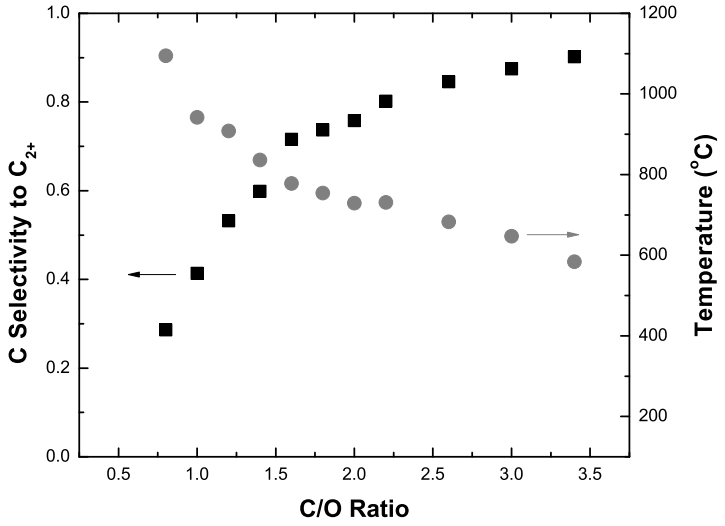

Figure 6.13: Oxidative pyrolysis of PE. Carbon selectivity to pyrolysis products, left axis. Catalyst back face temperature, right axis.

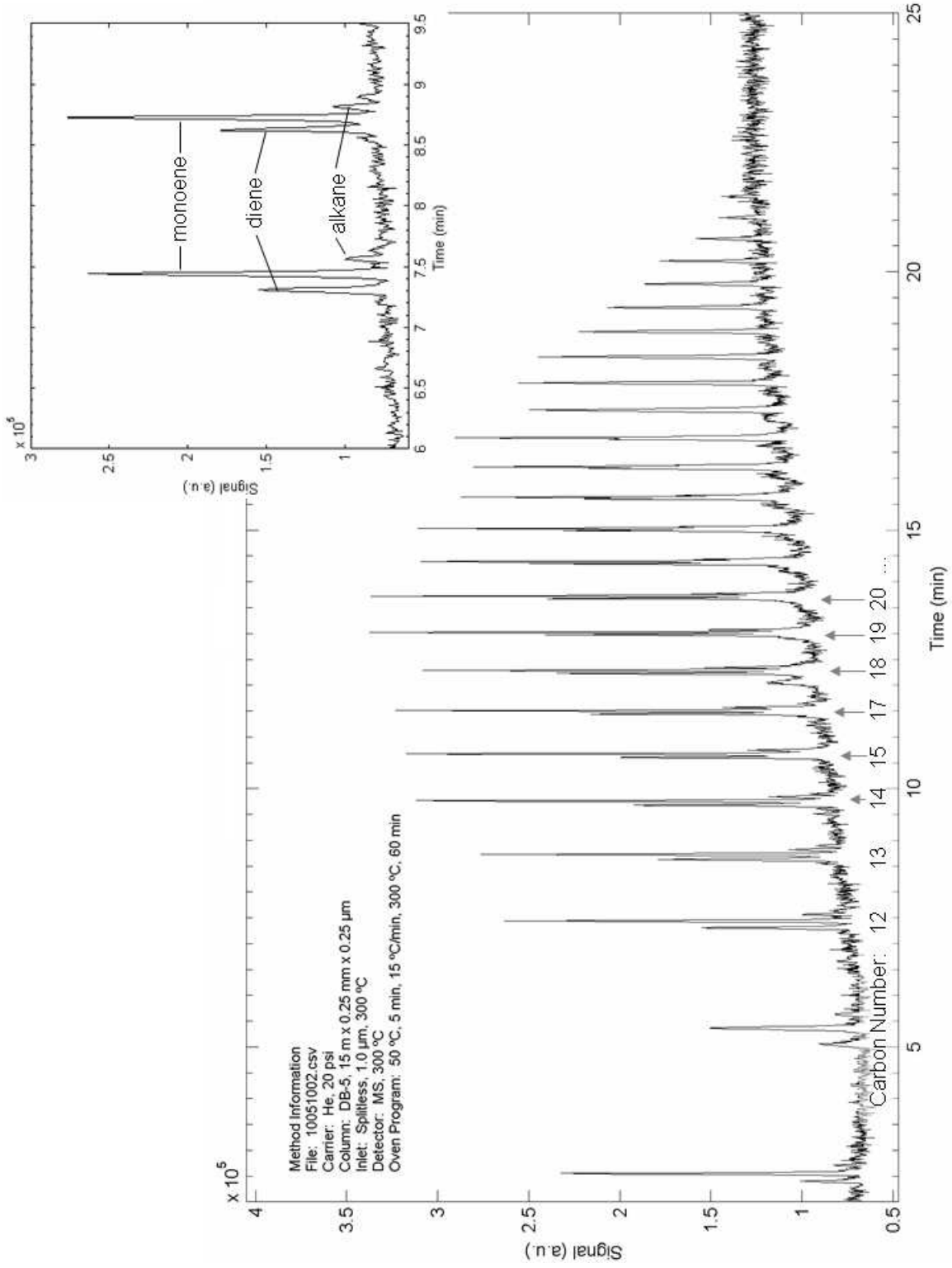

Figure 6.14: MS chromatograph of PE pyrolysis product.

Autothermal catalytic oxidative pyrolysis is proposed to convert biomass models and waste plastics into useful liquid products. The results presented in Chapters 3 to 5 demonstrate and give insight to the posibility of processing lignocellulosic biomass in such a reactor system. This processes may be able to provide a small-scale, efficient, and economical alternative to traditional processing methods. The preliminary results combined with the proposed work presented in Chapter 6 may provide valuable insight to the capabilities of catalytic oxidative pyrolysis in the future.

BIBLIOGRAPHY

[1] R. D. Perlack, L. L. Wright, A. F. Turhollow, R. L. Graham, B. J. Stokes, and D. C. Erbach. Biomass as feedstock for a bioenergy and bioproducts industry: the tecnical feasibility of a billion-ton annual supply. Technical report, US Department of Energy and Department of Agriculture, April 2005.

[2] Office of Transportation and Air Quality. EPA finalizes regulations for the national renewable fuel standard program for 2010 and beyond. Regulatory announcement, US Environmental Protection Agency, February 2010.

[3] US Environmental Protection Agency. Regulation of fuels and fuel additives: Chnages to renwable fuel standard program. Final rule, US Federal Register, March 2010.

[4] US Environmental Protection Agency. Regulation of fuels and fuel additives: 2011 renewable fuel standards. Federal register, rules and regulations, US Federal Register, December 2010.

[5] K. Rao, S. Chelikani, P. Relue, and S. Varanasi. *Biotechnology for fuels and chemicals: the twenty-ninth symposium*, Chapter: A novel technique that enables efficient conduct of simultaneous isomerization and fermentation (SIF) of xylose, pages 101–117. Humana Press, 2008.

[6] D. Takara, P. Shrestha, and S. K. Khanal. *Bioenergy and Biofuel from Biowastes and Biomass*, Chapter: Lignocellulosic Biomass Pretreatment, pages 172–200. ASCE Publications, 2010.

[7] Z. L. Liu, B. C. Saha, and P. J. Slininger. *Bioenergy*, Chapter: Lignocellulosic biomass conversion to ethanol by Saccharomyces, pages 17–36. ASM Press, 2008.

[8] S. R. A. Kersten, W. P. M. van Swaaij, L. Lefferts, and K. Seshan. *Catalysis for renewables: from feedstock to energy production*, Chapter: Options for catalysis in the thermochemical conversion of biomass into fuels, pages 119–145. Wiley-VCH, 2007.

[9] C. Heitner and D. Dimmel. *Lignin and Lignans: Advances in Chemistry*. CRC Press, 2009.

[10] C. Fu, J. R. Mielenz, X. Xiao, Y. Ge, C. Y. Hamilton, M. Rodriguez, F. Chen, M. Foston, A. Ragauskas, J. Bouton, R. A. Dixon, and Z.-Y. Wang. Genetic manipulation of lignin reduces recalcitrance and improves ethanol production from switchgrass. *Proceedings of the National Academy of Sciences of the US*, 108:3803–3808, 2010.

[11] B. S. Dien, G. Sarath, J. F. Pedersen, S. E. Sattler, H. Chen, D. L. Funnell-Harris, N. N. Nichols, and M. A. Cotta. Improved sugar conversion and ethanol yield for Forage Sorghum (Sorghum bicolor L. Moench) lines with reduced lignin contents. *Bioenergy Research*, 2:153–164, 2009.

[12] US Environmental Protection Agency. Partial grant of clean air act waiver application submitted by Growth Energy to increase the allowable ethanol content of gasoline to 15 percent; Decision of the administrator. Notice, US Federal Register, January 2011.

[13] US Department of Energy. Ethanol incentives and laws. Online, September 2010. URL: http://www.afdc.energy.gov.

[14] L. Reijnders and M. A. J. Huijbregts. *Biofuels for road transport: a seed to wheel perspective*. Springer, 2009.

[15] A.V. Bridgwater. Biomass fast pyrolysis. *Thermal Science*, 8:21–49, 2004.

[16] S. Czernik. Review of fast pyrolysis of biomass. Online, 2010. URL: www.nh.gov.

[17] A. V. Bridgwater. Review of fast pyrolysis of biomass and product upgrading. *Biomass and Bioenergy*, 2011.

[18] Dynamotive Energy Systems Corporation. Corporate history. Online, 2011. URL: www.dynamotive.com.

[19] Dynamotive Energy Systems Corporation. Fast pyrolysis. Online, 2011. URL: www.dynamotive.com.

[20] Dynamotive Energy Systems Corporation. Biooil plus. Online, 2011. URL: www.dynamotive.com.

[21] Ensyn. Multiple RTP facilities with commercial scale operations. Online, 2011. URL: www.ensyn.com.

[22] Wisconsin Biorefining Development Initiative. Biorefining process: Biomass gasification. www.wisbiorefine.org.

[23] J. T. Cobb. Survey of commercial biomass gasifiers. In *AIChE Annual Meeting*. AIChE, November 2007.

[24] J. Warzel. Fischer-Tropsch (FT) workshop for turbine engine applications, Oklahoma City, Oklahoma. 2006.

[25] H. Schulz. Short history and present trends of Fischer-Tropsch synthesis. *Applied Catalysis A: General*, 186:3–12, 1999.

[26] National Energy Technology Laboratory of the US Department of Energy. Fischer-Tropsch (FT) synthesis. Online, June 2011. URL: http://www.netl.doe.gov.

[27] E. van Steen and M. Claeys. Fischer-Tropsch catalysts for the biomass-to-liquid process. *Chemical Engineering & Technology*, 31:655–666, 2008.

[28] A. Bridgwater. *Progress in Thermochemical Biomass Conversion*. Wiley-Blackwell, 2008.

[29] T. G. Kreutz, E. D. Larson, G. Liu, and R. H. Williams. Fischer-tropsch fuels from coal and biomass. In *25th Annual International Pittsburgh Coal Conference*, September 2008.

[30] J. Scheirs, editor. *Polymer Recycling. Science, Technology and Applications*. John Wiley & Sons, 1998.

[31] Rentech. Product demonstration unit. Online, 2009. URL: http://www.rentechinc.com.

[32] R. Penning. New developments in synthetic fuels. In *CTL/GTL Conference 2010*, December 2009.

[33] Rentech. Fuels, 2009. URL: http://www.rentechinc.com.

[34] R. Ray and R. B. Thorpe. A comparison of gasification with pyrolysis for the recycling of plastic containing wastes. *International Journal of Chemical Reactor Engineering*, 5, 2007.

[35] J. Gaube and H. F. Klein. The promoter effect of alkali in Fischer-Tropsch iron and cobalt catalysts. *Applied Catalysis, A: General*, 350:126, 2008.

[36] P. J. Dauenhauer, B. J. Dreyer, N. J. Degenstein, and L. D. Schmidt. Millisecond reforming of solid biomass for sustainable fuels. *Angewandte Chemie*, 46: 5864–5867, 2007.

[37] D. A. Hickman, E. A. Haupfear, and L. D. Schmidt. Synthesis gas formation by direct oxidation of methane of Rh monoliths. *Catalysis Letters*, 17:223–237, 1993.

[38] P. M. Torniainen, X. Chu, and L. D. Schmidt. Comparison of monolith-supported metals for the direct oxidation of methane to syngas. *Journal of Catalysis*, 146:1–10, 1994.

[39] R. P. O'Connor, E. J. Klein, and L. D. Schmidt. High yields of synthesis gas by millisecond partial oxidation of higher hydrocarbons. *Catalysis Letters*, 70: 99–107, 2000.

[40] C. Wheeler, A. Jhalani, E. J. Klein, S. Tummala, and L. D. Schmidt. The water-gas-shift reaction at short contact times. *Journal of Catalysis*, 223:191–199, 2004.

[41] J. R. Salge, G. A. Deluga, and L. D. Schmidt. Catalytic partial oxidation of ethanol over noble metal catalysts. *Journal of Catalysis*, 235:69–78, 2005.

[42] N. J. Degenstein, R. Subramanian, and L. D. Schmidt. Partial oxidation of n-hexadecane at short contact times: Catalyst and washcoat loading and catalyst morphology. *Applied Catalysis, A: General*, 305:146–159, 2006.

[43] A. S. Bodke, S. S. Bharadwaj, and L. D. Schmidt. The effect of ceramic supports on partial oxidation of hydrocarbons over noble metal coated monoliths. *Journal of Catalysis*, 179:138–149, 1998.

[44] E. C. Wanat, B. Suman, and L. D. Schmidt. Partial oxidation of alcohols to produce hydrogen and chemicals in millisecond-contact time reactors. *Journal of Catalysis*, 235:18–27, 2005.

[45] J. L. Colby, P. J. Dauenhauer, and L. D. Schmidt. Millisecond autothermal steam reforming of cellulose for synthetic biofuels by reactive flash volatilization. *Green Chemistry*, 10:773–783, 2008.

[46] G. W. Huber, S. Iborra, and A. Corma. Synthesis of transportation fuels from biomass: Chemistry, catalysts, and engineering. *Chemical Reviews*, 106:4044–4098, 2006.

[47] In G. Huber, editor, *Breaking the Chemical and Engineering Barriers to Lignocellulosic Biofuels: Next Generation Hydrocarbon Biorefineries*. NSF, 2008.

[48] B. C. Gates, G. W. Huber, C. L. Marshall, P. N. Ross, J. Siirola, and Y. Wang. Catalysts for emerging energy applications. *MRS Bulletin*, 33:429–435, 2008.

[49] T. R. Carlson, T. P. Vispute, and G. W. Huber. Green gasoline by catalytic fast pyrolysis of solid biomass derived compounds. *ChemSusChem*, 1:397–400, 2008.

[50] G. Varhegyi, E. Jakab, and M. J. Antal Jr. Is the Broido-Shafizadeh model for cellulose pyrolysis true? *Energy & Fuels*, 8:1345–1352, 1994.

[51] J. Piskorz, P. Majerski, D. Radlein, A. Vladars-Usas, and D. S. Scott. Flash pyrolysis of cellulose for production of anhydro-oligomers. *Journal of Analytical and Applied Pyrolysis*, 56:145–166, 2000.

[52] J. Lede, J. P. Diebold, G. V. C. Peacocke, and J. Piskorz. *Deveopments in thermochemical biomass conversion*, Chapter: The nature and properties of intermediate and unvaporized biomass pyrolysis material, pages 27–42. Blackie Academic & Professional, 1997.

[53] C. DiBlasi. Modeling of chemical and physical processes of wood and biomass pyrolysis. *Progress in Energy and Combustion Science*, 34:47–90, 2008.

[54] A. G. W. Bradbury, Y. Sakai, and F. Shafizadeh. A kinetic model for pyrolysis of cellulose. *Journal of Applied Polymer Science*, 23:3271–3280, 1979.

[55] J. P. Diebold. A unified, global model for the pyrolysis of cellulose. *Biomass and Bioenergy*, 7:75–85, 1994.

[56] A. G. Liden, F. Berruti, and D. S. Scott. A kinetic model for the production of liquids from the flash pyrolysis of biomass. *Chemical Engineering Communications*, 65:207–221, 1988.

[57] J. Piskorz, D. Radlein, and D. S. Scott. On the mechanism of the rapid pyrolysis of cellulose. *Journal of Analytical and Applied Pyrolysis*, 9:121–137, 1986.

[58] J. Lede, H. Z. Li, and J. Villermaux. Fusion-like behavior of wood pyrolysis. *Journal of Analytical and Applied Pyrolysis*, 10:291–308, 1987.

[59] O. Boutin, M. Ferrer, and J. Lede. Radiant flash pyrolysis of cellulose – evidence for the formation of short-lifetime intermediate liquid species. *Journal of Analytical and Applied Pyrolysis*, 47:13–31, 1998.

[60] D. L. Pyle and C. A. Zaror. Heat transfer and kinetics in the low temperature pyrolysis of solids. *Chemical Engineering Science*, 39:147–158, 1984.

[61] C. DiBlasi. Kinetic and heat transfer control in the slow and flash pyrolysis of solids. *Industrial & Engineering Chemistry Research*, 35:37–46, 1996.

[62] A. M. C. Janse, R. W. J. Westerhout, and W. Prins. Modelling of flash pyrolysis of a single wood particle. *Chemical Engineering and Processing*, 39:239–252, 2000.

[63] A. M. Kanury. Combustion characteristics of biomass fuels. *Combustion Science and Technology*, 97:469–491, 1994.

[64] W. E. Ranz and W. R. Marshall. Evaporation from drops I. *Chemical Engineering Progress*, 48:141–146, 1952.

[65] I. Milosavljevic, V. Oja, and E. M. Suuberg. Thermal effects in cellulose pyrolysis: Relationship to char formation processes. *Industrial & Engineering Chemistry Research*, 35:653–662, 1996.

[66] S. Chandra and C. T. Avedisian. Observations of droplet impingement on a ceramic porous surface. *International Journal of Heat and Mass Transfer*, 35: 2377–2388, 1992.

[67] Y. M. Arifin, T. Furuhata, M. Saito, and M. Arai. Diesel and biodiesel fuel deposits on a hot surface. *Fuel*, 87:1601–1609, 2008.

[68] J. Lede, J. Panagopoulos, H. Z. Li, and J. Villermaux. Fast pyrolysis of wood: direct measurement and study of ablation rate. *Fuel*, 64:1514–1520, 1985.

[69] G. V. C. Peacocke and A. V. Bridgwater. Ablative plate pyrolysis of biomass for liquids. *Biomass and Bioenergy*, 7:147–154, 1994.

[70] C. DiBlasi. Heat transfer mechanisms and multi-step kinetics in the ablative pyrolysis of cellulose. *Chemical Engineering Science*, 51:2211–2220, 1996.

[71] C. DiBlasi. The state of the art of transport models for charring solid degradation. *Polymer International*, 49:1133–1146, 2000.

[72] R. S. Miller and J. Bellan. Numerical simulation of vortex pyrolysis reactors for condensable tar production from biomass. *Energy & Fuels*, 12:25–40, 1998.

[73] C. T. Brooks, S. J. Peacock, and B. G. Reuben. Pyrolysis of benzene. *Journal of the Chemical Society, Faraday Transactions 1: Physical Chemistry in Condensed Phases*, 75(3):652–62, 1979.

[74] M. U. Alzueta, P. Glarborg, and K. Dam-Johansen. Experimental and kinetic modeling study of the oxidation of benzene. *International Journal of Chemical Kinetics*, 32(8):498–522, 2000.

[75] I. Da Costa, R. Fournet, F. Billaud, and F. Battin-Leclerc. Experimental and modeling study of the oxidation of benzene. *International Journal of Chemical Kinetics*, 35(10):503–524, 2003.

[76] C. T. Brooks and S. J. Peacock. Pyrolysis of ethylbenzene. *Journal of the Chemical Society, Faraday Transactions 1: Physical Chemistry in Condensed Phases*, 78:3187–3202, 1982.

[77] K. K. Pant and D. Kunzru. Noncatalytic and catalytic pyrolysis of toluene. *The Canadian Journal of Chemical Engineering*, 77:150–155, 1999.

[78] A. Donazzi, B. C. Michael, and L. D. Schmidt. Chemical and geometric effects of Ce and washcoat addition on catalytic partial oxidation of CH_4 on Rh probed by spatially resolved measurements. *Journal of Catalysis*, 260:270–275, 2008.

[79] B. E. Koel. A high-resolution electron energy loss spectroscopy study of the surface structure of benzene adsorbed on the rhodium(111) crystal face. *Journal of Physical Chemistry*, 88:1988–1996, 1984.

[80] B. E. Koel. Thermal decomposition of benzene on the Rh(111) crystal surface. *Journal of Physical Chemistry*, 90:2949–2956, 1986.

[81] C. Minot and P. Gallezot. Competitive hydrogenation of benzene and toluene: Theoretical study of their adsorption on ruthenium, rhodium, and palladium. *Journal of Catalysis*, 123:341–348, 1990.

[82] M. E. Viste, K. D. Gibson, and S. J. Sibener. Heterogeneous combustion of benzene on Rh(111): Kinetics and dynamics of CO and CO_2 production. *Journal of Catalysis*, 191:237–244, 2000.

[83] T. Ioannides and X. E. Verykios. The interaction of benzene and toluene with Rh dispersed on SiO_2, Al_2O_3, and TiO_2 carriers. *Journal of Catalysis*, 143: 175–186, 1993.

[84] C. M. Friend and E. L. Muetterties. Coordination chemistry of metal surfaces. 3. Benzene and toluene interactions with nickel surfaces. *Journal of the American Chemical Society*, 103:773–779, 1981.

[85] M. J. Patterson, D. E. Angove, and N. W. Cant. The effect of carbon monoxide on the oxidation of four C_6 to C_8 hydrocarbons over platinum, palladium and rhodium. *Appl Catal B: Environ*, 26:47–57, 2000.

[86] M. J. Patterson, D. E. Angove, and N. W. Cant. The effect of metal order on the oxidation of a hydrocarbon mixture over alumina-supported combined platinum/rhodium catalysts. *Appl Catal B: Environ*, 35:53–58, 2001.

[87] S. B. Domke, R. F. Pogue, F. J. R. Van Neer, and C. M. Smith. Investigation of the kinetics of ethylbenzene pyrolysis using a temperature-scanning reactor. *Industrial & Engineering Chemistry Research*, 40:5878–5884, 2001.

[88] M.-C. Tsai and E. L. Muetterities. Coordination chemistry of benzene, toluene, cyclohexadienes, cyclohexene, and cyclohexane on Pt(100). *Journal of Physical Chemistry*, 86:5067–5071, 1982.

[89] D. Duprez, A. Miloudi, G. Delahay, and R. Maurel. Selective steam reforming of aromatic hydrocarbons. *Journal of Catalysis*, 101:56–66, 1986.

[90] P. J. Dauenhauer, J. R. Salge, and L. D. Schmidt. Renewable hydrogen by autothermal steam reforming of volatile carbohydrates. *Journal of Catalysis*, 244:238–247, 2006.

[91] D. Duprez. Selective steam reforming of aromatic compounds on metal catalysts. *Applied Catalysis A: General*, 82:111–157, 1992.

[92] H. Cordatos, T. Bunluesin, J. Stubenrauch, J. M. Vohs, and R. J. Gorte. Effect of ceria structure on oxygen migration for Rh/ceria catalysts. *Journal of Physical Chemistry*, 100:785–789, 1996.

[93] T. Zhu and M. Flytzani-Stephanopoulos. Catalytic partial oxidation of methane to synthesis gas over Ni-CeO_2. *Applied Catalysis A: General*, 208(1-2):403 – 417, 2001. ISSN 0926-860X.

[94] A. V. Bridgwater. Renewable fuels and chemicals by thermal processing of biomass. *Chemical Engineering Journal*, 91:87 – 102, 2003.

[95] A. V. Bridgwater, D. Meier, and D. Radlein. An overview of fast pyrolysis of biomass. *Organic Geochemistry*, 30:1479 – 1493, 1999.

[96] P. J. Dauenhauer, J. L. Colby, C. M. Balonek, W. J. Suszynski, and L. D. Schmidt. Reactive boiling of cellulose for integrated catalysis through an intermediate liquid. *Green Chemistry*, 11:1555–1561, 2009.

[97] R. G. Graham, L. K. Mok, M. A. Bergougnou, H. I. De Lasa, and B. A. Freel. Fast pyrolysis (ultrapyrolysis) of cellulose. *Journal of Analytical and Applied Pyrolysis*, 6:363–374, 1984.

[98] L. Wei, S. Xu, L. Zhang, H. Zhang, C. Liu, H. Zhu, and S. Liu. Characteristics of fast pyrolysis of biomass in a free fall reactor. *Fuel Processing Technology*, 87:863–871, 2006.

[99] C. M. Balonek, J. L. Colby, and L. D. Schmidt. Millisecond catalytic reforming of monoaromatics over noble metals. *AIChE Journal*, 56:979–988, 2010.

[100] C. K. Law and O. C. Kwon. Effects of hydrocarbon substitution on atmospheric hydrogen-air flame propagation. *International Journal of Hydrogen Energy*, 29: 867–879, 2004.

[101] B. C. Michael, A. Donazzi, and L. D. Schmidt. Effects of H_2O and CO_2 addition in catalytic partial oxidation of methane on Rh. *Journal of Catalysis*, 265:117–129, 2009.

[102] J. L. Colby. *Catalytic Autothermal Reforming of Biomass to Synthesis Gas*. PhD thesis, University of Minnesota, 2010.

[103] R. Horn, K. A. Williams, N. J. Degenstein, A. Bitsch-Larsen, D. Dalle Nogare, S. A. Tupy, and L. D. Schmidt. Methane catalytic partial oxidation on autothermal Rh and Pt foam catalysts: Oxidation and reforming zones, transport effects, and approach to thermodynamic equilibrium. *Journal of Catalysis*, 249: 380–393, 2007.

[104] G. J. Panuccio and L. D. Schmidt. Species and temperature profiles in a differential sphere bed reactor for the catalytic partial oxidation of n-octane. *Applied Catalysis, A: General*, 332:171–182, 2007.

[105] K. L. Hohn and L. D. Schmidt. Partial oxidation of methane to syngas at high space velocities over Rh-coated spheres. *Applied Catalysis, A: General*, 211: 53–68, 2001.

[106] G. A. Deluga, J. R. Salge, L. D. Schmidt, and X. E. Verykios. Renewable hydrogen from ethanol by autothermal reforming. *Science*, 303:993–997, 2004.

[107] J. Warnatz, M. D. Allendorf, R. J. Kee, and M. E. Coltrin. A model of elementary chemistry and fluid mechanics in the combustion of hydrogen on platinum surfaces. *Combustion and Flame*, 96:393–406, 1994.

[108] A. Bitsch-Larsen, N. J. Degenstein, and L. D. Schmidt. Effect of sulfur in catalytic partial oxidation of methane over Rh-Ce coated foam monoliths. *Applied Catalysis B: Environmental*, 78:364–370, 2008.

[109] R. P. O'Connor, E. J. Klein, D. Henning, and L. D. Schmidt. Tuning millisecond chemical reactors for the catalytic partial oxidation of cyclohexane. *Applied Catalysis, A: General*, 238:29–40, 2003.

[110] A. Donazzi, A. Beretta, G. Groppi, and P. Forzatti. Catalytic partial oxidation of methane over a 4% Rh/α-Al_2O_3 catalyst. *Journal of Catalysis*, 255:241–258, 2008.

[111] B. C. Michael, D. N. Nare, and L. D. Schmidt. Catalytic partial oxidation of ethane to ethylene and syngas over Rh and Pt coated monoliths: Spatial profiles of temperature and composition. *Chemical Engineering Science*, 65:3893–3902, 2010.

[112] D. Mohan, C. U. Pittman, and P. H. Steele. Pyrolysis of wood/biomass for bio-oil: A critical review. *Energy & Fuels*, 20:848–889, 2006.

[113] E. M. Hassan, P. H. Steele, and L. Ingram. Characterization of fast pyrolysis bio-oils produced from pretreated pine wood. *Applied Biochemistry and Biotechnology*, 154:182–192, 2009.

[114] S. Arvelakis and E. G. Koukios. Physicochemical upgrading of agroresidues as feedstocks for energy production via thermochemical conversion methods. *Biomass and Bioenergy*, 22:331, 2002.

[115] S. Xiong, J. Burvall, H. Orberg, G. Kalen, M. Thyrel, M. Ohman, and D. Bostrom. Slagging characteristics during combustion of corn stovers with and without kaolin and calcite. *Energy and Fuels*, 22:3465, 2008.

[116] L. Hoskinson, D. L. Karlen, S. J. Birrellc, C. W. Radtke, and W. W. Wilhelm. Engineering, nutrient removal, and feedstock conversion evaluations of four corn stover harvest scenarios. *Biomass and Bioenergy*, 31:126, 2007.

[117] E. A. Blekkan, A. Holmen, and S. Vada. Alumina-supported cobalt catalysts characterized by TPR, TPD and pulse chemisorption. *Acta Chemica Scandinavica*, 47:275, 1993.

[118] H. P. Bonzel, G. Broden, and H. J. Krebs. X-ray photoemission spectroscopy of potassium-promoted iron and platinum surfaces after hydrogen reduction and carbon monoxide-hydrogen reaction. *Applications of Surface Science*, 16:373, 1983.

[119] M. Trpanier, A. Tavasoli, A. K. Dalai, and N. Abatzoglou. Co, Ru and K loadings effects on the activity and selectivity of carbon nanotubes supported cobalt catalyst in Fischer-Tropsch synthesis. *Applied Catalysis, A: General*, 353:193, 2009.

[120] O. Borg, N. Hammer, S. Eri, O. A. Lindvaag, R. Myrstad, E. A. Blekkan, M. Roenning, E. Rytter, and A. Holmen. Fischer-Tropsch synthesis over unpromoted and Re-promoted γ-Al_2O_3 supported cobalt catalysts with different pore sizes. *Catalysis Today*, 142:1, 2009.

[121] R. R. Baker and H. W. Elbersen. 14^{th} European Biomass Conference and Exhibition. 2005.

[122] H. Mansilla, R. Garcia, J. Tapia, H. Duran, and S. Urzua. Chemical characterization of chilean hardwoods. *Wood Science and Technology*, 25:145, 1991.

[123] X. L. Zhou and J. M. White. Stabilization by potassium of adsorbed hydrogen on platinum(111). *Surface Science*, 185:450, 1987.

[124] W.-P. Ma, Y.-J. Ding, and L.-W. Lin. Fischer-Tropsch synthesis over activated-carbon-supported cobalt catalysts: Effect of Co loading and promoters on catalyst performance. *Industrial & Engineering Chemistry Research*, 43:2391, 2004.

[125] F. Solymosi and I. Kovacs. Effects of potassium adlayer on the adsorption and desorption of hydrogen on a palladium(100) surface. *Journal of Physical Chemistry*, 93:7537, 1989.

[126] H. P. Bonzel and H. J. Krebs. Enhanced rate of carbon deposition during Fischer-Tropsch synthesis on potassium-promoted iron. *Surface Science*, 109: L527, 1981.

[127] I. Rodriguez-Ramos, A. Guerrero-Ruiz, J. L. G. Fierro, P. R. de la Piscina, and N. Homs. Carbon monoxide hydrogenation over potassium-promoted iron, cobalt and nickel catalysts prepared from cyanide complexes. *Zeitschrift fuer Anorganische und Allgemeine Chemie*, 582:197, 1990.

[128] J. K. Brown, A. C. Luntz, and P. A. Schultz. Long-range poisoning of molecular deuterium dissociative chemisorption on platinum(111) by coadsorbed potassium. *Journal of Chemical Physics*, 95:3767, 1991.

[129] D. A. Wesner, G. Linden, and H. P. Bonzel. Alkali promotion on cobalt: surface analysis of the effects of potassium on carbon monoxide adsorption and Fischer-Tropsch reaction. *Applied Surface Science*, 26:335, 1986.

[130] G. Ertl, S. B. Lee, and M. Weiss. The influence of potassium on the adsorption of hydrogen on iron. *Surface Science*, 111:L711, 1981.

[131] N. D. Lang, S. Holloway, and J. K. Norskov. Electrostatic adsorbate-adsorbate interactions: the poisoning and promotion of the molecular adsorption reaction. *Surface Science*, 150:24, 1985.

[132] S. Yaman. Pyrolysis of biomass to produce fuels and chemical feedstocks. *Energy Conversion and Management*, 45:651–671, 2004.

[133] A. Shihadeh and S. Hochgreb. Diesel engine combustion of biomass pyrolysis oils. *Energy & Fuels*, 14:260–274, 2000.

[134] S. Czernik and A. V. Bridgwater. Overview of applications of biomass fast pyrolysis oil. *Energy & Fuels*, 18:590–598, 2004.

[135] R. K. Kaila, A. Gutierrez, S.T. Korhonen, and A.O.I. Krause. Autothermal reforming of n-dodecane, toluene, and their mixture on mono- and bimetallic noble metal zirconia catalysts. *Catalysis Letters*, 115(1-2):70–78, May 2007.

[136] C. Jeyabharathi, P. Venkateshkumar, J. Mathiyarasu, and K.L.N. Phani. Platinum-tin bimetallic nanoparticles for methanol tolerant oxygen-reduction activity. *Electrochimica Acta*, 54:448–454, 2008.

[137] E. W. Dean and D. D. Stark. A convenient method for the determination of water in petroleum and other organic emulsions. *The Journal of Industrial and Engineering Chemistry*, 12:486–490, 1920.

[138] Academie Reims. Principaux montages de chimie. Online, June 2011. URL: http://www.ac-reims.fr.

[139] Z. Wang and S. A. Stout. *Oil spill environmental forensics: fingerprinting and source identification.* Academic Press, 2007.

[140] A. Buekens. *Feedstock Recycling and Pyrolysis of Waste Plastics: Converting Waste Plastics into Diesel and Other Fuels*, Chapter: Introduction to Feedstock Recycling of Plastics, pages 3–41. John Wiley & Sons, 2006.

[141] N. Miskolczi. *Feedstock Recycling and Pyrolysis of Waste Plastics: Converting Waste Plastics into Diesel and Other Fuels*, Chapter: Kinetic Model of the Chemical and Catalytic Recycling of Waste Polyethylene into Fuels, pages 225–247. John Wiley & Sons, 2006.

[142] C. G. Jung and A. Fontana. *Feedstock Recycling and Pyrolysis of Waste Plastics: Converting Waste Plastics into Diesel and Other Fuels*, Chapter: Production of Gaseous and Liquid Fuels by Pyrolysis and Gasification of Plastics: Technological Approach, pages 251–283. John Wiley & Sons, 2006.

[143] P. T. Williams. *Feedstock Recycling and Pyrolysis of Waste Plastics: Converting Waste Plastics into Diesel and Other Fuels*, Chapter: Yield and Composition of Gases and Oils/Waxes from the Feedstock Recycling of Waste Plastic, pages 285–313. John Wiley & Sons, 2006.

[144] E. A. Williams and P. T. Williams. The pyrolysis of individual plastics and a plastic mixture in a fixed bed reactor. *Journal of Chemical Technology & Biotechnology*, 70(1):9–20, 1997.

[145] P. T. Williams and R. Bagri. Hydrocarbon gases and oils from the recycling of polystyrene waste by catalytic pyrolysis. *International Journal of Energy Research*, 28(1):31–44, 2004.

[146] K.-H. Lee. *Feedstock Recycling and Pyrolysis of Waste Plastics: Converting Waste Plastics into Diesel and Other Fuels*, Chapter: Thermal and Catalytic Degradation of Waste HDPE, pages 129–160. John Wiley & Sons, 2006.

[147] M. Blazso. *Feedstock Recycling and Pyrolysis of Waste Plastics: Converting Waste Plastics into Diesel and Other Fuels*, Chapter: Composition of Liquid Fuels Derived from the Pyrolysis of Plastics, pages 315–344. John Wiley & Sons, 2006.

APPENDIX

A

SUPPLEMENTARY INFORMATION: REACTIVE BOILING OF CELLULOSE FOR INTEGRATED CATALYSIS THROUGH A LIQUID INTERMEDIATE[1]

A.1 Method for Small Cellulose Particles on Catalytic Foams

Visualization of microcrystalline cellulose particles on a 80 ppi α-Al_2O_3 foam coated with Rh-Ce (2.5 wt% each) occurred in a 20 mm I.D. quartz reactor tube shown in Figure A.1. Three foams (10 mm high, 18 mm wide) were stacked on top of each other with a fourth blank 80 ppi foam on the bottom, wrapped in ceramic paper (for friction fit), and slid into the reactor tube. A type K thermocouple was inserted 10 mm from the leading surface. A 1 cm pyrex tube combined with a size 20 pyrex reactor tube end cap provided the connection between the reactor and a cellulose hopper necessary for solid particle delivery. A quartz light pipe was inserted through the end cap and contacted the leading surface providing a light sample to an optical pyrometer. The cellulose particles (avg. 315 μm) stored in an acrylic tube hopper ($\sim$ 10 cm diameter) were pushed into a feed tube (0.25 inch I.D.) using a 0.25 inch wood auger driven in reverse with a servo motor permitting variable feed rates. Air was supplied by a gas cylinder and metered by a flow control valve calibrated with a bubble column.

The reactor in Figure A.1 was wrapped in a resistive heater controlled by a variac and wrapped in insulation. Autothermal operation was initiated by heating the re-

[1]Portions of this chapter appear in P.J. Dauenhauer, J.L. Colby, C.M. Balonek, W.J. Suszynski, L.D. Schmidt, "Rapid ablative pyrolysis of cellulose in an autothermal fixed-bed catalytic reactor," *Green Chemistry* **11** (2009) 1555-1561.

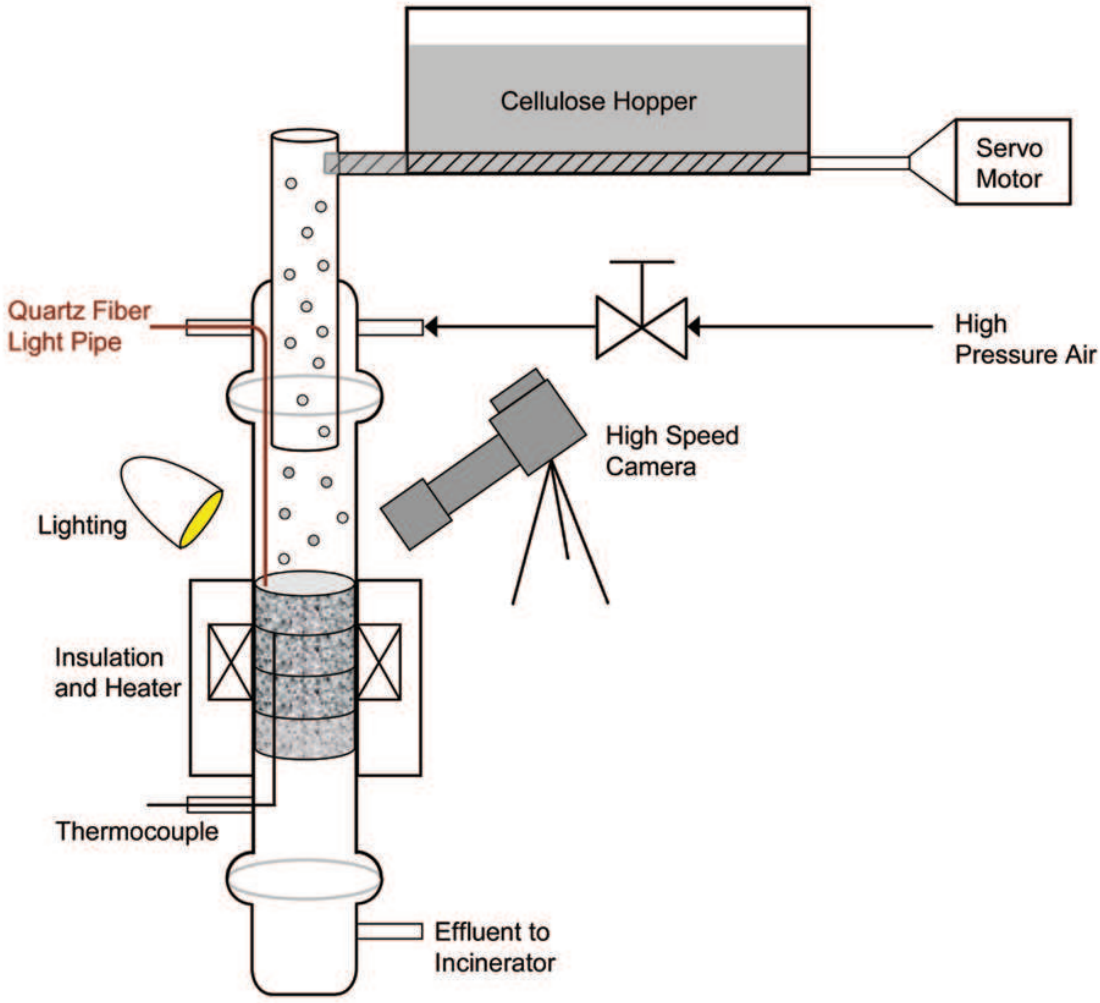

Figure A.1: Cellulose particle conversion was studied on RhCe-coated alumina foams in air in a visibly transparent 20 mm I.D. quartz tube surrounded by a resistive heater wrapped in ceramic insulation. Particles were delivered to the surface using an acrylic tube hopper through which passed a 0.25 inch wood auger operating in reverse. Cellulose flow rate was set by controlling the rotational speed of the wood auger with a servo motor. Air was supplied with a high pressure gas cylinder and metered using a gas-flow needle valve. A thermocouple was inserted into the catalytic bed 10 mm below the leading surface. A quartz fiber light pipe was inserted through the feed end-cap and impinged on the leading catalytic surface perpendicularly. Effluent was sent to an incinerator.

actor externally with air flow to $\sim$ 400 °C, at which point particles were delivered to the surface. Steady operation was obtained within $\sim$ 5 minutes, and the heater was turned off. Varying surface temperatures were obtained by varying the air flow rate or cellulose flow rate.

Digital video was obtained by focusing a Photron Fastcam Ultima APX with color image through the curved quartz reactor. The four optical lenses placed in series to obtain the presented magnification were: 1) a Micro-NIKKOR 105 mm lens by Nikon of Japan, 2) a Nikon PN-11 extension tube by Nikon of Japan, 3) a Kenko extension tube for Nikon/AF 36 mm by Kenko of Japan, and 4) a Kenko 2x Teleplus MC7 telephoto extension tube by Kenko of Japan. Light was provided to the catalyst necessary for high speed imaging by a Solarc Light LB-50 by Welch Allyn, Inc. of New York, U.S.A.

Additional videos are shown as Figures A.2 and A.3, and Figure 2.1(a) from Chapter 2 is repeated as Figure A.4. Figure A.2 shows the behavior of two particles impacting and coming to rest near each other on a the catalytic foam within $\sim$ 20 ms. After converting to an intermediate liquid, the two particles combine in about 3 ms to form a larger liquid particle which ultimately volatilizes at $\sim$ 180 ms. Gaseous evolution is clearly visible from 100 137 ms. The frames illustrate the particles tendency to form spherical liquid droplets. White streaks in frames 100 and 123 ms are small particles passing through the frame before contacting the surface and volatilizing. Figure A.3 shows a lone, irregularly shaped particle coming to rest on an alumina strut, converting to a liquid, and volatilizing to gases in $\sim$ 123 milliseconds. The particle forms an intermediate liquid overhanging the narrower strut, but surface tension pulls the liquid into a more spherical conformation.

A.2 Method for Small Particle Cellulose Feedstock

Microcrystalline cellulose obtained from FMC biopolymer (Lattice NT-200) was sieved to average size $\sim$ 315 μm. As shown in Figure A.5, the particles are not perfectly spherical, but rather have an aspect ratio (defined as length/width) of 1.39 ± 0.05 (95 % confidence interval) when considering only particles large enough for examination with high speed photography ($>$ 20 μm). Examination of cellulose particles by light scattering reveals in the size distribution (vol %) that most of the mass of the cellulose exists as large particles ($>$ 200 μm). However, most of the particles are small ($\sim$ 1 μm). Figure A.6 includes scanning electron micrographs of microcrystalline particles coated in Pt. The particles clearly exhibit high porosity with large void spaces (10 -

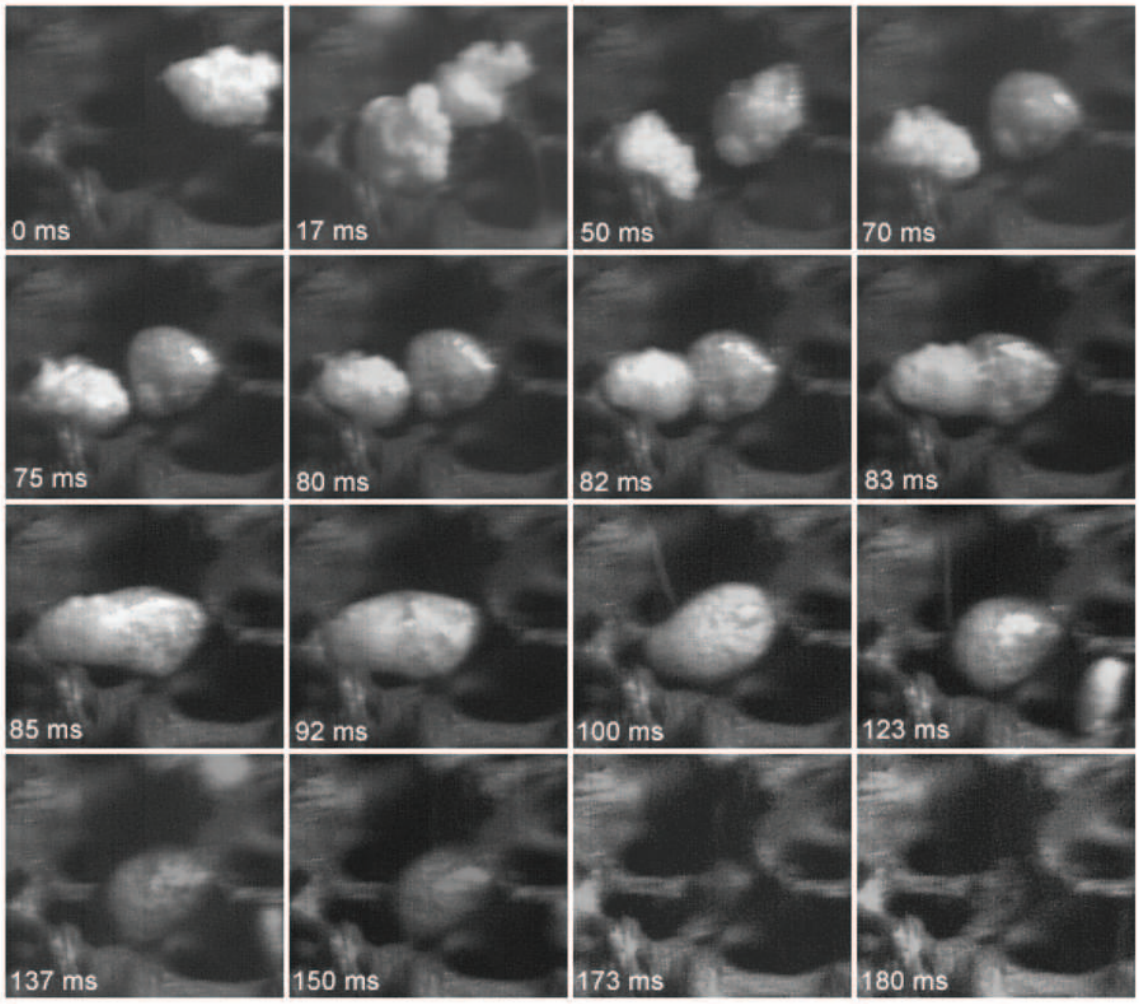

Figure A.2: Microcrystalline cellulose particles ($\sim 300\ \mu$m) reacting to volatile species in air on a 700 °C Rh-Ce/α-Al_2O_3 surface have been visualized with high-speed photography on an 80 ppi Al_2O_3 foam support at C/O = 1.15 at 45° from the surface normal with temporal resolution of one millisecond. Two particles (impacting at 0 and 17 ms) convert to a liquid and combine (82 - 85 ms) to a single particle which reactively volatilizes completely (180 ms).

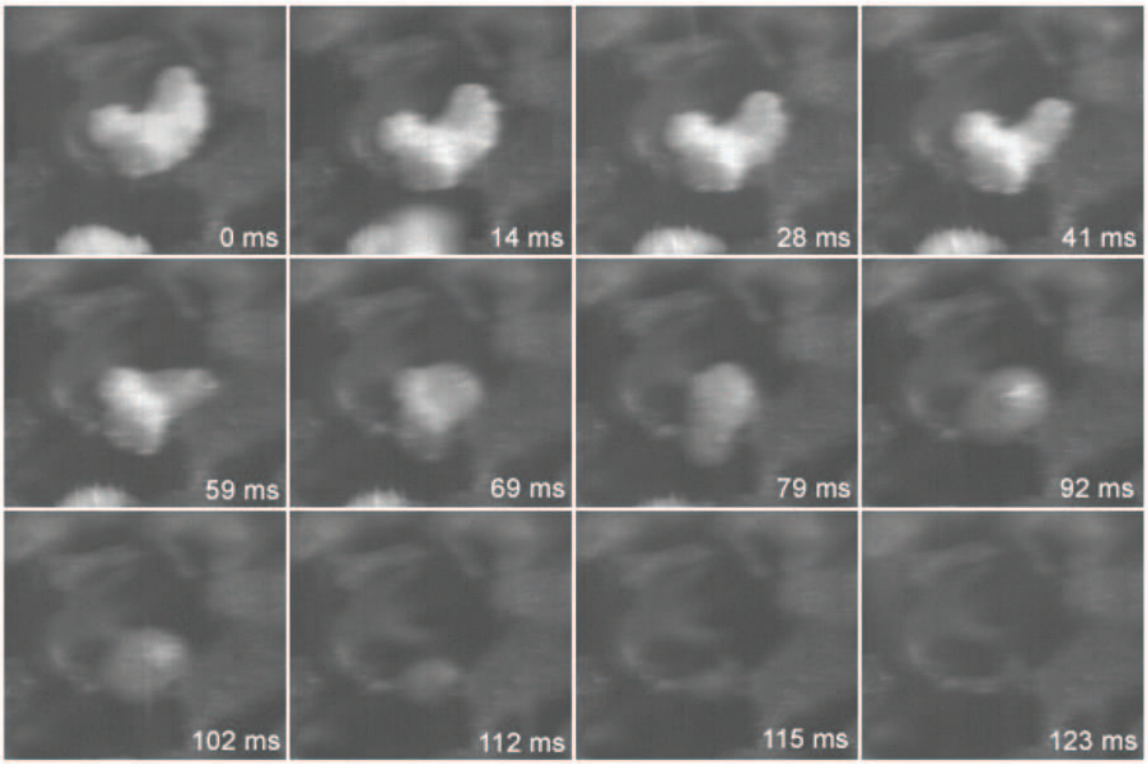

Figure A.3: Conversion of $\sim$ 300 μm microcrystalline cellulose particle to volatile species on a 700 °C RhCe/α-Al_2O_3 surface. Cellulose passes through a molten intermediate state before volatilizing completely.

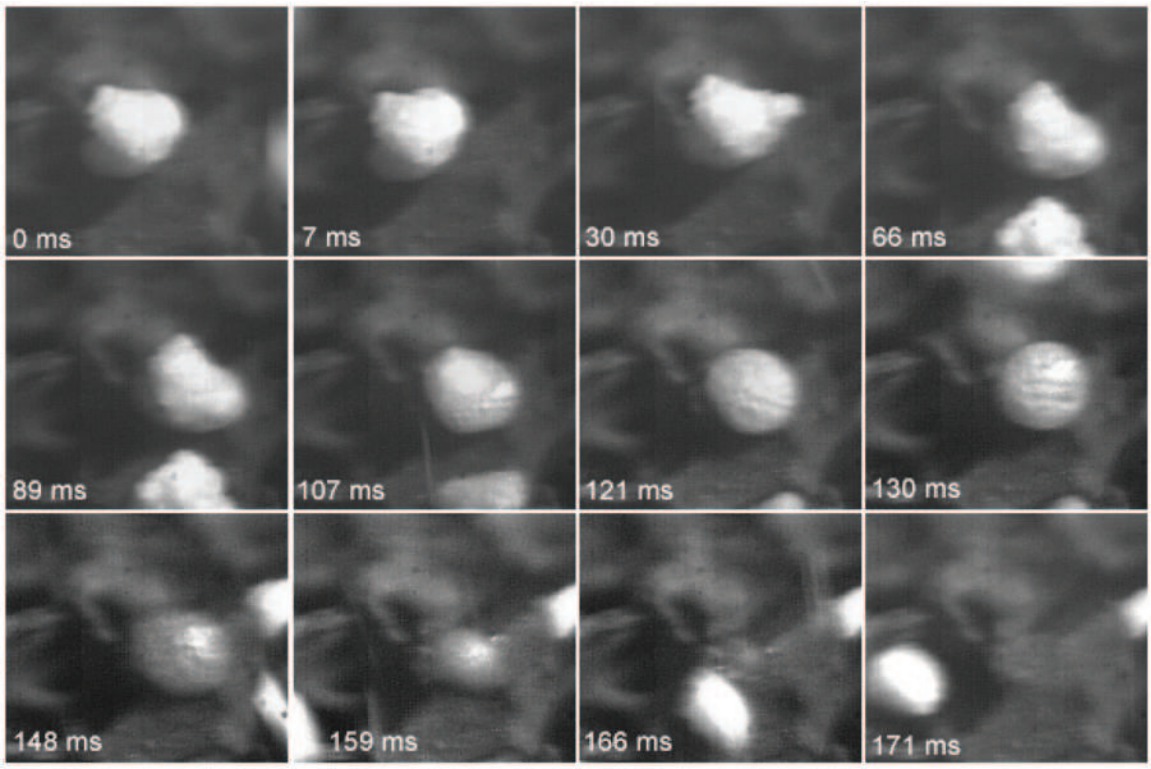

Figure A.4: Conversion of $\sim$ 300 μm microcrystalline cellulose particle to volatile species on a 700 °C RhCe/α-Al_2O_3 surface. Cellulose passes through a molten intermediate state before volatilizing completely.

40 microns) within the particle.

A.3 Method for Small Particle Conversion on Catalytic Foams

Three video files with $T_{surface}$ = 700, 825, and 900 °C were obtained by varying the cellulose and air flow rates as listed in Figure A.7. At each of the listed conditions, approximately 50 particles were tracked from resting impact (not moving on the surface) to the point in time when no visual trace of the particle was evident. At each of the three conditions, the total conversion time was directly proportional to the square of the initial particle radius (measured at the point of resting impact). The difference between the measured conversion times and a linear fit appears to increase with increasing particle dimensions. As shown in the first three panels of Figure A.7, the proportionality constant decreased with increasing surface temperature. In other words, a hotter surface resulted in faster heat transfer approximately consistent with $q_{conduction}$=$h_{surface}(\Delta T)$. The fourth panel shows a frame of video captured through the reactor wall. The thermocouple is clearly visible in the upper left corner for size comparison ($\sim$ 300 μm). The limitation of the depth of field of the camera only permits the measurement of particles that fall on the foam located in the center of the video frame.

Particles landing on struts of the catalytic foam within the depth of field of the camera were clearly visible and measurable during their conversion lifetime as shown in Figure 2.1. The width of four additional particles of varying size are included in Figure A.8 to show that the behavior of the particle in Figure 2.1 was representative of other particles. All observable particles exhibited nearly constant (or only slightly decreasing) width for most of their lifetime through the conversion from solid to liquid. Near the end of the particle conversion, fast linear decrease in particle width was observed.

A.4 Method for Small Particle Conversion on Catalytic Flat Surfaces

Particles of cellulose and sucrose pyrolyzing on a flat catalytic wafer (Rh-Ce/α-Al_2O_3, 2.5 wt% each) were also recorded using a high speed camera using the experimental setup depicted in Figure A.9. A quartz reactor was held in place 1 - 2 cm above the

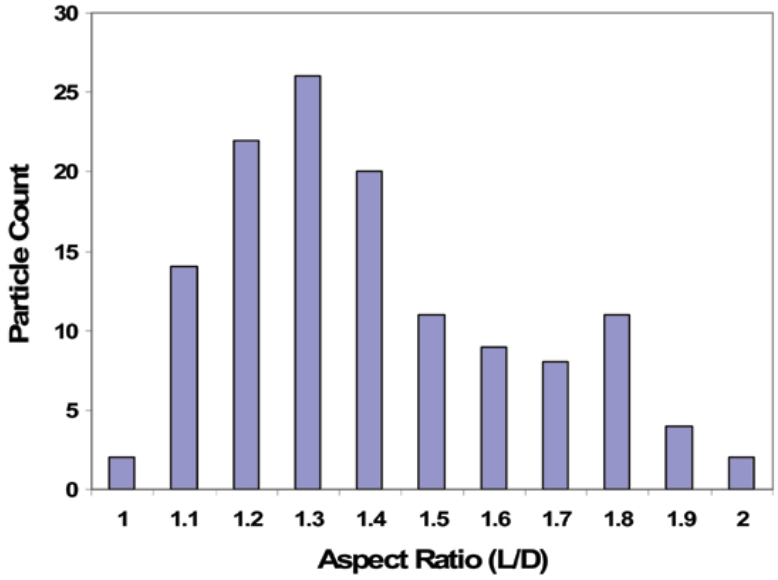

(a)

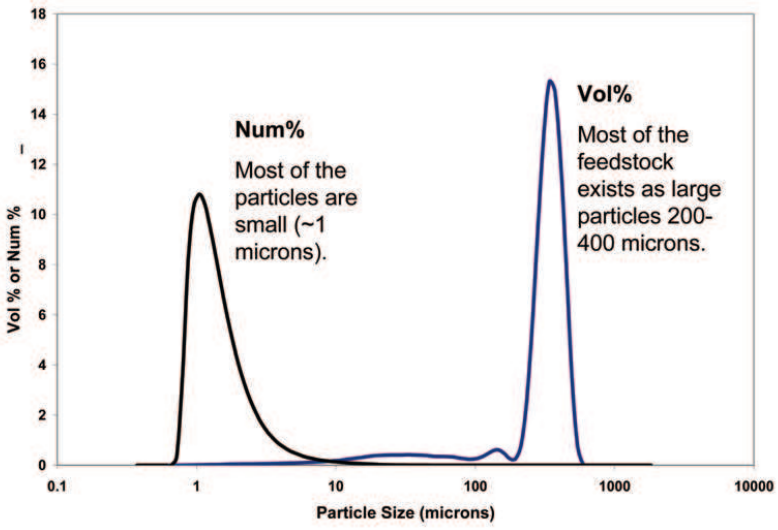

(b)

Figure A.5: (a) Particles of microcrystalline cellulose exhibited a distribution of aspect ratios defined as length/width with average aspect ratio 1.39 $\pm$ 0.05. (b) Sieved microcrystalline cellulose considered in the small particle experiments exists mostly as $\sim$ 300 μm particles, but most of the particles are small ($\sim$ 1 μm). Particle size distributions were collected by light scattering.

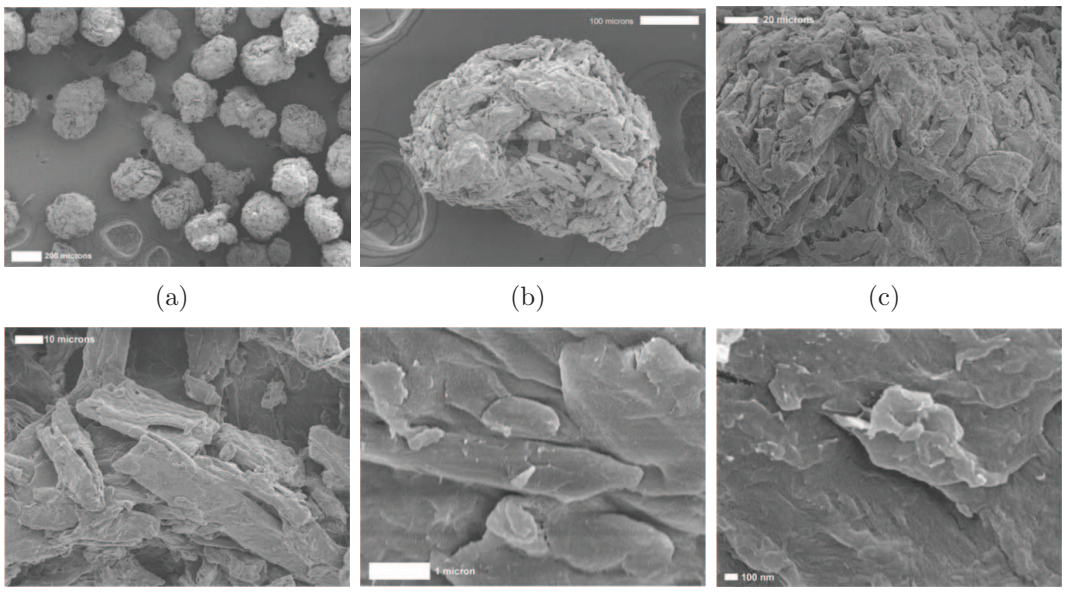

(a) (b) (c)

(d) (e) (f)

Figure A.6: Microcrystalline cellulose particles sieved to 300 μm average particle size (by volume) are shown in Panels (a), (b). Particles exist as porous structures of crystalline cellulose rods 1 - 20 microns in width (Panels (c), (d)). The surface of a crystalline micro-rod (Panels (e), (f)).

catalytic wafer by metal clamps. Air was supplied by a high pressure gas cylinder through a needle valve, and particles of solid material were supplied from a side tube sealed with a pushrod. A quartz fiber light pipe delivering light to an optical pyrometer was attached through the quartz reactor such that it contacted the catalytic surface. A butane torch was clamped directly below the catalytic wafer such that its distance was adjustable to control the surface temperature. The high speed camera was placed at a low angle relative to the flat surface (~ 10 °) obtaining light through a flat pyrex protector plate. Light was provided from behind the particles.

Figures A.10 and A.11 depict the conversion of two very different shaped cellulose particles at 700 °C. Both particles generate a liquid layer in contact with the surface followed by gas evolution as small bubbles. The liquid layer progresses up the particle finally generating a fully liquid droplet. The liquid droplet, hemispherical in shape, decreases rapidly in size leaving a clean surface behind.

Calculations in Figure 2.2 were completed with the following measurements in Figure A.12. The height (x) and width (2y) were measured directly from the video frames by relating the number of pixels to objects of known dimension such as the optical fiber. The radius of curvature, R_C, defining the shape of the liquid droplet

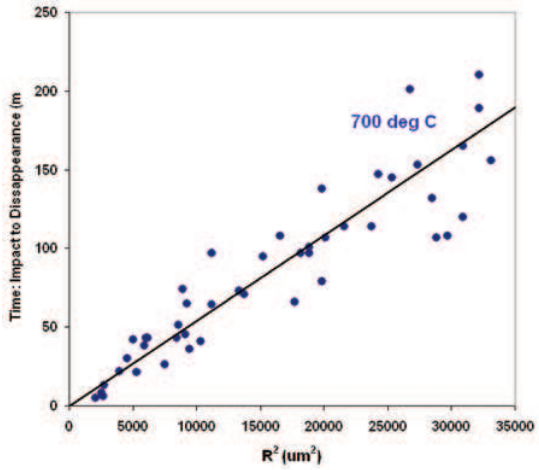

(a)

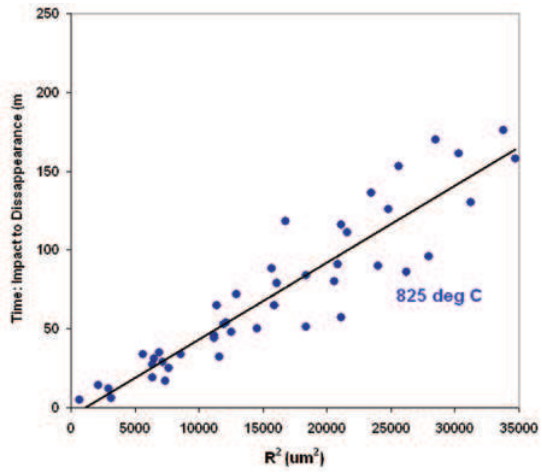

(b)

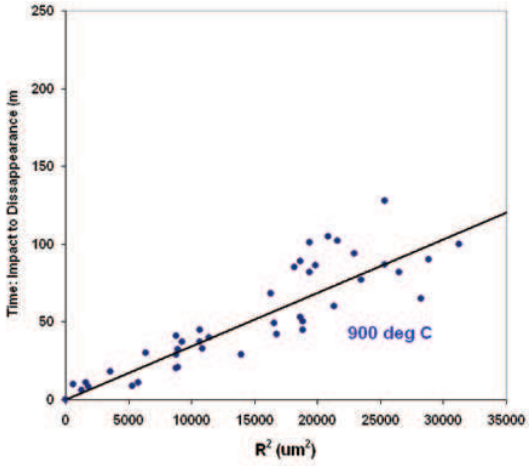

(c)

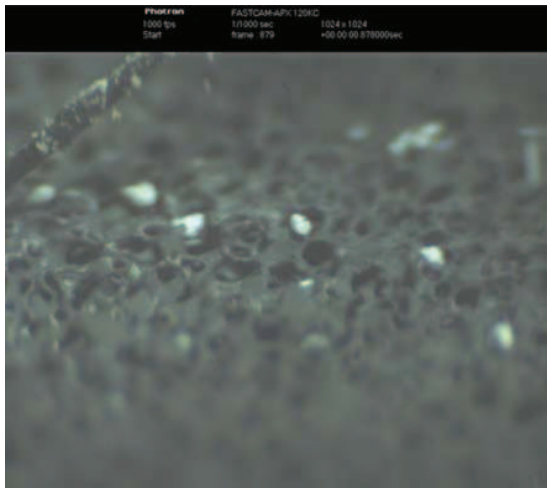

(d)

Experiment	A	B	C
Support	Foam	Foam	Foam
Catalyst	Rh-Ce	Rh-Ce	Rh-Ce
Surface T / °C	700	825	900
Air Flow / SLPM	1.52	2.21	1.98
Cellulose Flow / g hr^{-1}	53.1	37.2	30.6
N_2/O_2 Ratio	3.76	3.76	3.76
C/O Ratio	1.15	0.55	0.51

(e)

Figure A.7: The conversion of microcrystalline cellulose particles on Rh-Ce/α-Al_2O_3 foam supports (80 ppi) exhibited conversion time in milliseconds (impact to disappearance) linearly dependent on the square of the particle radius. Panel (a) is the data shown in Figure 2.2(a) with a different independent axis. Hotter surfaces decreased conversion time by increasing heat transfer rates to the particle (Panels (b), (c)). Panel (d) shows a frame captured by high-speed photography for the conversion of particles with a 700 °C surface (thermocouple in the top-left corner is 300 μm in width). Experimental conditions for the three sets of data in Panels (a), (b), and (c) are located in the table.

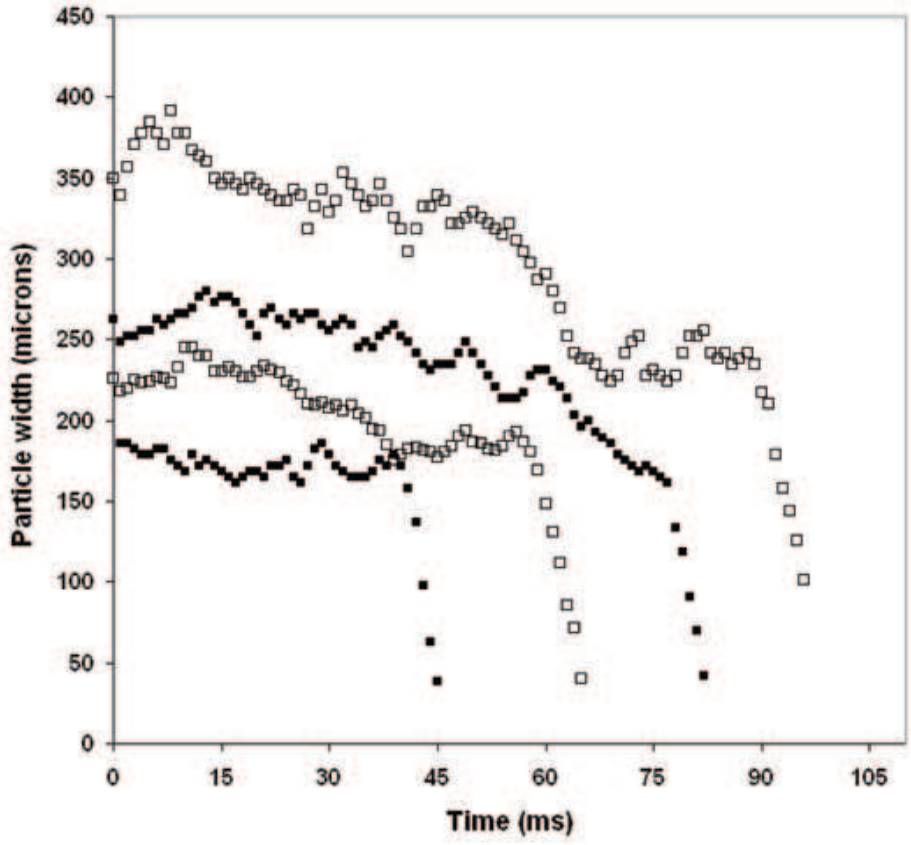

Figure A.8: The conversion multiple microcrystalline cellulose particles on Rh-Ce/α-Al_2O_3 foam supports (80 ppi) on a 700 °C surface exhibited a constant particle diameter (width measured parallel to surface) before rapid, linear decrease.

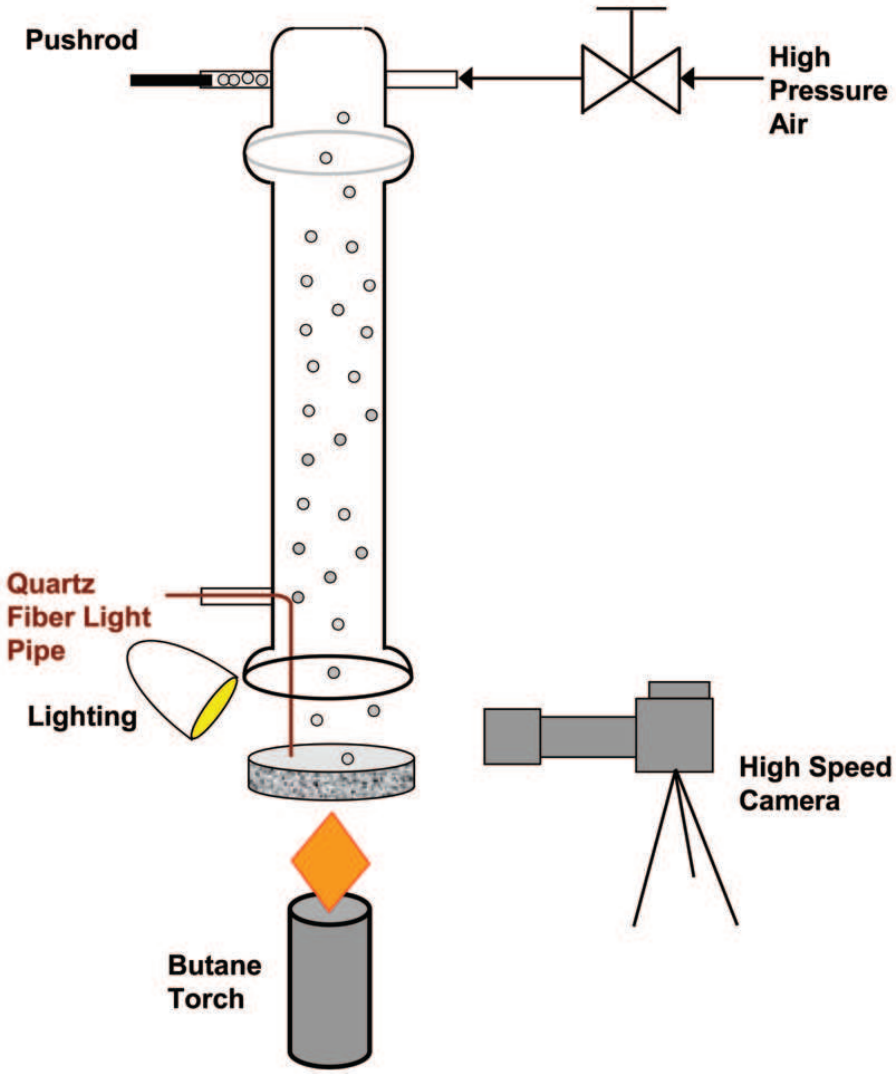

Figure A.9: Cellulose particle conversion was studied on RhCe-coated alumina wafer in air heated from below by a butane torch. Particles were fed to the surface by addition to the side of the reactor by a sealed push rod. Air was supplied by a compressed cylinder through a needle valve to control the flow. A quartz fiber light pipe was inserted through a side arm and impinged on the leading catalytic surface perpendicularly.

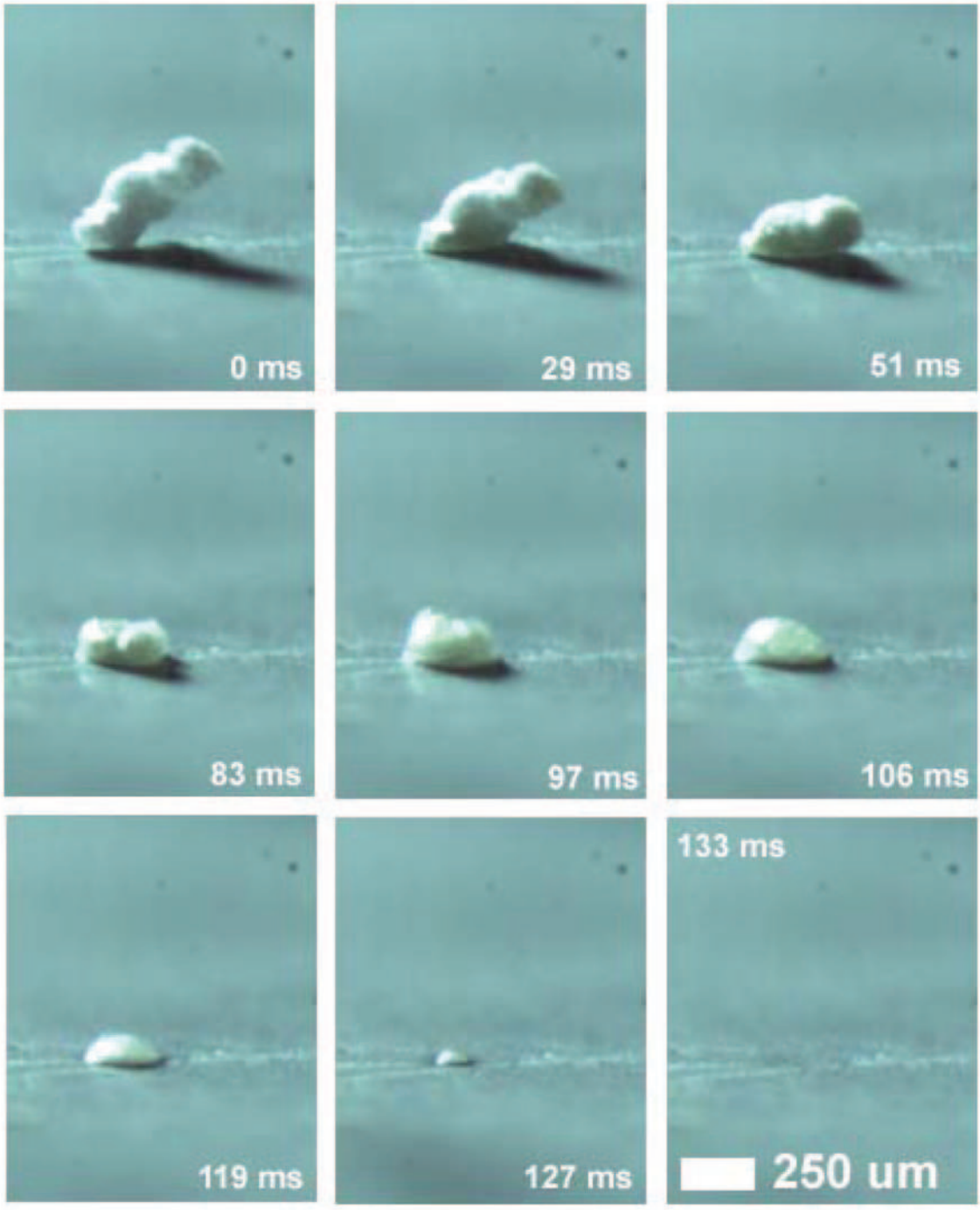

Figure A.10: Cellulose particle conversion was studied on RhCe-coated alumina wafer in air heated from below by a butane torch at 700 °C.

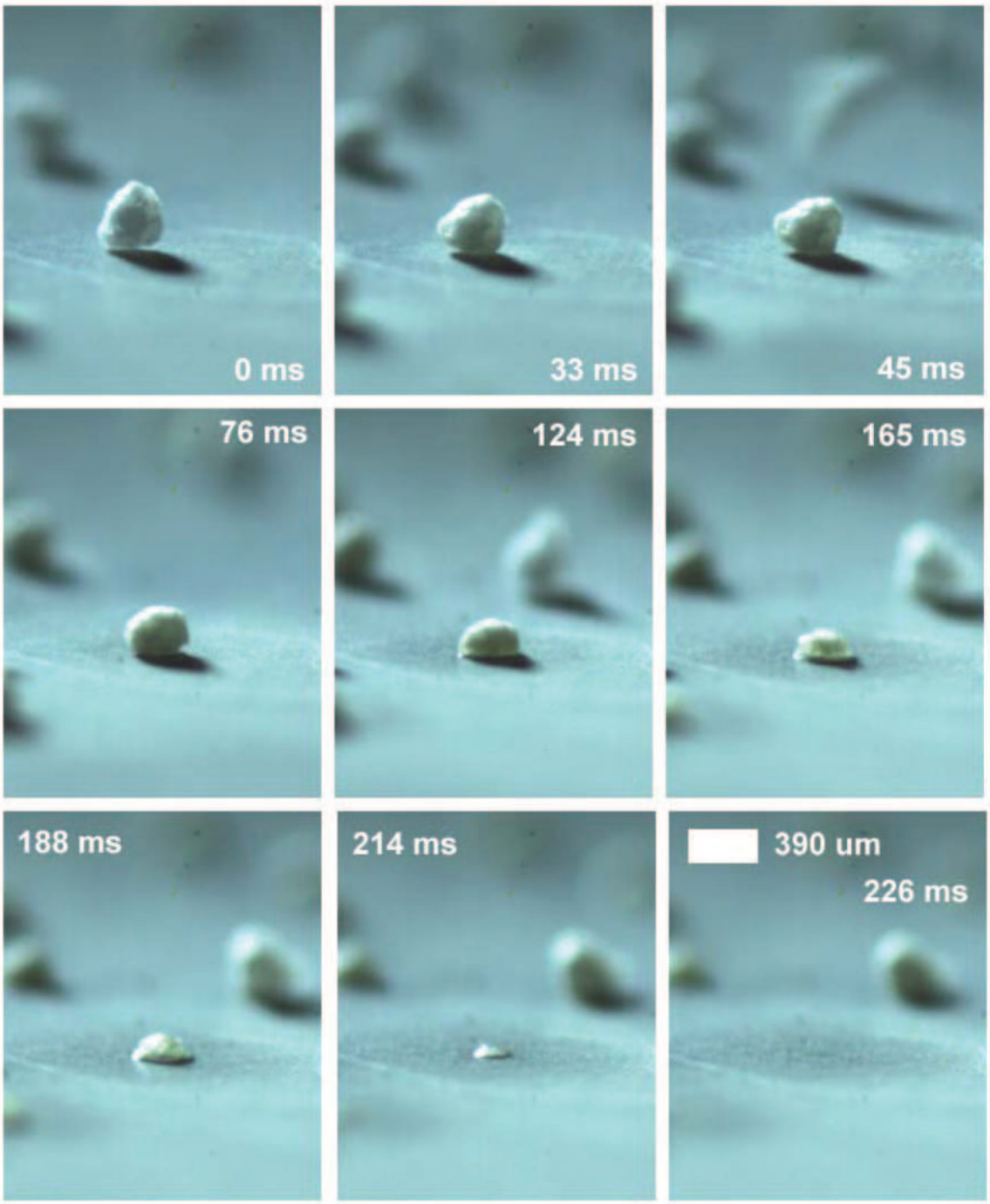

Figure A.11: Cellulose particle conversion was studied on RhCe-coated alumina wafer in air heated from below by a butane torch at 700 °C.

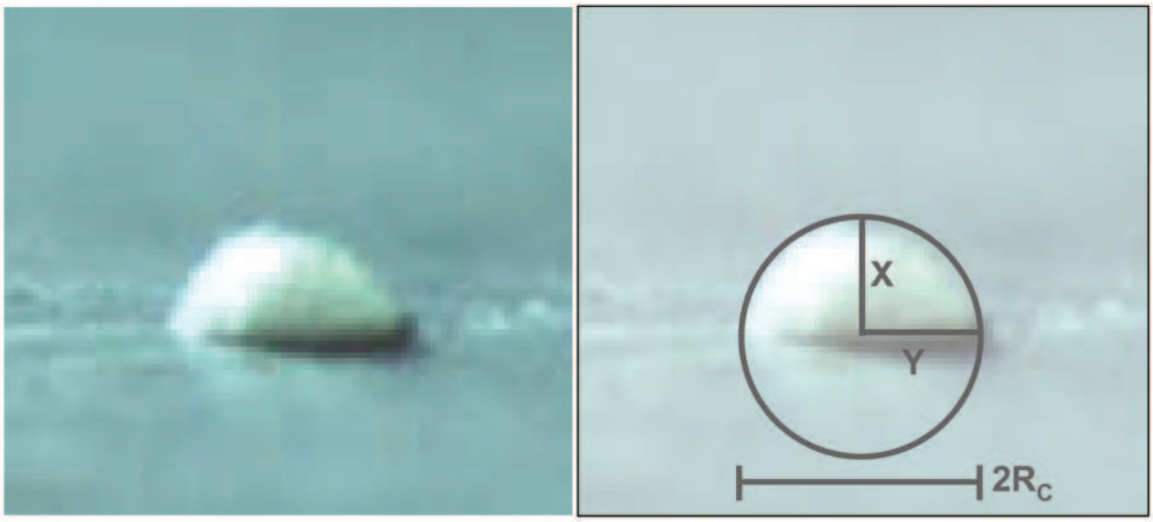

$$R_C = \frac{X^2 + Y^2}{2X}$$

$$V = \pi\left(RX^2 - \frac{1}{3}X^3\right)$$

Figure A.12: Cellulose particles completely converted to liquid were measured for height, x, and width, 2y, as a function of time. The radius of curvature, R_C, and volume, V, of the droplet were then calculated by the listed equations.

was calculated permitting a calculation of the liquid droplet volume, V. As shown in Figure A.13 and A.14, the radius of curvature and droplet volume exhibited constant linear change with time.

Figures A.15 and A.16 depict the conversion of two particles of sucrose (mp = 190 °C) on the flat catalytic surface at 700 °C. The solid crystalline particle appears very different (transparent with flat surfaces) than the microcrystalline (semi-crystalline) cellulose particle at the moment of impact. Both sucrose particles rapidly melt to a nonvolatile liquid droplet which initiates reactive gas and volatile organic evolution. The liquid droplets rapidly decrease in volume leaving a clean, flat surface.

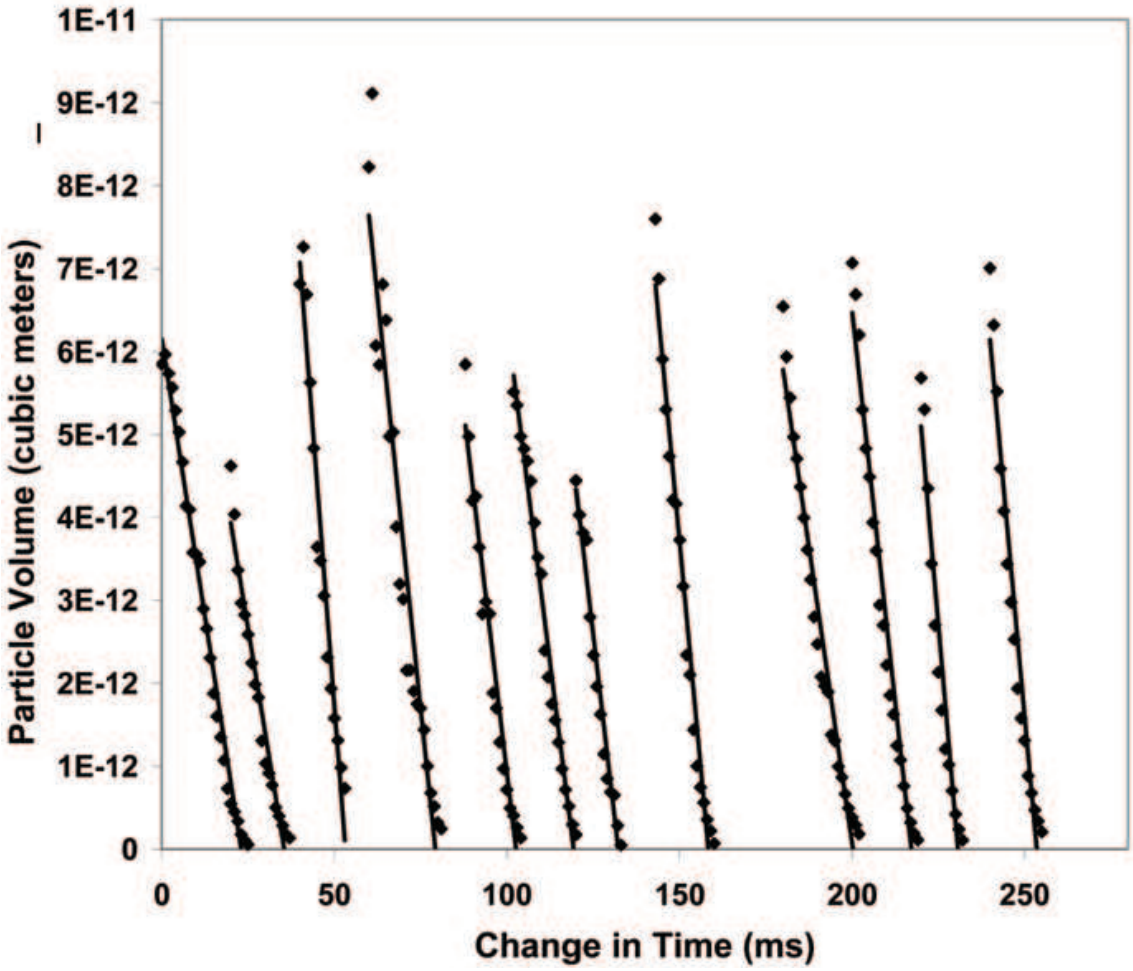

Figure A.13: Cellulose particles completely converted to liquid exhibit approximately linear change in volume as a function of time. Twelve particles are shown decreasing in volume starting from arbitrary time corresponding to Region C of Figure 2.3.

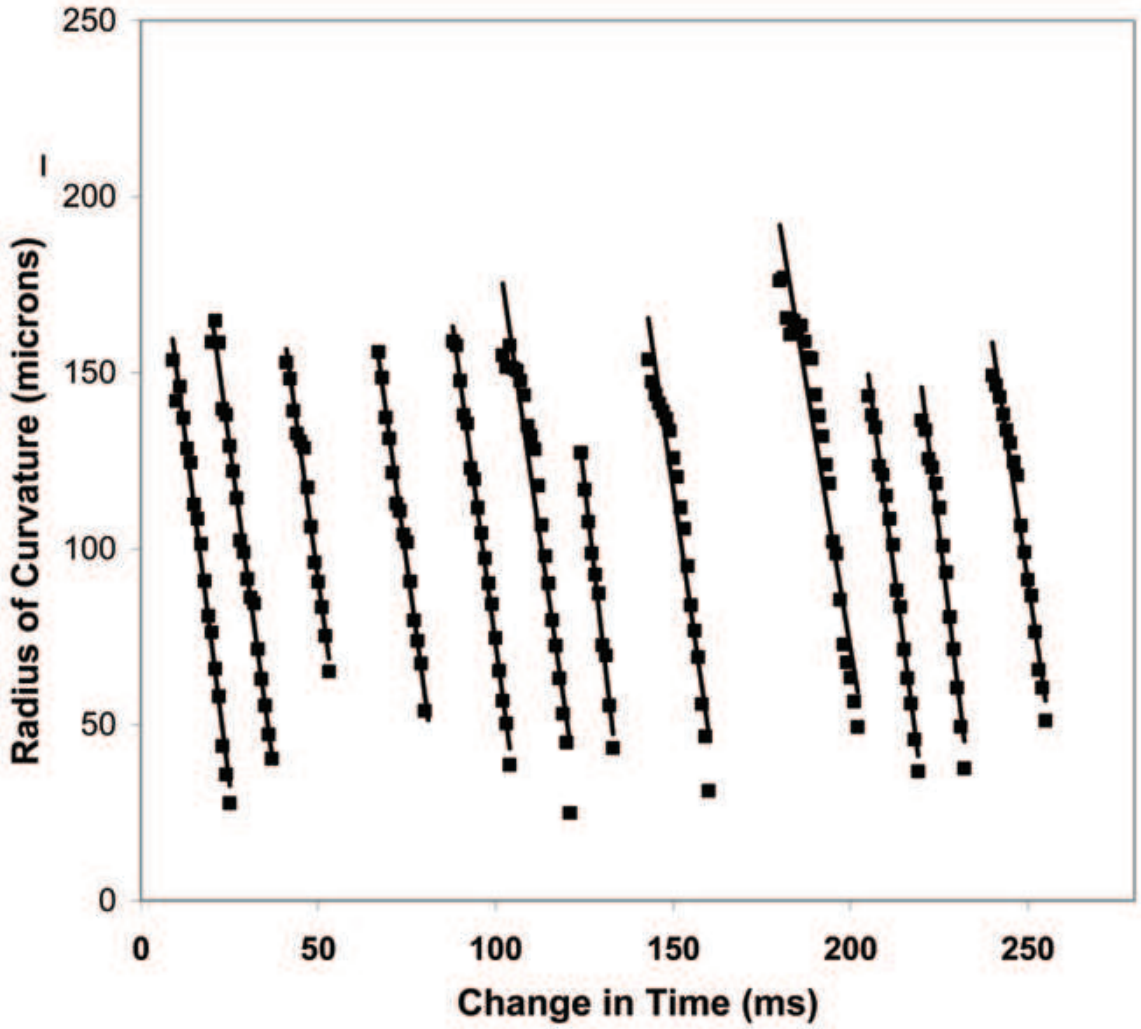

Figure A.14: Cellulose particles completely converted to liquid exhibit approximately linear change in radius of curvature as a function of time. Twelve particles are shown decreasing in radius of curvature starting from arbitrary time corresponding to Region C of Figure 2.3.

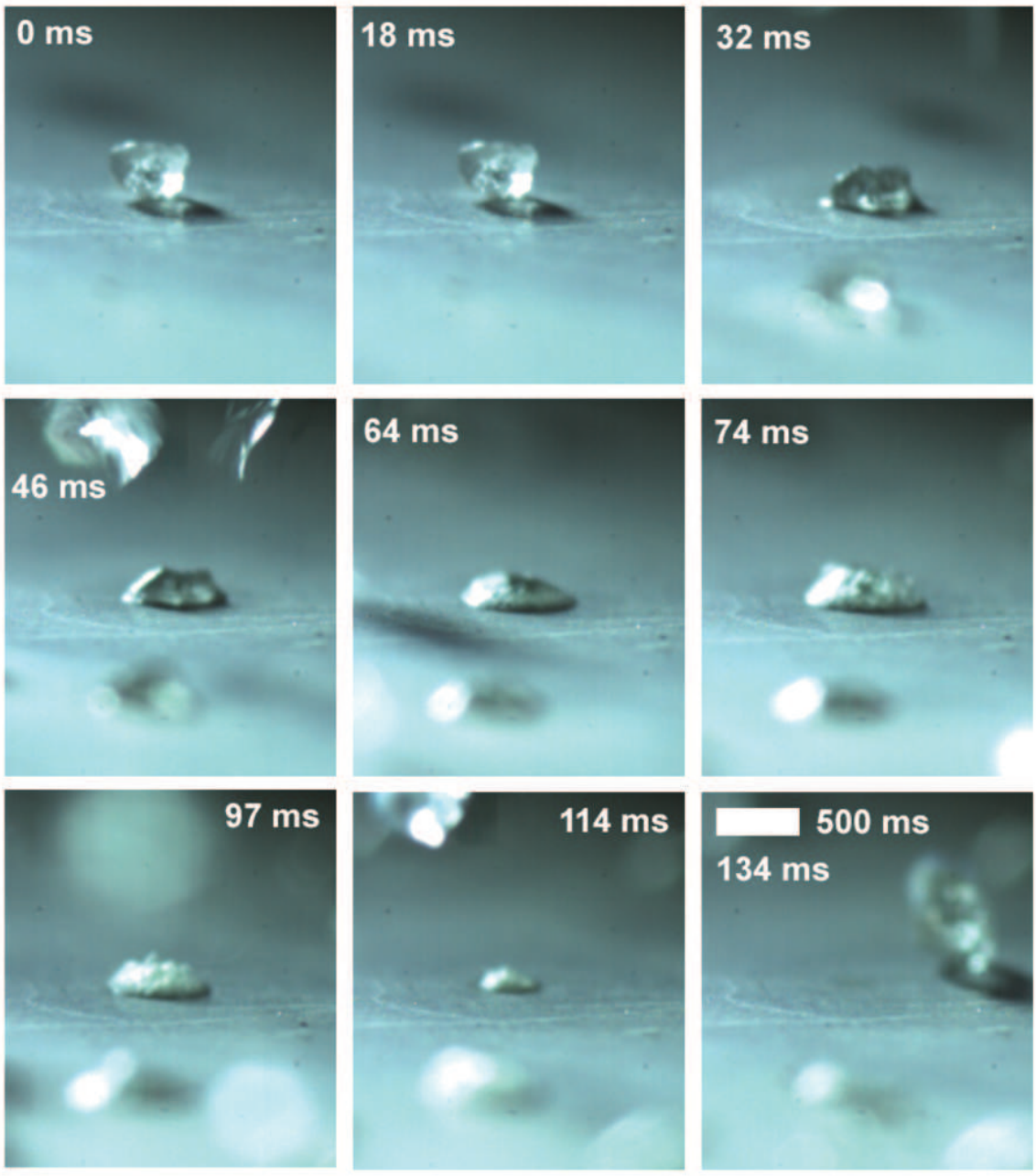

Figure A.15: Crystalline sucrose particle conversion was studied on RhCe-coated alumina wafer in air heated from below by a butane torch at 700 °C.

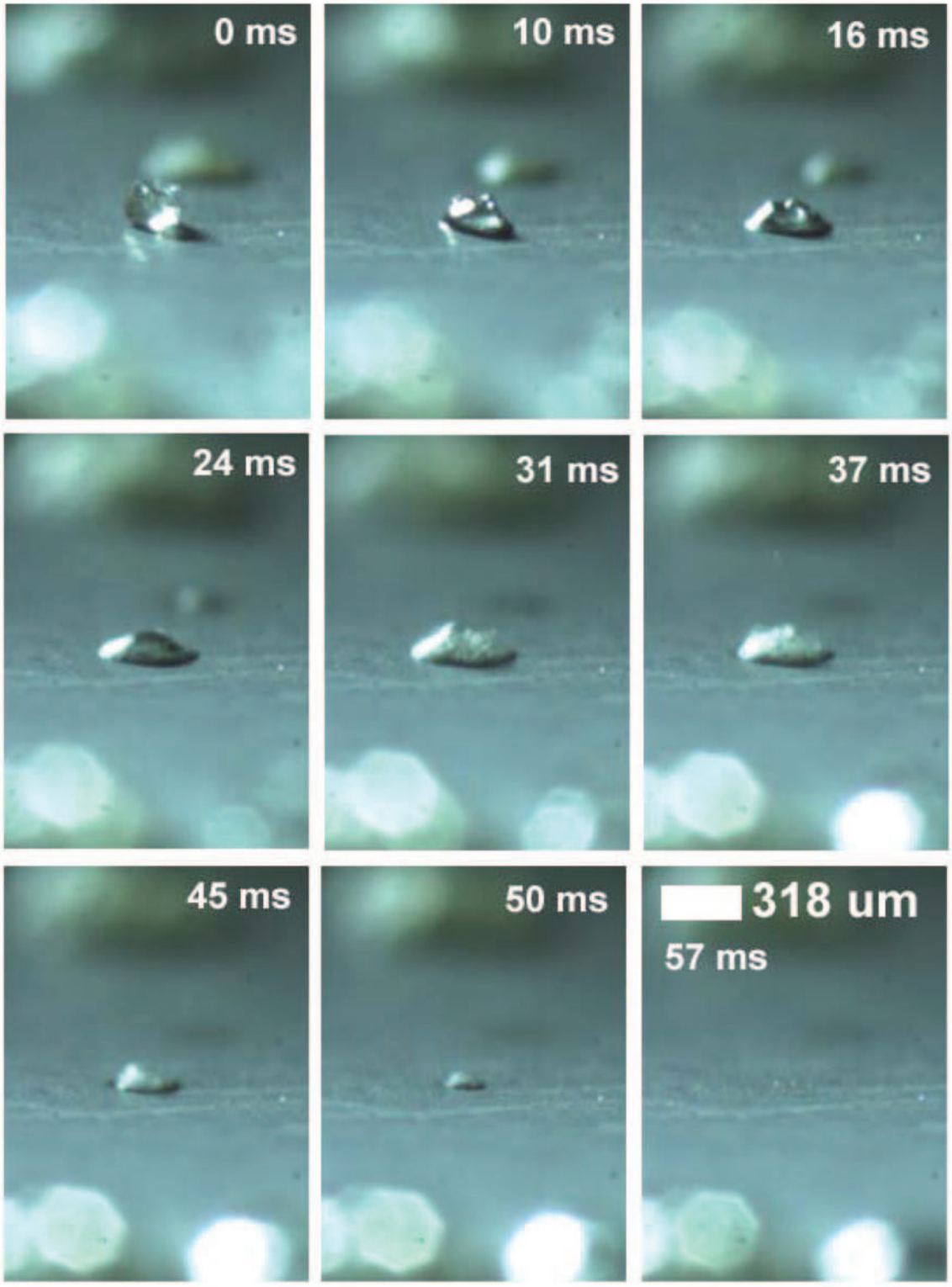

Figure A.16: Crystalline sucrose particle conversion was studied on RhCe-coated alumina wafer in air heated from below by a butane torch at 700 °C.

A.5 Glycerol Droplets on Catalytic Foams and Wafers

The paper refers to glycerol droplets converting by reactive flash volatilization to volatile species. Glycerol boils under atmospheric pressure at $\sim$ 290 °C permitting a liquid particle to form a gaseous film between itself and a hot surface. Figure A.17 shows the impact dynamics (impact and breakup) of a large particle ($\sim$ 800 μm) of glycerol on a catalytic foam at 650 °C. Due to its boiling point restriction, the temperature difference between the surface and the particle must be approximately 350 °C. The key observation of the frames (particularly 27 - 47 ms) is the absence of the nucleating gaseous bubbles.

A.6 Method for Cellulose Rod Experimental Setup

Cellulose rods were prepared by pulping (grinding at high speed in the presence of distilled water) prepared sheets of cellulose-rich biopolymer. Analysis of the cellulose-rich sheets showed that some hemicellulose was still mixed with cellulose (79.8 % glucan, 19.5 % xylan, 0.3 % lignin, 0.4 % ash). The liquid pulp was poured into a mold with a mesh bottom (50 cm x 50 cm x 1 cm deep), compressed with a board, and dried for two days. The semi-dry slab was removed from the mold, and air-dried in the presence of a fan for three additional days. The board was then cut using a table saw in the following manner. All four edges were lightly trimmed (1 - 2 mm) creating a square slab. Strips of cellulose were cut with a saw to 7 mm width. The strips were then trimmed with a razor blade to 7 mm cross width, creating a cellulose rod 7 mm x 7 mm x 500 mm.

Processing of the cellulose rods was performed in the setup outlined in Figure A.18. Three catalytic foams and one blank heat shield were wrapped in ceramic paper and held in place inside a quartz reactor by friction fit. A thermocouple was placed 10 mm down from the leading edge of the catalytic bed. The reactor was wrapped in insulation. Attached to the top of the reactor was a size 20 pyrex reactor endcap fused to a 1 cm I.D. pyrex tube extending $\sim$ 1 m from the top of the reactor. Gases (N_2, O_2, and CH_4) flowed into the cap through the outside of the annulus to the catalyst. A quartz light pipe was inserted into the outside of the annulus and down to the leading edge of the catalyst. The long pyrex tube was graduated (Δx =

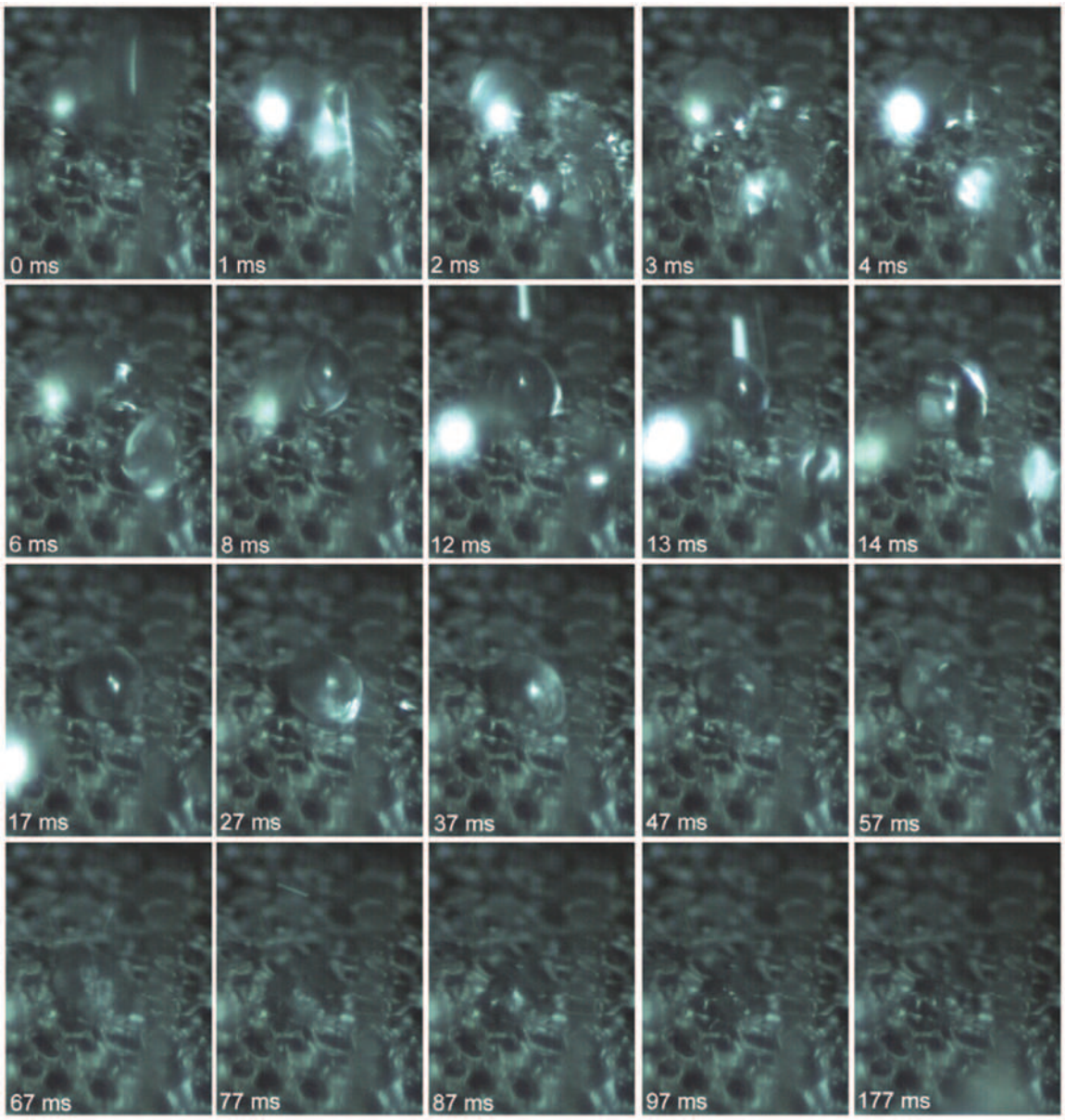

Figure A.17: Impact of a large droplet ($\sim$ 800 μm) of room temperature glycerol on a Rh-Ce (2.5 wt% each) on 80 ppi alpha alumina (99 %) foam at C/O = 1.5 and a surface temperature of 650 °C measured with an optical parameter. Large droplet impact (2 ms) results in two smaller particles with the back particle remaining in the frame until completely disappearing in 177 ms. Original image collected at 1000 frames per second. Frames have been contrast adjusted to enhance viewing. Liquid glycerol droplets do not exhibit development of bubbles but rather appear to move around on the hot surface under a film of gas consistent with the Leidenfrost phenomenon.

1 cm) along its entire length to measure the movement of the rod with time. Metal weights (60, 120, 180 g) were inserted through the top of the tube, and an end cap assured a reactor seal. The catalytic reactor was attached to a secondary fixed bed reactor with 9 cm long by 18 mm diameter of Rh-Ce/α-Al_2O_3 spheres. The secondary bed assured that all organics were broken down to non-condensable carbon species (CO, CO_2, CH_4) for measurement with a gas chromatograph. The secondary reactor bed was wrapped in a resistive heater and then in 1 inch thick ceramic insulation and the bed temperature was maintained at 700 °C. Effluent gases were sampled during initial rod experiments to validate carbon flow rates measured visually.

The reaction was initiated by flowing CH_4, O_2, and N_2 over the catalyst and supplying heat externally from a butane torch. Methane was selected as the control fuel due to its inability to exhibit homogeneous chemistry at the considered temperatures upstream of the catalyst where the virgin cellulose rod rested. The methane catalytic partial oxidation (CPO) reaction lit off at $\sim$ 350 °C generating sufficient heat to initiate an orange glow at the leading edge of the catalyst. The rod was supported on a sealed pull-pin and dropped on the catalyst after light off. Initiation of the methane CPO reaction generates sufficient heat to initiate cellulose decomposition. In general, 5-10 cm of rod was permitted to process before data was collected (reported in Fig. 2.3) to allow steady-state processing conditions. The first catalyst was replaced every three rods.

Figure A.19 shows the surface temperature measured with the optical pyrometer attached to the quartz light pipe on the surface of the reaction catalyst. Without the presence of a cellulose rod, methane CPO exhibited $T_{surface}$ behavior that was satisfactorily fit with a third degree polynomial as a function of the dilution parameter (N_2 mol%). The methane temperature served as a measure of the bulk surface temperature. Naturally, the interaction of the rod with the catalyst foam will alter the temperature immediately at the interface in a complex manner requiring future study.

Figure A.20 shows that rod height as a function of time for three rods with the 60 gram weight as a function of the bulk surface temperature to demonstrate the behavior of continuous, steady state cellulose processing. Each data point represents the recorded time at which the top edge of the cellulose rod passed a length marker on the reactor tube. These experiments generated a large number of measurements for each experimental parameter combination. By examining multiple applied pressures and dilution parameters, Table A.1 (data used in Fig. 2.3) was constructed showing cellulose processing rates. The 95 % confidence interval listed in the Figure 2.3 caption

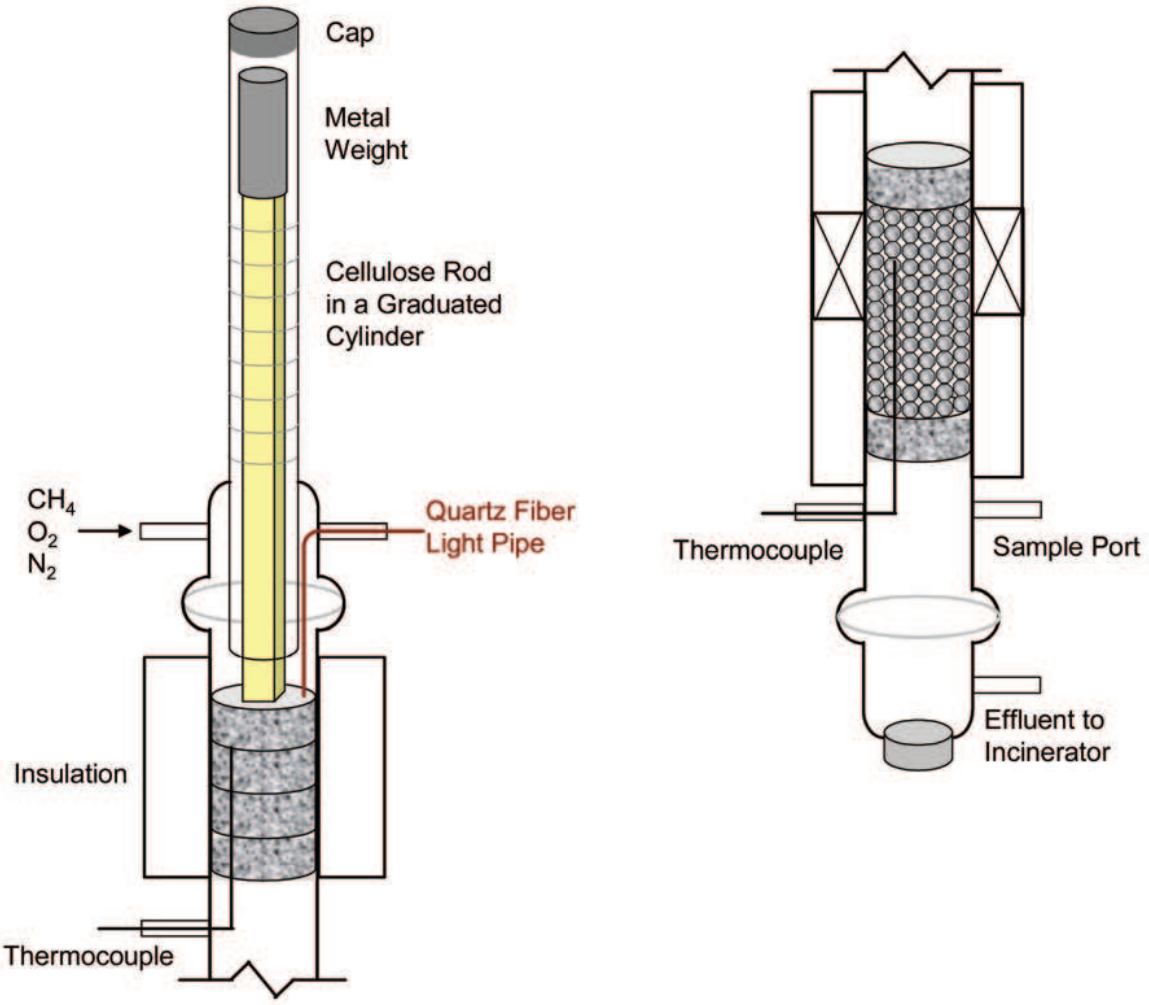

Figure A.18: Conversion of cellulose rods to synthesis gas was examined using a RhCe-coated 80 ppi alumina foam catalyst in a 20 mm I.D. quartz reactor wrapped in ceramic insulation. A size 20 pyrex tube end-cap was fused with a graduated 1 cm O.D. pyrex tube extending $\sim$ 1 m above the reactor and 1 cm past the interface between the end-cap and the reactor. Cellulose rods (7 mm by 7 mm) placed in the pyrex tube were pressed against the foam catalysts by cylindrical steel weights placed on top of the cellulose rod. A thermocouple was placed in the catalytic bed 10 mm from the catalyst/cellulose interface. A quartz light pipe fiber was inserted in the feed end-cap and contacted the catalyst perpendicularly. Effluent gases then passed over a 9 cm Rh-Ce bed of spheres heated by an external resistive heater to 700 °C to ensure complete breakdown to combustion products and synthesis gas. Products were sampled with a syringe, and the effluent was passed to an incinerator.

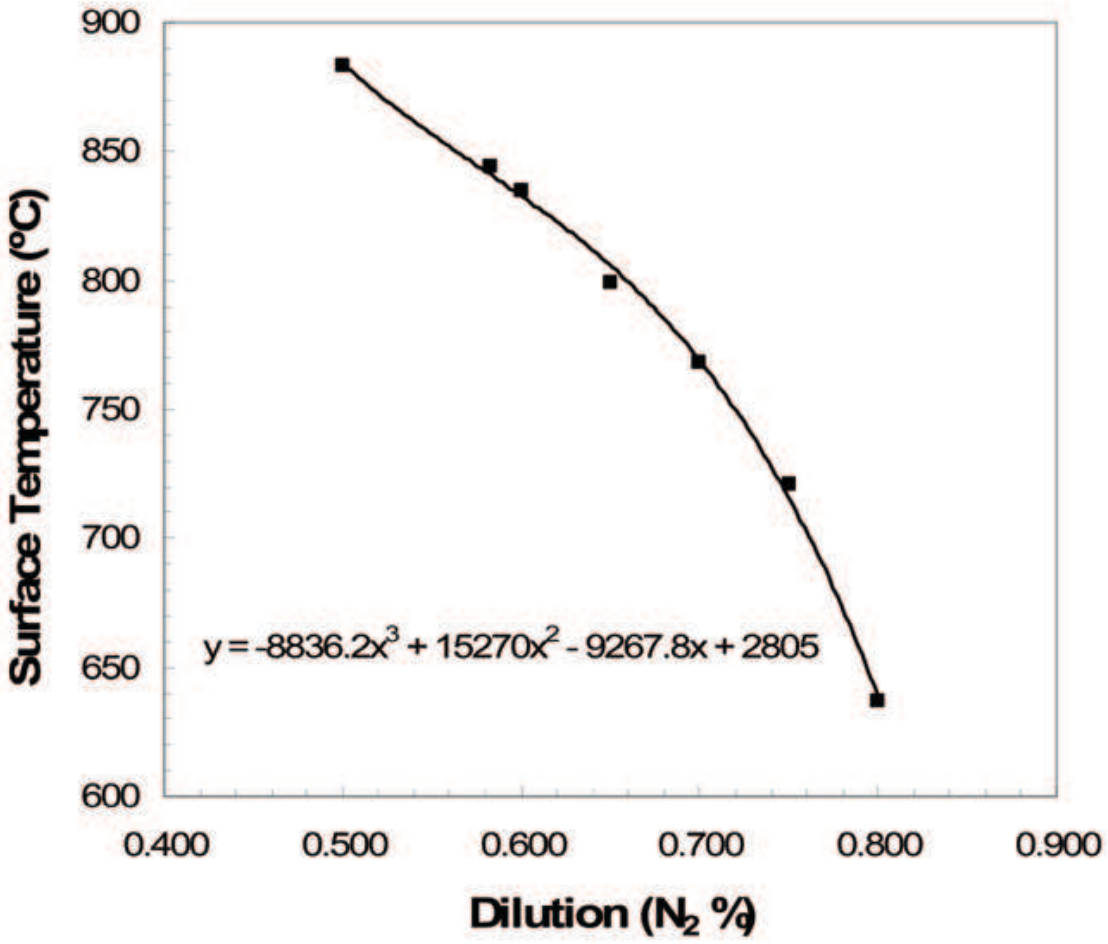

Figure A.19: The bulk surface temperature was measured using an optical pyrometer collecting light through a quartz light pipe touching the surface of an Rh-Ce/α-Al_2O_3 80 ppi foam operating with CH_4, O_2 and N_2. The total gas flow rate was maintained at 5.0 SLPM, and the C/O ratio was maintained at 0.8. The dilution (N_2 / (N_2 + O_2 + CH_4)) was varied between 0.5 and 0.8 to vary the surface temperature on the catalytic foam.

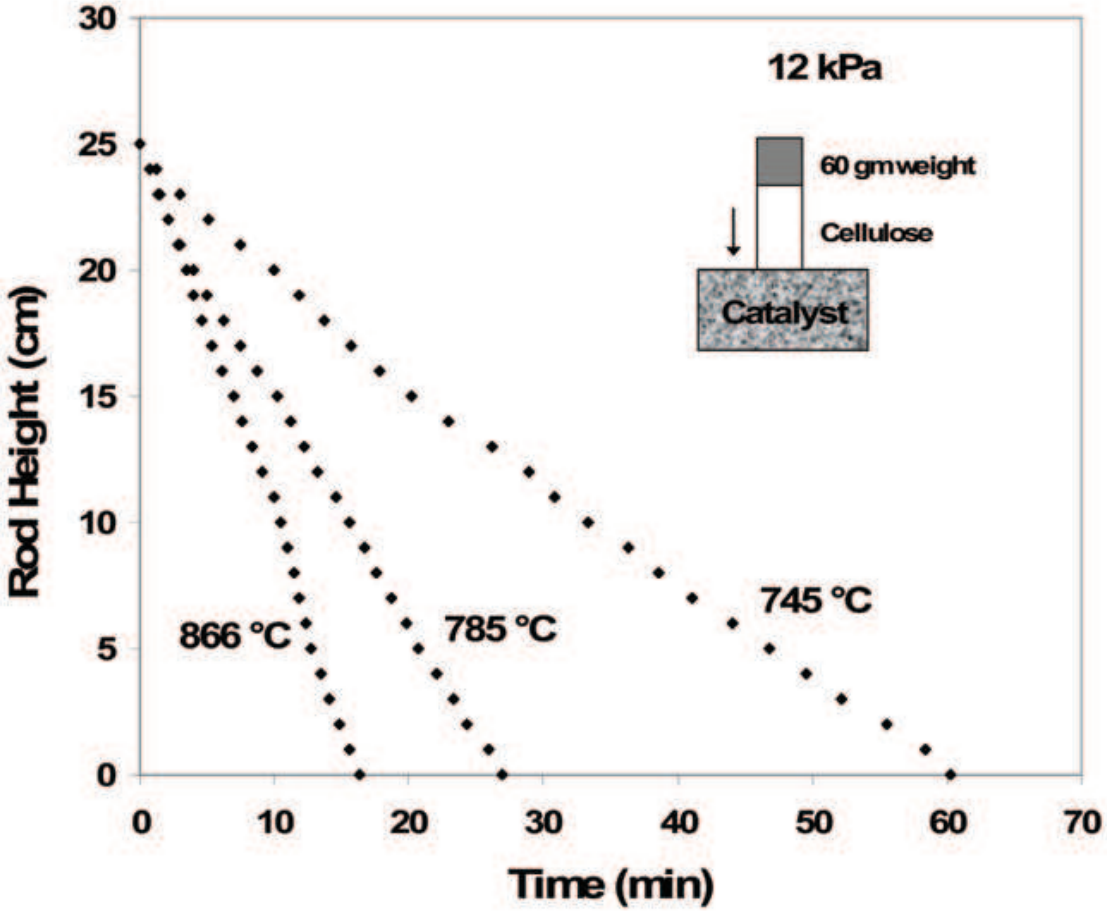

Figure A.20: Rods of cellulose (7 mm x 7 mm x 500 mm) were pressed against an operating Rh-Ce/α-Al_2O_3 80 ppi foam catalyst operating with CH_4, N_2 and O_2. The rate of rod pyrolysis was measured as rod height as a function of time.

was calculated by the method of Table A.2.

Table A.1: The conversion of rods of cellulose (7 mm X 7 mm X 500 mm) on Rh-Ce/α-Al_2O_3 80 ppi foams was examined to determine conversion rate (flux through the catalyst) as a function of the dilution parameter and accompanying bulk surface temperature.

	Char			Transition	Pyrolysis				
Experiment #	**6**	**3**	**5**	**7a**	**18**	**1**	**0**	**4**	**2**
Weight (grams)	60	60	60	60	60	60	60	60	60
Flux (kg hr^{-1} m^{-2})	28	37	39	80	91	98	111	135	154
ΔR (95%)	4	6	6	12	10	9	22	19	12
D, Dilution Parameter	0.77	0.75	0.725	0.713	0.697	0.68	0.65	0.59	0.53
$T_{Surface}$(°C)	688	716	745	757	772	785	806	838	867
Experiment #	**16**	**17**	**15**	**14b**	**14a**	**12**	**10**	**9**	**11**
Weight (grams)	120	120	120	120	120	120	120	120	120
Flux (kg hr^{-1} m^{-2})	39	50	54	79	108	123	161	199	250
ΔR (95%)	5	4	1	15	11	26	21	24	36
D, Dilution Parameter	0.77	0.75	0.725	0.713	0.697	0.68	0.65	0.59	0.53
$T_{Surface}$(°C)	688	716	745	757	772	785	806	838	867
Experiment #	**24**	**23**	**25**	**21**	**20**	**19**	**22**		
Weight (grams)	180	180	180	180	180	180	180		
Flux (kg hr^{-1} m^{-2})	48	70	69	102	136	199	327		
ΔR (95%)	9	15	11	19	24	40	106		
D, Dilution Parameter	0.77	0.75	0.725	0.713	0.697	0.68	0.65		
$T_{Surface}$(°C)	688	716	745	757	772	785	806		
Experiment #					**27**	**26**			
Weight (grams)					150	90			
Flux (kg hr^{-1} m^{-2})					208.61	118.55			
ΔR (95%)					30.31	13.27			
D, Dilution Parameter					0.65	0.65			
$T_{Surface}$(°C)					806	806			

Table A.2: The experimental data in Figure 2.3 exhibited a 95 % confidence interval equivalent to $\sim$ 21 kg $hr^{-1}m^{-2}$. Variance from all experiments was pooled and the degrees of freedom was calculated as 553.

Experiment #	St Dev	# of Measurements	Variance
18	1.464	36	2.14
1	1.29	35	1.66
0	1	13	1.14
4	2.57	30	6.60
2	1.66	32	2.76
14a	1.11	16	1.24
12	3.78	33	14.26
10	3.03	32	9.17
9	2.76	22	7.61
11	4.02	26	16.19
20	3.19	29	10.17
19	5.72	32	32.67
22	4.97	11	24.71
7a	0.6	13	0.36
14b	1.451	15	2.11
21	1.575	11	2.48
5	0.79	28	0.62
3	0.72	25	0.52
6	1.12	25	1.25
15	2.037	25	4.15
17	1.995	25	3.98
16	1.542	32	2.38
25	0.703	6	0.49
23	1.602	18	2.57
24	0.656	9	0.43
		Pooled Variance	151.7
		PV^0.5	12.32
		N - 25 - 1	553
		Interval (± g/hr)	1.03
		Conversion to Flux	20.94